University of Zurich UZH

Measurement of Open Charm and Double Open Charm Production Cross Sections and Ratios in pp Collisions at $\sqrt{s} = 2.76$ TeV with the LHCb Experiment

Master Thesis

zur

Erlangung des akademischen Grades Master of Science (MSc)

Vorgelegt der

Mathematisch-Naturwissenschaftlichen Fakultät

der

Universität Zürich

Von

Enzio Crivelli

aus

Solothurn, Schweiz

Aufsicht:

Prof. Dr. Ulrich Straumann (Vorsitz)

Dr. Katharina Müller

Dr. Albert Bursche

Zürich

15. Juni 2016

Abstract

In proton-proton collisions, mechanisms other than gluon-gluon fusion can contribute to double charm production. One possible additional source is double parton scattering (DPS). The theory of Quantum Chromodynamics cannot precisely predict DPS production cross sections, since simplifications have to be used. Double open charm production cross sections in proton-proton collisions at LHCb have been measured so far at a centre of mass energy of $\sqrt{s} = 7$ TeV (see [2], [3]). These provide valuable input for the theoretical understanding of DPS. In this work such double open charm production cross sections are measured at LHCb at $\sqrt{s} = 2.76$ TeV using D^0 and D^+ mesons in the final state.

Acknowledgement

Contents

1 Introduction

The purpose of physics is to explain the fundamental laws of nature. At present, four fundamental forces determine all known physical processes: the gravitational force, the electromagnetic force and the weak- and strong forces. In particle physics experiments like LHCb, all fundamental forces except gravitation are examined by colliding particles with high energy and by analyzing the collision products. Subsequently the results can be compared with theoretical predictions.

This work discusses the measurement of the single and double open charm production cross sections in proton-proton (pp) collisions at LHCb at a center of mass energy of $\sqrt{s} = 2.76$ TeV. The production channels are $pp \rightarrow c\bar{c} + X$ resp. $pp \rightarrow \bar{c}c\bar{c}c + X$, where X denotes an arbitrary number of additional final state particles. For comparision the open charm pair production channel is also considered. The chosen decay modes are $D^0 \rightarrow K^- \pi^+$ and $D^+ \rightarrow K^- \pi^+ \pi^+$. In pp collisions, other processes than single parton scattering (SPS) can contribute to double open charm production [1]. One possible additional source is double parton scattering (DPS). Since QCD models for DPS rely on simplifications in order to be able to calculate correponding cross sections, the predictions are relatively inaccurate, when compared with calculations for single parton scattering (SPS) for instance. Experimental measurements of double charm production cross sections allow to improve the understanding of the DPS contributions in the production processes and can help to calibrate theoretical predictions. This analysis complements LHCb measurements of $J\psi$, open charm and double open charm production cross section at LHCb at $\sqrt{s} = 7$ TeV [2], [3], however with a much smaller integrated luminosity of $\mathscr{L} = 3.3$ pb^{-1}.

The thesis is structured in five chapters. Chapter 2 gives a brief overview of the main foundations of the theory of modern particle physics, followed by a description of the LHC collider and LHCb detector in chapter 3. The analysis is presented in chapter 4, starting with an overview of the strategy. The determined cross sections are shown in chapter 5, while the thesis is completed by a discussion of the results given in chapter 6.

2 Theory

The standard model of particle physics (SM) is able to explain most the observed phenomena in particle physics. It describes the elementary particles and their fundamental interactions by three of four fundamental forces of nature, being the electromagnetic force and the weak- and strong forces, but not gravitation. Known shortcomings lie in the lack of explanation for dark matter and dark energy as well as the abundance of matter over antimatter.

This chapter follows standard textbooks [4], [5], [6]. Due to the extension and complexity of the SM it is only intended to give a brief overview of the main foundations of the modern understanding of fundamental particle physics. This includes the fundamental and composite particles with their interactions encountered at particle colliders like the LHC in chapter 2.1 and the DPS model explained in chapter 2.2.

2.1 The Standard Model of Particle Physics (SM)

The SM consists of fundamental particles, i.e particles that are assumed to be point-like and have consequently no inner structure, classified according to their interaction ability (see Tab. 2.1 and Tab. 2.2).

Fundamental Particles
These are the electrically neutral gauge bosons γ, Z, g, H, the charged gauge bosons $W^\pm$, the charged leptons $e^\pm$, $\mu^\pm$, $\tau^\pm$, the electrically neutral leptons ν_e, ν_μ, ν_τ, called neutrinos, and the quarks u, d, c, s, t, b. They can be split by the quantum number (QN) of spin s into two groups, the bosons (s 1) (including the higgs (s 0)) and fermions (s 1/2).

- **Fermions**
  Each fermion f has an antiparticle state with the same qualities with the exception of an opposite charge QN q_e, denoted by a bar (e.g. $\bar{u}$). The fermions can be split further by the QN of isospin I into doublets leading to three families. There are two groups of fermions, called leptons l and quarks q.

  The leptons l consist of the charged electron, muon and tau with $q_e = -1$, of which only the electron is stable, and the corresponding electrically neutral neutrinos. These neutrinos usually escape detection in most particle collider experiments, since they exclusively interact by the weak force resulting in very small cross sections.

  The quarks q exist in six flavours, up (u), down (d), charm (c), strange (s), top (t) and bottom (b) and have a non-integer charge of $q_e = +2/3$ resp. $q_e = -1/3$.

They form all composite particles, of which only the ones formed by quarks from the first family (up, down) can be stable. Quarks have an additional charge, called color charge $q_c \in \{r, g, b, \bar{r}, \bar{g}, \bar{b}\}$ (red, green and blue with their anticolors), which exclusively allows them to interact by the strong force. They can not be directly observed in experiments, but only as constituent of composite particles, since they do not exist as free particles due to the QCD phenomenon called confinement, which allows only states with zero net color charge to exist freely.

- **Bosons**
  The gauge bosons are the carriers of the fundamental forces. The photon γ is the gauge boson of the electromagnetic force, describing the interaction between charged fermions. It is stable, charge- and massless and moves at the speed of light
  $c = 2.998 \cdot 10^8$ m/s.

  The massive $W^\pm$ and Z bosons mediate the weak force, which couples to quarks and leptons and allows changes of flavour, e.g. $l^- \to W^- \nu_l$, $d \to W^- u$. The weak force also allows transitions between different quark families, e.g. $c \to W^+ d$. The amplitude of a transition $i \to W^\pm j$ is proportional to the corresponding element of the Cabibbo-Kobayashi-Maskawa (CKM) matrix $|V_{ij}|^2$, given by:

  $$|V_{\text{CKM};ij}| = \begin{pmatrix} |V_{ud}| & |V_{us}| & |V_{ub}| \\ |V_{cd}| & |V_{cs}| & |V_{cb}| \\ |V_{td}| & |V_{ts}| & |V_{tb}| \end{pmatrix} = \begin{pmatrix} 0.974 & 0.225 & 0.004 \\ 0.225 & 0.986 & 0.041 \\ 0.008 & 0.040 & 0.999 \end{pmatrix} \quad . \tag{2.1}$$

  Due to the dominance of the diagonal matrix elements, transitions across families are suppressed, called Cabibbo suppression. This suppression is the strongest when the quarks of the third family are involved. The eight charge- and massless gluons g are the gauge bosons of the strong force. They interact with the quarks q and are responsible for holding the composite fermions (e.g. proton and neutron) together. They also carry color charge themselves, enabling the interaction among each other.

  The massive higgs boson H is needed in the SM to break the electroweak symmetry and to give each fundamental particle its mass.

Quantity	1st family	2nd family	3rd family
	Quarks		
	up (u)	charm (c)	top (t)
q	$+2/3$	$+2/3$	$+2/3$
M_0 [MeV/c^2]	$\approx 2 - 3.5$	$\approx 1.27 \cdot 10^3$	$\approx 172 \cdot 10^3$
s	$1/2$	$1/2$	$1/2$
	down (d)	strange (s)	bottom (b)
q	$-1/3$	$-1/3$	$-1/3$
M_0 [MeV/c^2]	$\approx 4 - 5.5$	≈ 101	$\approx 4.67 \cdot 10^3$
s	$1/2$	$1/2$	$1/2$
	Leptons		
	electron (e^-)	muon (μ^-)	tau (τ^-)
q	-1	-1	-1
M_0 [MeV/c^2]	$= 0.511$	$= 105$	$= 1780$
s	$1/2$	$1/2$	$1/2$
	electron neutrino (ν_e)	muon neutrino (ν_μ)	tau neutrino (ν_τ)
q	0	0	0
M_0	< 2 eV/c^2 95% CL	< 17 keV/c^2 95% CL	< 1.23 MeV/c^2 95% CL
s	$1/2$	$1/2$	$1/2$

Table 2.1: Overview of the fermions in the Standard Model (SM) [7]. For each fermion f an anti-particle state exists, denoted by $\bar{f}$. Since such anti-particle states have the same qualities as the corresponding fermions, with the exception of the opposite charge-like QN, they are not listed in the table.

Quantity		Gauge Bosons		
	photon (γ)	$W^{\pm}$, Z bosons	gluon (g; 8 color charges)	Higgs (H)
q	0	± 1 ($W^{\pm}$), 0 (Z)	0	0
M_0 [GeV/c^2]	0	= 80.4 ($W^{\pm}$), 91.2 (Z)	0	$\approx$ 126
s	1	1	1	1
Interaction Type	electromagnetic	weak	strong	higgs mechanism

Table 2.2: Overview of the bosons with their accompanying interaction in the SM [7].

The quarks form composite particles, called hadrons, whose properties are largely determined by their valence quarks. The gluons holding such a hadron together constantly produce and annihilate quark-antiquark pairs $q\bar{q}$ (sea quarks) due to their self interaction by the strong force.

Composite Particles

According to the number of valence quarks, hadrons can be structured into two groups: the baryons containing three quarks and the mesons consisting of a quark-antiquark pair.

- **Baryons**
  The most common hadrons are the proton p and neutron n, whose valence quark content is $p = uud$ and $n = udd$. They are the components of the atomic nuclei listed in the periodic system of elements. All baryons, with the possible exception of the proton, are unstable. For example, when not bound in a nuclei, a free neutron decays into a proton, electron and electron neutrino with a lifetime of about 900 s. This radioactive β-decay was the first experimentally observed process involving the weak force. Whether the proton can be considered as stable or not is the subject of current experimental research. Since no proton decay is so far observed, lower limits of the lifetime with 90% confidence limit of about 10^{40} s have been determined [7]. Due to such extremely long lifetime expectations, the proton is considered as stable in this work.

- **Mesons**
  No meson is observed to be stable. The most common ones, the kaons (K) and pions (π), decay with a lifetime of about 10^{-8} s [7]. Such long lifetimes allow for their measurement as the traverse through the LHCb detector. They are of particular interest in this work, since the investigated D^0 and D^+ mesons decay into K and π.

The lightest mesons involving one charm quark, $D^0 = c\,\bar{u}$, $D^+ = c\,\bar{d}$ and $D_s^+ = c\,\bar{s}$ with their antiparticles $\bar{D}^0 = \bar{c}\,u$, $D^- = \bar{c}\,d$ and $D_s^- = \bar{c}\,s$ are called D mesons or open charm mesons, due to the not specified quark accompanying the charm. In hadron collider experiments like the LHC experiment, they are produced by the interaction of quarks, which is described by the theory of Quantum Chromodynamics (QCD).

QCD production processes of D mesons

In this non-abelian gauge theory the eight gluons can interact among themselves, leading to complicated processes. The force behaves differently depending on the energy scale with the two extremes of confinement and asymptotic freedom. Since the QCD describes the strong force, a perturbative expansion ansatz is not always feasible. Although numerical and analytical methods to approximate QCD such as lattice QCD exist, perturbative QCD can only be carried out for high energies. The theory offers some interesting characteristics.

- **Confinement**
  When the interaction length of the strong force is increased, i.e. when quarks and/or gluons drift apart, the gluon field strength increases to the point, where a quark-antiquark pair is created. This results in the non-existence of free quarks and gluons, such that only charge-colorless particle states are observed.

- **Asymptotic Freedom**
  When hadrons collide at high center-of-mass energy, their interaction can be described in good approximation as interaction of their single fundamental particle constituents, being the valence (or sea) quarks and gluons, denoted as partons. Such interactions are called hard parton interactions.

- **Factorization**
  The factorization theorem allows the separation of short- and long distance effects. In calculations this means that hard parton interactions calculations and parton distribution functions can be factorized, i.e. written as a products. The cross section for a given final state f can be written as [7]:

$$\sigma_f \; = \; \sum_{ab} \int_{x_a} \int_{x_b} d\xi_a \; d\xi_b \; f_a(\xi_a, \mu_F^2) \; \hat{\sigma}_{ab}(\xi_a, \xi_b, \mu_F^2, \mu_R^2) \; f_b(\xi_b, \mu_F^2) \quad , \qquad (2.2)$$

  where the sum runs over all possible partons a and b (i.e. quarks or gluons) and the integral over their momentum fractions ξ_a and ξ_b, $\hat{\sigma}_{ab}$ is the parton-parton cross section for the final state f and $f_i(\xi_i, \mu_F^2)$, $i \in \{a, b\}$ are the parton distribution functions. These functions defining the probabilities of a parton i having a momentum fraction ξ_i of the hadron momentum p at a factorization scale μ_F have to be determined by experiment, but are important for the calculations in theory.

- **Hadronization**
  Due to the confinement, a free quark cannot be observed. Instead all quarks produced in hard parton interactions form baryons and mesons as the interaction distance of the strong force increases, i.e. they hadronize. Hadronization is flavour conserving, so for each produced c-quark a charm hadron is produced in the final state, e.g. D^0, D^+, D_s^+, D^{*0}, D^{*+}, Λ_c^+, etc.

- **Running Coupling**
  The coupling constant α_s needs to be renormalized, in order to compensate divergences in perturbative QCD. α_s decreases with increasing normalization scale μ_R, leading to both asymptotic freedom for hard parton interactions and confinement.

If the D mesons are produced at high transverse momentum, the QCD factorization can be used [8]. In Fig. 2.1, three typical production diagrams are shown, that contribute to $pp \to c\bar{c}$ production. Because there is only one parton per proton involved, this is referred to as single parton scattering (SPS). Likewise, Fig. 2.2 and Fig. 2.3 show typical production diagrams for $pp \to c\bar{c}c\bar{c}$. When the $c\bar{c}$ pair is produced twice, two cases need to be distinguished. First, $c\bar{c}c\bar{c}$ can be produced by double parton scattering (DPS) involving two partons per proton (see Fig. 2.2). Secondly $c\bar{c}c\bar{c}$ can be produced by SPS (see Fig. 2.3). Since each produced c or $\bar{c}$ quark can hadronize into a D meson, e.g. D^0 or D^+, many such diagrams can contribute to the D meson production. However, some information about the underlying production processes can be extracted from the D mesons. For instance the observation of the double D meson $D^0 D^0$ indicates, that it has not been produced by $pp \to c\bar{c}$ SPS, but by DPS or $pp \to c\bar{c}c\bar{c}$ SPS processes. For DPS, the matrix element occurs twice in the diagrams, where for $pp \to c\bar{c}c\bar{c}$ SPS $gg \to c\bar{c}$ occurs twice in the same pp interaction. Since the contribution of the latter process is much smaller than the observed cross section, the observation of $D^0 D^0$ is a strong indication for DPS [2]. Considering all D meson candidates, this is referred to as double open charm production. For $D^0 \bar{D}^0$ $pp \to c\bar{c}$ SPS, $pp \to c\bar{c}c\bar{c}$ DPS and SPS are possible. Since the DPS processes can not be isolated, this is referred to as open charm pair production. The previous double open charm data obtained by the LHCb experiment [2] have been described using the DPS approach [1] (see chapter 2.2). However, additional experimental input is important to further understand this aspect of QCD.
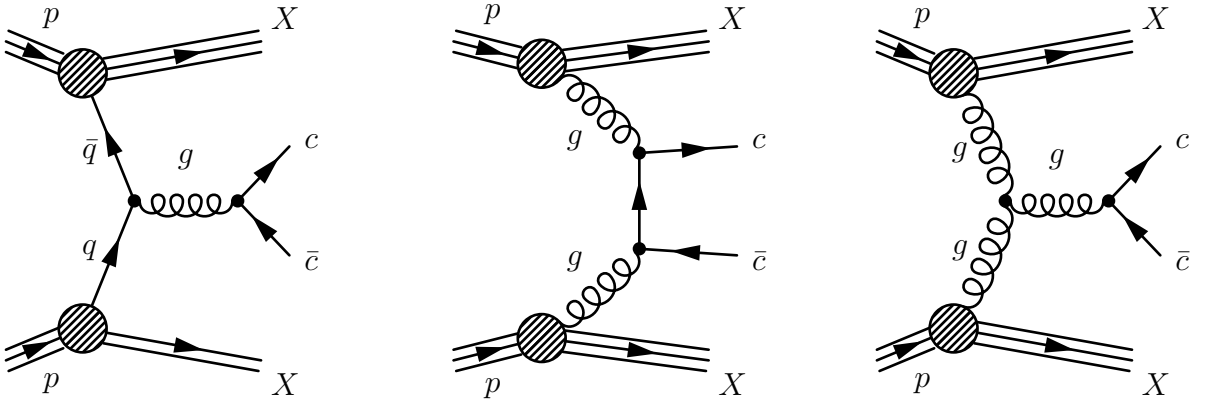
Figure 2.1: Illustration of some SPS production processes for $pp \to c\bar{c}$, called $q\bar{q}$ annihilation (left) and gg fusion (center and right).
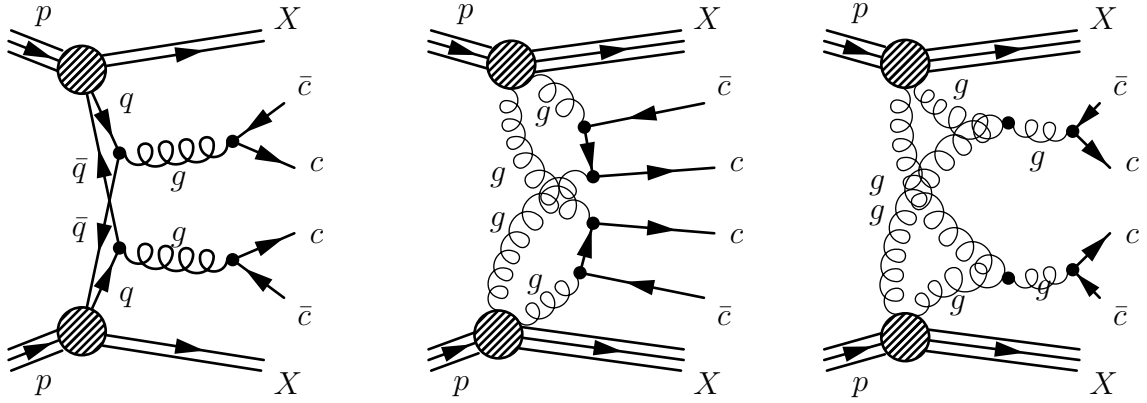
Figure 2.2: Illustration of some DPS production processes for $pp \to c\bar{c}c\bar{c}$, called $q\bar{q}$ annihilation (left) and gg fusion (center and right).
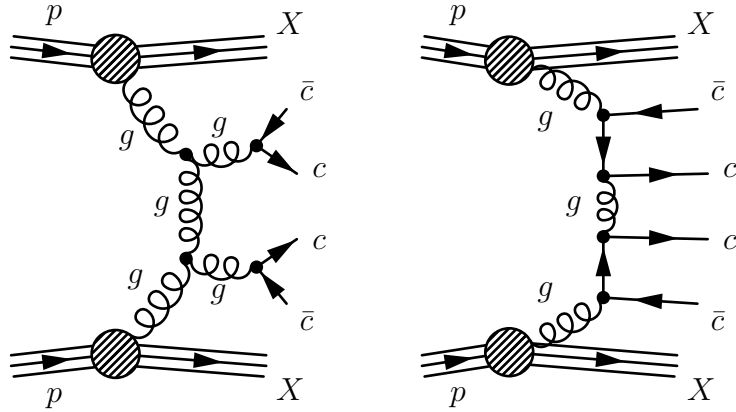
Figure 2.3: Illustration of some SPS production processes for $pp \to c\bar{c}c\bar{c}$.

Since the charm quark needs to change its flavour for a decay of the ground state D mesons, the D^0 and $D^{\pm}$ mesons can only decay by the weak force and have therefore a relatively long lifetime of about 10^{-12} s [7]. At the speed of light this corresponds to a decay length of about 300 μm. In experiments, the property of a relatively long decay length (or lifetime) can be exploited as an advantage by identifying these mesons by their displaced decay vertices. This property is also used in the analysis at hands.

Weak decay processes of D mesons

The charm quarks changes its flavour preferably into the strange quark via an exchange of a $W^{\pm}$ boson, such that D mesons decay mainly into kaons and pions. The two candidates D^0 and D^+ with the corresponding decay modes $D^0 \to K^- \pi^+$ and $D^+ \to K^- \pi^+ \pi^+$ are chosen for this work (see also chapter 4.1). These decay modes are illustrated in Fig. 2.4. The decay modes for the corresponding double open charm candidates $D^0 D^0$, $D^0 D^+$ and $D^+ D^+$ are the same as for the correponding single open charm candidates D^0 and D^+.

Also excited D meson states, such as D^{*0} and D^{*+}, which subsequently decay into D mesons, can be produced in pp collisions. Due to the extremely short lifetimes of these

excitation states of about 10^{-21} s [7], the two sources are not distinguished in this work and all D mesons from these two sources are considered to be promptly produced.

Likewise, B mesons can be produced, which subsequently decay into D mesons. Compared to the D mesons, the B mesons decay also by the weak force, but their decay is additionally Cabibbo suppressed, leading to similar albeit higher lifetimes of about 10^{-12} s [7]. The D meson production from the decay of B mesons is not prompt and is treated as background process (see chapter 4.2.2).
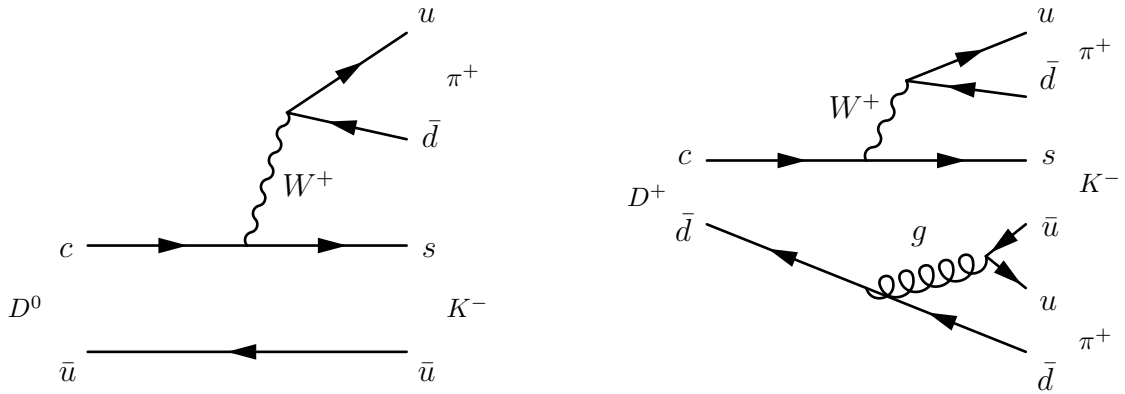
Figure 2.4: Illustration of the D meson decay modes $D^0 \rightarrow K^- \pi^+$ (left) and $D^+ \rightarrow K^- \pi^+ \pi^+$ (right).

The lifetimes of the produced kaons and pions are sufficienctly large for them to travel through the LHCb detector and to be directly measured by their interaction with the detector matter.

Interaction of Particles with Matter
The interaction of particles with matter involves several processes.

- **Ionization and Excitation of Electrons**
  Charged particles scattering off detector matter leads to excitation and ionization of electrons in the atomic shell. The energy loss per distance is described by the Bethe-Bloch formula and follows the proportional law:

$$-\frac{dE}{dx} \propto \frac{z^2}{m\beta^2} \left(\ln\left(\frac{\beta^2}{I\left(1 - \beta^2\right)} \right) - \beta^2 \right) \quad , \tag{2.3}$$

  where z is the charge of the scattered particle, m its mass, $\beta = v/c$ its speed in units of the speed of light c and I is the mean excitation energy of the target matter. For an atomic nucleus with a number of protons $Z > 20$, $I/Z \approx$ const. This type of energy deposit is most important for tracking detectors.

- **Coulomb Scattering**
  Charged particles, which pass through matter, scatter in the Coulomb fields of the atomic nuclei. The energy loss is small, but the particles get deflected. Since the angular distribution of the deflected particles is smeared by large tails, this effect worsens the track reconstruction of detectors at collider experiments. Therefore it is attempted to keep the amount of detector material as small as possible. This effect is important for low particle momenta.

- **Bremsstrahlung**
  It is the dominant process of energy loss of charged particles with low rest mass M_0, i.e. primarily electrons. An electron retains $1/e$ of its energy after one radiation length X_0, where e is the Euler number, $X_0 \propto 1/Z^2$ and Z is the number of protons in the atomic nuclei.

- **Inelastic Scattering**
  If one or both scattering particles is a composite one, e.g a proton or a nucleus, the particles constituents can absorb collision energy. If that energy transfer Q is large enough, the constituent can produce other hadrons. The mean free path length required to reduce the number of relativistic charged particles by the factor of $1/e$ as they pass through matter is given by the nuclear interaction length λ. This quantity includes elastic processes, that lead to diffraction, resulting in a longer mean free path, than when only inelastic scattering is considered.

- **Photon Absorption**
  The photon absorption in matter is highly energy dependent. It follows the exponential law with the radiation length X_0 as slope parameter, where $X_0 = 7/9$ of the mean free path of a photon in matter. Photon absorption involves the photoelectric effect, Compton scattering and electron-positron pair production, which leads to electromagnetic showers.

- **Cherenkov Radiation**
  The Cherenkov Effect describes the emittance of electromagnetic radiation when a particle with velocity $\vec{v}$ larger than the speed of light in the material passes through matter with a refractive index n. Cherenkov radiation is emitted if $|\vec{v}| = v > c_{\mathrm{med}} = \frac{c}{n}$ or $\beta > \frac{1}{n}$, where c_{med} is the speed of light inside the medium and $\beta = \frac{v}{c}$. The angle θ, under which the radiation is emitted, is given through the relation $\cos\theta = \frac{1}{\beta n}$. Therefore the measurement of this angle θ allows to determine the particle's velocity. Furthermore, the invariant mass of the particle can be determined, if the particle's momentum $\vec{p}$ is known. This effect is used by the RICH detectors of LHCb in order to assign kaon and pion hypotheses (see chapter 3.1.1 and 3.1.2).

2.2 The Double Parton Scattering (DPS) Model

At the LHC pp collisions containing hard parton interactions allow the usage of the QCD factorization theorem in order to convert the cross sections in terms of fundamental particles to cross sections in dependence of the colliding protons. This conversion results in [9]:

$$\frac{d\sigma}{dQ^2\,dy} = \sum_{ab} \int_{x_A} d\xi_A \int_{x_B} d\xi_B \; f_{a/A}(\xi_A, \mu_F^2) \; \hat{\sigma}_{ab}(\xi_a, \xi_b, \mu_F^2, \mu_R^2) \; f_{b/B}(\xi_B, \mu_F^2) \quad , \quad (2.4)$$

The indices a, b denote the particle species considered, i.e. a quark or a gluon. A, B denote the collided hadron species, i.e. two protons such that $A = p$, $B = p$, and $f_{a/A}(\xi_A, \mu_F^2)$, $f_{b/B}(\xi_B, \mu_F^2)$ are the parton distribution functions. These are the distributions of the partons a and b in the hadrons A and B carrying the momentum fractions ξ_a and ξ_b, that is evaluated at the QCD factorization scale μ_F. This QCD factorization yields a solid description of processes where the main production is of the form:

$$\sum_{ab} \to S + X \quad , \quad (2.5)$$

where S is the process of interest, i.e. the D meson production and X is the summarization of additional final state particles from the remainder of the hadron. All processes that can be described by this scheme are referred to as SPS.

In processes where more than one parton from each interacting hadron is involved, a generalized ansatz in form of the DPS model was proposed [10], [11], [12], [13]. It relies on the following simplifications. First, the meaning of A, B is changed to $S = A + B$. Additionally, factorization between the hard processes and A, B is assumed, such that the n-point function with four partons in the initial state becomes trivial. When considering a final state consisting of the products of two hard parton interactions A and B, where e.g. $A, B = W, Z, jj, ...$, the description of the cross section is given by:

$$\sigma_{\text{DPS};(A,B)} = \alpha \sum_{i,j,k,l} \int dx_1 \; dx_2 \; dx_1' \; dx_2' \; d^2b$$
$$\Gamma_{i,j}(x_1, x_2, b; t_1, t_2) \; \Gamma_{k,l}(x_1', x_2', b; t_1, t_2) \quad (2.6)$$
$$\hat{\sigma}_{A;\,i,k}(x_1, x_1') \; \hat{\sigma}_{B;\,j,l}(x_2, x_2') \quad .$$

$\Gamma_{i,j}(x_1, x_2, b; t_1, t_2)$, $\Gamma_{k,l}(x_1', x_2', b; t_1, t_2)$ represent the generalized double parton distribution functions and x_1, x_2, x_1', x_2' are the longitudinal momentum fractions for the hard parton interactions A, B. $\hat{\sigma}_{A;i,k}(x_1, x_1')$, $\hat{\sigma}_{B;j,l}(x_2, x_2')$ are the parton cross sections, which can be determined by QCD. The characteristic scales of the subprocesses A, B, t_1, t_2 are given by $t_1 = \ln Q_1^2$, $t_2 = \ln Q_2^2$, where Q_1, Q_2 are the corresponding four-momentum transfers. The transverse separation distance of the two parton interactions A, B is denoted as b, and α is a combinatorial factor. $\alpha = \frac{1}{4}$ if A and B are identical and non-self-conjugate (e.g. $D^0 D^0$),

$\alpha = 1$ if A and B are different and either A or B is self-conjugate (e.g. $J\psi D^0$) and $\alpha = \frac{1}{2}$ otherwise (e.g. $D^+ D^+$) [1].

First, it is assumed, that $\Gamma_{i,j}$ may be decomposed in terms of longitudinal and transverse components:

$$\Gamma_{i,j}(x_1, x_2, b; t_1, t_2) = D_h^{ij}(x_1, x_2; t_2, t_2) \, F_j^i(b) \quad . \tag{2.7}$$

Further, the $F_j^i(b)$ are assumed to be the same for all parton pairs ij involved in the process of interest. Finally, it is assumed, that the longitudinal momentum correlations can be ignored, such that the D_h^{ij} factorize as:

$$D_h^{ij}(x_1, x_2; t_2, t_2) = D_h^i(x_1; t_1) \, D_h^j(x_2; t_2) \quad . \tag{2.8}$$

Using these three simplifications, equation 2.6 can be rewritten as:

$$\sigma_{\text{DPS};(A,B)} = \alpha \, \frac{\sigma_{\text{SPS};A} \, \sigma_{\text{SPS};B}}{\sigma_{\text{eff}}} \quad , \tag{2.9}$$

where SPS denotes the single parton scattering, and the effective cross section σ_{eff} is given by:

$$\sigma_{\text{eff}} = \left(\int d^2 b \, \left(F_j^i(b) \right)^2 \right)^{-1} \quad . \tag{2.10}$$

The approximations imply that the hard parton interactions are independent from each other. They also violate energy conservation. Formula 4.2 is not justified, if the flavour of the partons or the momentum fractions make a difference in the studied processes. Nevertheless, this ansatz is phenomenologically successful and leads to an energy independent result for the effective cross section σ_{eff} [14], [15] [16], [17]. Formula 4.2 does not rely on theoretical predictions for the SPS cross section $\sigma_{\text{SPS};A}$ and $\sigma_{\text{SPS};B}$, since there is no explicit depencence on the parton distribution functions. Therefore, this model can be used in regimes, where the uncertainty on the production cross section $\sigma_{(A,B)}$ is high, by using measurements of σ_A and σ_B.

---

[1]The convention for α follows the addendum of [2] instead of the notation in [10].

3 Foundations: LHC Collider, LHCb Detector and Key Concepts for the Analysis

The Large Hadron Collider Beauty Experiment (LHCb) is one of the four main experiments at CERN, located at one of the four main collision points of the Large Hadron Collider (LHC) [19], [20]. The CERN, LHC accelerator and LHCb experiment are introduced in chapter 3.1, while chapter 3.1.1 explains the detector components of the LHCb experiment. In order to introduce the physical processes at the LHC accelerator and the LHCb experiment, the most important physical principles needed to understand the acceleration and detection of particles are explained in chapter 3.1.2.

3.1 The LHC at CERN

CERN is the abbreviation for the European Organization for Nuclear Research, literally Conséil Européen pour la Recherche Nucléaire. It was founded to plan the construction of a research laboratory for nuclear research [18]. The research started with the first accelerator in 1957, a synchro-cyclotron. Shortly afterwards it was followed by the Proton Synchrotron (PS), which accelerated the first beams in November 1959 and is still operational today. Since then an increasing amount of large accelerators has been built. The most recent two accelerators in the history of CERN are the Large Electron Positron Collider (LEP) and the Large Hadron Collider (LHC). The LEP accelerated electrons and positrons from 1989 to 2000, while the LHC started to accelerate protons in 2009 and is still operating today. It was planned from the start during the first LHC studies in the 1980's to reuse as much of the LEP infrastructure as possible for the LHC, mainly the LEP tunnel. Along with the increasing size and number of accelerators, the number of experiments and buildings grew more and more. Today the CERN is one of the largest institutions worldwide with about 10'000 visiting scientists representing over 600 universities and 100 nationalities.

The LHC accelerator is a proton proton collider with a circumference of 26.7 km. Its size and experimental infrastructure turns the LHC into the currently largest and most complicated scientific instrument in the world. The LHC is designed to be operated at a center of mass energy of $\sqrt{s} = 14$ TeV and an instantaneous luminosity of $L_{\mathrm{LHC}} = 2 \cdot 10^{32}$ cm^{-2}s^{-1}. It consists of eight arcs with a length of 2.8 km and eight straight sections with a length of 500 m each. The tunnel housing the LHC lies between 45 m and 170 m below the surface and has an inclination of 1.42% with respect to the horizontal

to enable an easier civil engineering. From 2010 to 2012 the LHC was operated at $\sqrt{s} = 0.45, 2.76, 5.02, 7$ and 8 TeV. To achieve such high center of mass energies, large bending magnets with a field strength of about 8 T are needed to keep the protons on track. This is achieved by superconducting magnets, which are cooled with superfluid helium at 1.9 K, implying the construction of a large cooling infrastructure with about 80 t of superfluid helium.

The LHC is the last piece of a complicated chain of accelerators to produce, bunch and accelerate the protons until they collide at one of the four collision points at the four main experiments. First, the protons are extracted as the nucleus of hydrogen atoms with an energy of 50 keV. Then they are guided to a linear accelerator (LINAC), where their energy is increased to 50 MeV. Afterwards they are injected into a booster synchrotron which increases their energy to 1.4 GeV. Subsequently, the protons arrive at the proton synchrotron (PS) where they are not only accelerated but also grouped into a train of bunches. This structure is kept until the proton beams finally collide in the LHC. The bunch-trains are injected into the super proton synchrotron (SPS) and are again accelerated, this time to the energy of 450 GeV. Then, they are transferred to the LHC ring via one of the transfer lines. After the filling of both counter rotating beams with bunch-trains, the protons are accelerated while the magnetic field in the bending dipoles is simultaneously rised until the collision energy is reached. Finally, the beams are brought to collision at the four collision points, where the four main detectors, Compact Muon Solenoid (CMS), A Toroidal LHC Apparatus (ATLAS), Large Hadron Collider Beauty Experiment (LHCb), A Large Ion Collider Experiment (ALICE) are situated. The beams can stay several hours in the LHC, if no technical problems occur, until they are finally dumped and the cycle is started again. This accelerator chain is shown in Fig. 3.1.

The locations, sizes and scopes of the four main experiments are different. ATLAS and CMS are general purpose detectors for high transverse momentum physics. LHCb is a b-physics experiment which focuses on CP-violation and rare decays of beauty and charm hadrons. It also performs analyses similar to ATLAS and CMS but in a different kinematic range, for example W and Z production. ALICE investigates primordial states of matter like the quark-gluon-plasma in heavy ion collisions.
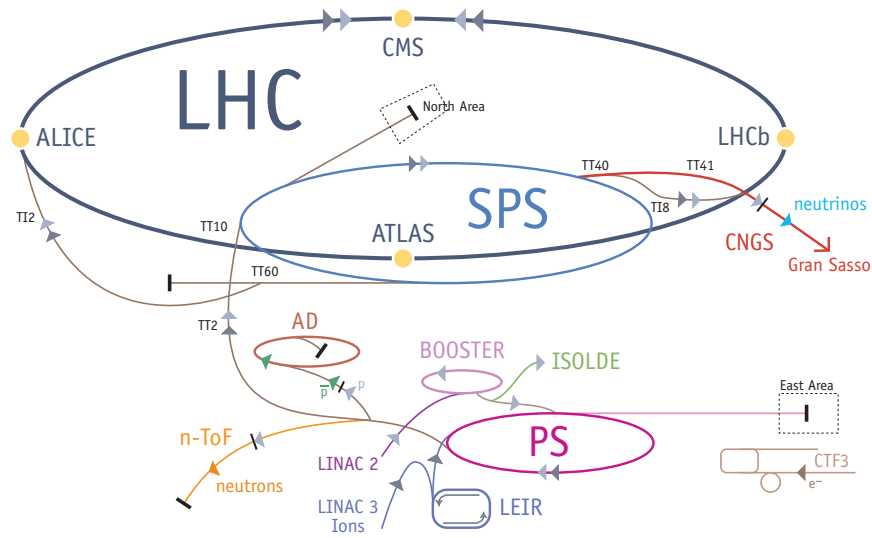
Figure 3.1: Schematic overview of the accelerator chain for the LHC at CERN. This chain is started with the extraction of the protons from hydrogen atoms, followed by a linear accelerator (LINAC2), a booster synchrotron (BOOSTER), Proton Synchrotron (PS), Super Proton Synchrotron (SPS) and the LHC (Figure taken from Ref. [21]).

3.1.1 The LHCb Detector

The LHCb detector is situated at one of the four main collision points of the LHC [22], [23]. It is a single-arm spectrometer with a forward geometry and is fully instrumented in the pseudorapidity range of $2 < \eta < 5$ (see Fig. 3.2, chapter 3.1.2).

The coordinate system for the LHCb is oriented, such that the positive z-axis points from the interaction point to the muon system along the beam pipe. The y-axis is vertical, starting from the interaction point to the surface, and is perpendicular to the LHC ring. The remaining x-axis, being perpendicular to the x- and y-axis, indicates where the bending of the dipole magnet is most pronounced. Its forward design arises from the fact, that b and $\bar{b}$ quarks are produced in pairs and predominantly in the forward (or backward) direction. Therefore the LHCb forward geometry allows to detect a large fraction of the produced particles containing a b or $\bar{b}$ quark, while covering a small solid angle, which helps reducing the costs.

The LHCb's subdetectors can be grouped into three parts. The track reconstruction system determines the three vector components of the particles' momenta $\vec{p}$. The purpose of the particle identification system is to determine the particle types. These two properties completely describe each detected individual particle and describe therefore a good part of the full event. Finally, the trigger system selects the events of interest for the physics analyses.

- **Track reconstruction**
  The track reconstruction system consists of a silicon microstrip detector called Vertex Locator (VELO), placed closely to the interaction point. It measures precisely the position of primary and secondary vertices as well as the impact parameter (IP) of the track. A second silicon microstrip detector, the Tracker Turicensis (TT), is located before the dipole magnet. Hits in the TT are used to improve the momentum resolution of reconstructed tracks and reject pairs of tracks that in reality belong to the same particle. The tracking stations (T1, T2, T3), placed behind the dipole magnet, use different technologies to detect particles: silicone microstrips close to the beam pipe and straw-tubes in the outer regions. The dipole magnet itself completes the track reconstruction system. Its magnetic field with vertical field lines bends the flight path of the particles in the xz - plane. Therefore the size of the magnetic field allows the determination of the patricles' momenta by comparision of the track direction before and after the magnet. All tracking detectors are characterized by a high spatial resolution (in one or two spatial coordinates) and a low material budget.

- **Particle identificaton**
  The particle identification system uses different physical principles. The two Ring Imaging Cherenkov Detectors (RICH1, RICH2) use the Cherenkov Effect to distinguish between different types of hadrons. The consecutive electromagnetic and hadronic calorimeters (ECAL, HCAL) measure the energy of the impinging particles by fully absorbing them. The ECAL absorbs all electromagnetic showers but only a small part of the hadronic showers, while hadronic showers are contained in the big-

ger HCAL. Two smaller subdetectors, the scintillating pad detector (SPD) and the preshower detector (PS), in front of the ECAL supplement the calorimeter system by resolving ambiguities on the identification. For instance, the SPD allows the discrimination of electron and photon candidates, while the PS is used to discriminate electron and photon candidates from hadron candidates. The muon system consists of five stations (M1 to M5) and is placed at the most remote position within the LHCb seen from the interaction point. It identifies muons, that traverse the detector and the iron shields between the muon stations almost unaffected.

- **Trigger**
  The LHCb detector produces too much information per collision for all of it to be read out. Moreover, many of the collisions are not of particular interest for physics analyses. Therefore the LHCb has a three stage trigger system to reduce the amount of data collected to a rate, which can be written to disk. The first level, called L0, is hardware based, while the second and third stage, HLT1 and HLT2, are software based and execute algorithms that partially reconstruct the event and then decide if they are of further interest or not.
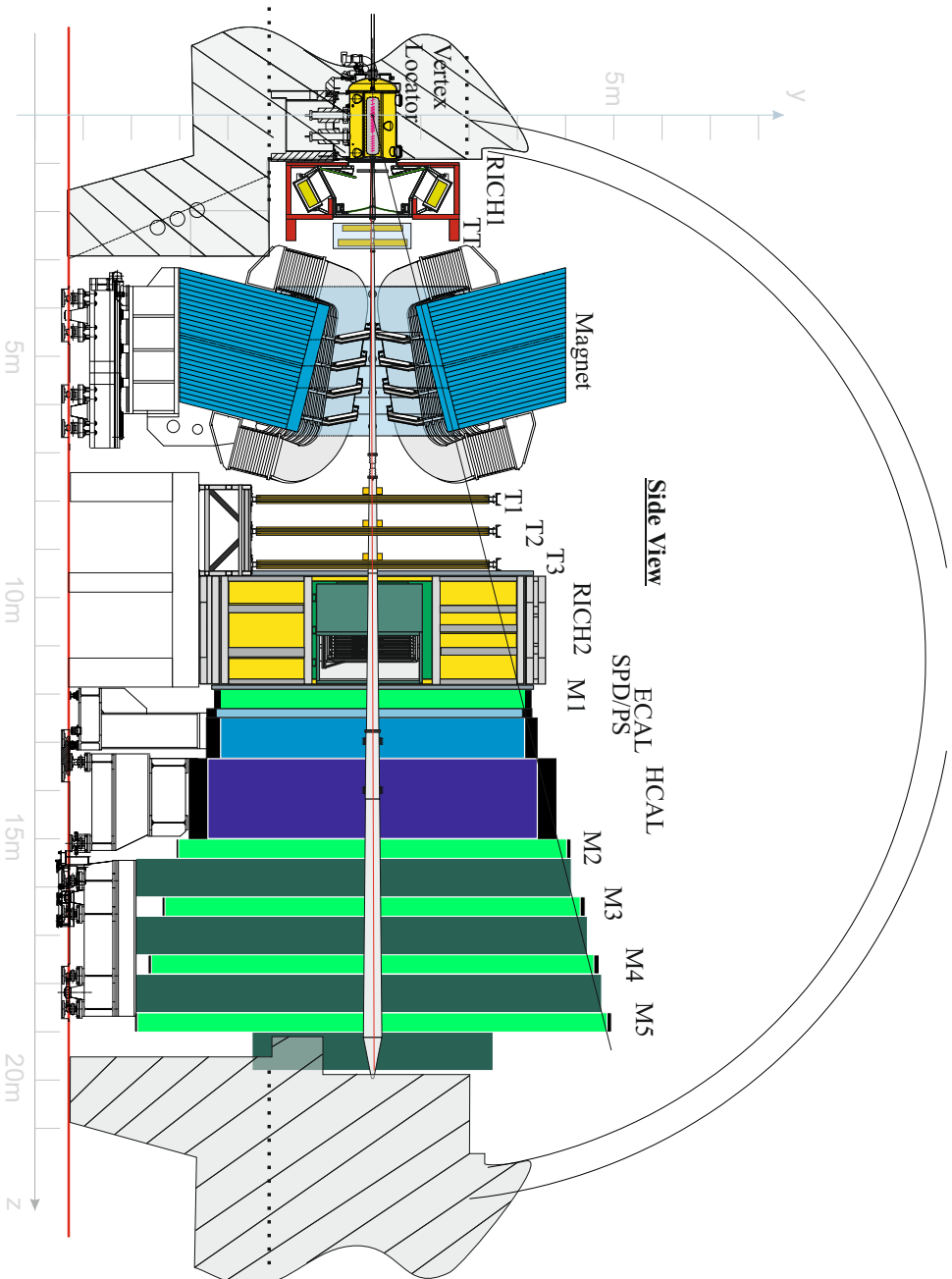
Figure 3.2: Schematic side view of the LHCb detector. The different subdetectors are from the left to the right in the forward beam direction: The vertex locator (VELO), the two Ring Imaging Cherenkov Detectors (RICH1 and RICH2), the tracking stations (TT and T1-T3), the scintillator pad detector (SPD), the preshower (PS), the electromagnetic calorimeter (ECAL), the hadronic calorimeter (HCAL) and the muon stations (M1-M5). Figure taken from Ref. [22], [23].

3.1.2 Key Concepts for the Analysis

This analysis requires the understanding of some fundamental principles of experimental particle physics. The most important ones are explained in this section.

There are two major variables describing the dataset at hands: the center of mass energy s, also denoted as $\sqrt{s}$, and the luminosity L.

Center-of-Mass Energy $\sqrt{s}$

At the LHC, predominantly two protons are collided with each other. The LHC is in fact able to collide also heavy ions with each other or protons with heavy ions, but since such data is not used in this analysis, pp collision is assumed in the following. The two protons have the same rest mass $m_1 = m_2$ and the four-momenta $p^\mu_1 = (E_1/c\,,\,\vec{p_1})$, $p^\mu_2 = (E_2/c\,,\,\vec{p_2})$ where the energy $E_1 = E_2$ and momenta $\vec{p_1} = -\vec{p_2}$ are given in the center of mass frame and $c = 2.998 \cdot 10^8$ m/s is the speed of light. The Mandelstam variable s, also called center of mass energy, is defined by:

$$s = (p^\mu_1 + p^\mu_2)^2 = (E_1/c + E_2/c)^2 \quad . \tag{3.1}$$

Since $(p^\mu_1 + p^\mu_2)^2 = M^2 c^4$, s is the square of the invariant mass M. Natural units, where $\hbar = c = 1$, are used throughout this analysis. For clarity an explicit factor c is preserved in selected equations. The center of mass energy can also be denoted as square root and in natural units:

$$\sqrt{s} = (p^\mu_1 + p^\mu_2) = (E_1 + E_2) = M \quad . \tag{3.2}$$

The data used in this analysis were taken at a center of mass energy $\sqrt{s} = 2.76$ TeV.

Luminosity L

The luminosity is a measure of how many collisions happen when two bunches of particles collide with each other and is linked to the number of collisions and the cross section by:

$$\frac{dN}{dt} = L\ \sigma \quad ,$$

$$\text{where} \quad \frac{dN}{dt} : \text{number of collisions per second} \tag{3.3}$$

$$\sigma : \text{cross section}$$

$$L : \text{(instantaneous) luminosity}$$

For a gaussian beam distribution, the luminosity L is given by:

$$L = \frac{N_b^2 \, n_b \, f_{rev} \, \gamma}{4 \, \pi \, \epsilon_n \, \beta^*} \, F \quad ,$$

where N_b : number of particles per bunch

n_b : number of bunches per beam

f_{rev} : revolution frequency   (3.4)

γ : relativistic gamma factor

ϵ_n : normalized transverse beam emittance

β^* : Beta function at the collision point

F : geometrical luminosity reduction factor   .

The beta function at the collision point β^* is a measure of how compressed the beam is at the collision point. The normalized transverse beam emittance ϵ_n is a measure of the distribution of the particles in space and momentum. The geometrical luminosity reduction factor F takes into account, that the beams do not collide head on and arises due to the crossing angle at the collision point. The luminosity L has the units of inverse area and inverse time, given in by the SI units $\mathrm{m^{-2} \, s^{-1}}$ or more practical by $\mathrm{b^{-1} \, s^{-1}}$, where the unit barn is given by the relation $1\,\mathrm{b} = 10^{-28}\mathrm{m}^2$. The integrated luminosity given by $\mathscr{L} = \int L \, dt$ is a measure for the total amount of the aquired data. The used dataset corresponds to an integrated luminosity of $\mathscr{L} = 3.31 \, \mathrm{pb}^{-1}$.

Invariant Mass M

Since the velocity $\vec{v}$ is frequently close to c in particle physics, relativistic conservation laws for energy and momentum have to be used. The energy E and momentum $\vec{p}$ from classical mechanics are reformulated as the four-momentum p^μ, in order to adapt to Einstein's principles of relativity, implying Lorentz transformations and the introduction of the four-vector notation, when considering space-time translations (see [24], [25]). Consequently, the two conservation laws from classical mechanics are reformulated into one, called the (relativistic) energy-momentum conservation or four-momentum conservation:

$$\sum_i p^\mu = \text{const.} \quad ,$$

where $\quad p^\mu = \left(p^0, \vec{p}\right) = \gamma\, M\,(c, \vec{v}) \quad$ four-momentum

$x^\mu = (c\,t, \vec{x}) \quad$ (contravariant) four-position vector

$x^0 = ct \quad$ time component or zero component

$\vec{x}$: space component

$d\tau = \dfrac{dt}{\gamma} \quad$ proper time element

$\gamma = \dfrac{1}{\sqrt{1-\beta^2}}$

$\beta = \dfrac{\vec{v}^{\,2}}{c^2}$

(3.5)

M : invariant mass, also called rest mass in the particle's
   rest frame of reference

$E = p^0\, c = \gamma\, M\, c^2 \quad$ total energy

$E|_{\vec{v}=0} = E_0 = M\, c^2 \quad$ rest energy

$T = E - E_0 = M\, c^2\,(\gamma - 1) \quad$ kinetic energy $\quad$.

This holds under the condition of the Lorentz invariance of the four-momentum squared, p^2, resulting in the energy momentum relation:

$$p^2 \;=\; \langle p^\mu, p^\nu \rangle \;=\; \left(p^0\right)^2 - \vec{p}^{\,2} \;=\; \frac{E^2}{c^2} - \vec{p}^{\,2}$$

$$=\; \gamma^2 M^2 c^2 - \gamma^2 M^2 \vec{v}^{\,2} \;=\; M^2 \gamma^2 \left(c^2 - \vec{v}^{\,2}\right) \;=\; M^2 \frac{1}{1 - \frac{\vec{v}^{\,2}}{c^2}} \left(c^2 - \vec{v}^{\,2}\right) = M^2 c^2 \quad ,$$

where $\quad \langle x^\mu, y^\nu \rangle \;=\; \displaystyle\sum_{\mu=0}^{3}\sum_{\nu=0}^{3} g_{\mu\nu} x^\mu y^\nu \;=\; g_{\mu\nu} x^\mu y^\nu \;=\; x^\mu y_\mu \;=\; x^0 y^0 - \vec{x} \cdot \vec{y}$

(3.6)

$$g_{\mu\nu} = g^{\mu\nu} = \begin{pmatrix} 1 & 0 & 0 & 0 \\ 0 & -1 & 0 & 0 \\ 0 & 0 & -1 & 0 \\ 0 & 0 & 0 & -1 \end{pmatrix} \quad \text{Metric Tensor} \quad .$$

Simpler: $\quad E^2 \;=\; M^2 c^4 + \vec{p}^{\,2} c^2$

Therefore the invariant mass M is the same in all inertial frames of reference. In the rest frame of the particle, the invariant mass M is equal to the energy E of the particle (divided by c^2) and is called rest mass.

Consider a particle, which decays into N daughter particles. Since the four-momentum p^μ is conserved, the invariant mass of the decay particle, M, can be calculated as a sum of the energies and momenta of the daughter particles using the energy-momentum relation:

$$\left(Mc^2\right)^2 = \left(\sum_i^N E_i\right)^2 - \left(\sum_i^N \vec{p}_i\, c\right)^2 \quad,$$

where M : Invariant mass of the system of particles,
                 equal to the invariant mass of the decay particle
            E_i : Energy of the daughter particle i
            $\vec{p}_i$: Momentum of the daughter particle i
            $c = 2.998 \cdot 10^8\,\mathrm{m/s}$ Speed of light; when natural units are used: $\hbar = c = 1$
                                                                                                 (3.7)

For one particle that decays into two daughter particles this relation becomes:

$$M^2 c^4 = (E_1 + E_2)^2 - (\vec{p}_1 + \vec{p}_2)^2 = m_1^2\, c^4 + m_2^2\, c^4 + 2\left(E_1\, E_2 - \vec{p}_1\, \vec{p}_2\, c^2\right) = (p^\mu{}_1 + p^\mu{}_2)^2 \quad,$$

where $m_{1,2}$: invariant masses of the daughter particles
            $E_{1,2}$: energies of the daughter particles
            $p^\mu{}_{1,2}$: four momenta of the daughter particles   .
                                                                                                 (3.8)

This concept is applied in this work by starting from experimentally reconstructed tracks which correspond to a measurement of $\vec{p}$. Using other subdetectors, those tracks get a Pion or Kaon hypothesis assigned. This leads to particle candidates with $p^0 = E$ determined by $p^2 = m_K^2$ or $p^2 = m_\pi^2$. D meson candidates are formed by adding the momenta of the decay products, e.g. for D^0, D^+: $p^\mu_{D^0} = p^\mu_{K^-} + p^\mu_{\pi^+}$, $p^\mu_{D^+} = p^\mu_{K^-} + p^\mu_{\pi^+} + p^\mu_{\pi^+}$. The comparison to the known D mass provides a discriminant with respect to other processes.

Transverse Momentum p^T, Longitudinal Momentum p_L

As two protons collide at the LHCb interaction point, they form a PV, of which a bunch of particles with momentum $\vec{p}_i$, $i \in \{1, ..., n\}$ emerge. Each momentum $\vec{p}_i$ can be decomposed into the transverse momentum $\vec{p}_i^{\,T}$ perpendicular to the beam axis and the longitudinal momentum $\vec{p}_{i_L}$ along the beam axis. The same principle holds for the energies E_i, $i \in \{1, ..., n\}$, and consequently for the four momenta p^μ, $i \in \{1, ..., n\}$. Moreover such a decomposition can be applied at each vertex.
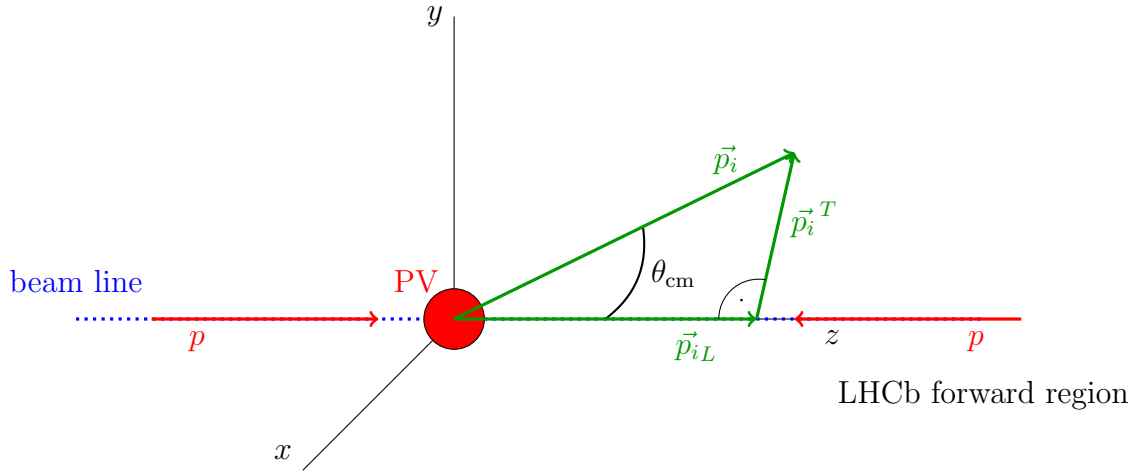
Figure 3.3: Schematic illustration of the decomposition of the momentum of a particle $\vec{p}_i$ emerging from a PV into longitudinal- and transverse momentum $\vec{p}_{i_L}$ and $\vec{p}_i^{\,T}$.

Pseudorapidity η and Rapidity y

The longitudinal pseudorapidity η of a particle is defined as:

$$\eta := -\ln\left(\tan\left(\frac{\theta_{\mathrm{cm}}}{2}\right)\right) = \frac{1}{2}\ln\left(\frac{|\vec{p}| + |\vec{p}_L|}{|\vec{p}| - |\vec{p}_L|}\right) = \arctan\left(\frac{|\vec{p}_L|}{|\vec{p}|}\right) \quad . \qquad (3.9)$$

The longitudinal momentum p_L is the momentum component along the beam axis, given along the positive z-axis in the forward coordinate system of LHCb. θ_{cm} is the scattering angle between the momentum of the particle in question, $\vec{p}$, and the beam axis (z-axis). The pseudorapidity is a commonly used variable at hadron colliders. It is defined as the high relativistic limit of the longitudinal rapidity y, given by:

$$y := \arctan\left(\frac{\vec{v}}{c}\right) = \arctan\left(\frac{|\vec{p}_L|\,c}{E}\right) = \frac{1}{2}\ln\left(\frac{E + |\vec{p}_L|c}{E - |\vec{p}_L|c}\right) \quad . \qquad (3.10)$$

In the relativistic limit $\vec{p} \approx E$ or $M << p^T$, the pseudorapidity η is a good approximation of the longitudinal rapidity y, i.e. $\eta \approx y$. Experimentally, these quantities have the following advantages compared to the angle. Differences in rapidity or pseudorapidity are

Lorentz invariant under boosts along the beam axis, i.e. they transform additively, similar to velocities under Galilean transformations. Loosely spoken, the particle production is constant as a function of rapidity (and pseudorapidity, if the mass of the particle is negligible compared to its energy). The pseudorapitiy is a pure geometrical quantity and only related to the scattering angle θ_{cm}. When the interaction point is fixed, each detector element can get a pseudorapidity value assigned. Consequently, the LHCb detector elements are positioned at high η, which allows the measurements of particles produced at high rapidity y.

Impact Parameter IP

It is defined as the shortest distance of a track to the PV. It is schematically illustrated in Fig. 3.4 for the example of a D^0 candidate promptly produced in the PV with decay mode $D^0 \to K^- \pi^+$, resulting in a Kaon and a Pion track. The reconstruction of the D^0 candidate yields usually also a non-zero but very small IP for the D^0. Candidates produced in PV's can be distinguished from the ones produced in SV's by applying a specific cut on the impact parameter for the candidate.
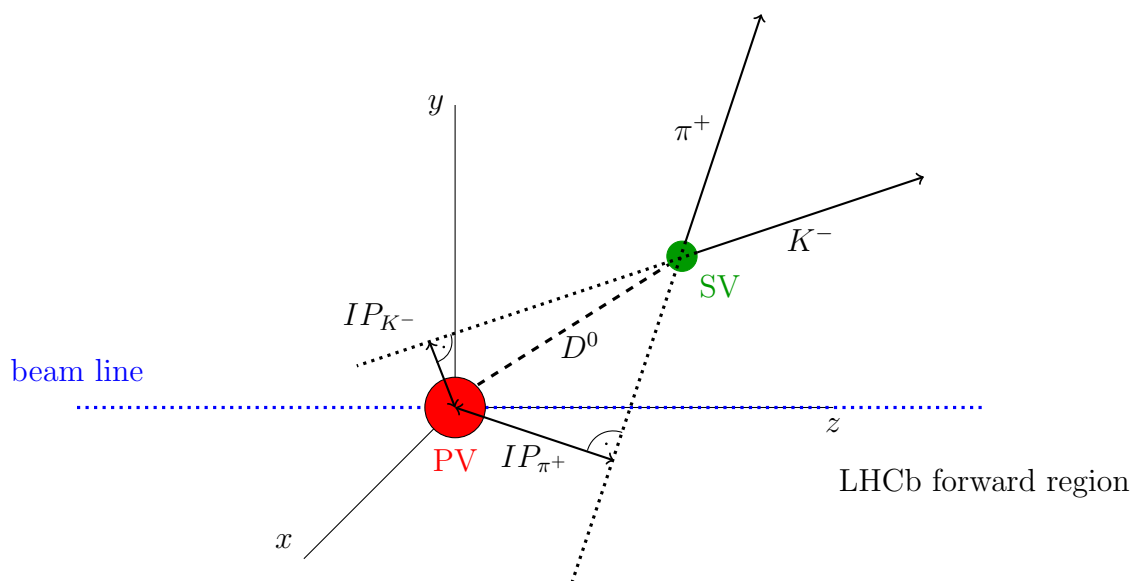

Figure 3.4: Schematical illustration of the impact parameter (IP) using the example of a D^0 candidate promptly produced in a PV with decay mode $D^0 \to K^- \pi^+$.

Branching Fraction or Branching Ratio B_i

The Branching fraction for a certain decay is the fraction of particles, which decay by an individual decay mode i, N_i, with respect to the total number of particles decaying, N_{tot}, given by:

$$B_i = \frac{N_i}{N_{\text{tot}}} \quad .$$

(3.11)

For instance, the charmed meson D^0 has a branching fraction of $B_{D^0 \to K^- \pi^+} = 3.93\%$ for the decay mode $D^0 \to K^- \pi^+$ and $B_{D^0 \to K^+ \pi^-} = 1.49 \cdot 10^{-4}$ for $D^0 \to K^+ \pi^-$.

Hypothesis Testing

In chapter 4.4, three goodness of fit criteria are imposed in order to estimate the fit quality of unbinned maximum likelihood fits to tracks, vertices, envent hypotheses and invariant mass distributions. Moreover, χ^2/n_{dof} values are used by the different reconstruction softwares to estimate the goodness of fits in chapter 4.2.1. These criteria are explained in the following (see also [26], [27]).

1) Reduced χ^2, i.e. χ^2/n_{dof}:
   Assume an unbinned one-dimensional distribution of an observable x that has been fitted by an unbinned maximum likelihood fit with a model $f(x)$. Furthermore assume a subsequently applied binning to the distribution. The reduced χ^2 value is given by:

$$\chi^2/n_{\text{dof}} = \frac{1}{n_{\text{dof}}} \sum_i \frac{(y(x_i) - f(x_i))^2}{\sigma_{y(x_i)}^2} \quad ,$$

   where $y(x_i)$: y-value of a data point or bin at position x_i

(3.12)

   $f(x_i)$: fit function value at the position x_i

   $\sigma_{y(x_i)}$: error on $y(x_i)$.

   The number of degrees of freedom is given by $n_{\text{dof}} = n_b - n_p$, where n_b is the number of bins or data points and n_p is the number of fit parameters that had to be determined.

2) Upper tail probability or upper P-value of the χ^2 distribution, $P_u(\chi^2, n_{\text{dof}})$:
   This quantity is given by:

$$P_u(\chi^2, n_{\text{dof}}) = \frac{1}{2^{\frac{n_{\text{dof}}}{2}} \Gamma\left(\frac{n_{\text{dof}}}{2}\right)} \int_{\chi^2}^{\infty} t^{\frac{n_{\text{dof}}}{2} - 1} e^{-\frac{t}{2}} \, dt$$

   where χ^2 : χ^2 value (see equation 3.12)   ,

   n_{dof} : number of degrees of freedom

   $\Gamma(z) = \int_0^{\infty} t^{z-1} e^{-t} \, dt$ Gamma function (Euler's integral form)   .

(3.13)

It denotes the probability to observe a χ^2-value, that is greater than the given χ^2-value, provided the underlying hypothesis is true. Its analogon is the lower tail probability or lower P-value, $P_l(\chi^2, n_{\mathrm{dof}})$, representing the probability to observe a χ^2 value, that is smaller than the given one. It is given by:

$$P_l(\chi^2, n_{\mathrm{dof}}) \;=\; \frac{1}{2^{\frac{n_{\mathrm{dof}}}{2}} \, \Gamma\!\left(\frac{n_{\mathrm{dof}}}{2}\right)} \int_0^{\chi^2} t^{\frac{n_{\mathrm{dof}}}{2} - 1} \; e^{-\frac{t}{2}} \; dt \quad . \tag{3.14}$$

$P_u(\chi^2, n_{\mathrm{dof}})$, $P_l(\chi^2, n_{\mathrm{dof}})$ are connected to the χ^2 distribution, whose probability density function (PDF) is given by:

$$\chi^2(x; n_{\mathrm{dof}}) \;=\; \frac{1}{2^{\frac{n_{\mathrm{dof}}}{2}} \, \Gamma\!\left(\frac{n_{\mathrm{dof}}}{2}\right)} \; x^{\frac{n_{\mathrm{dof}}}{2} - 1} \; e^{-\frac{x}{2}} \quad . \tag{3.15}$$

The cumulative distribution function (CDF) of the χ^2 distribution, $C(\chi^2(x; n_{\mathrm{dof}}))$, can be splitted into $P_u(\chi^2, n_{\mathrm{dof}})$, $P_l(\chi^2, n_{\mathrm{dof}})$ by:

$$\begin{aligned}
C(\chi^2(x; n_{\mathrm{dof}})) \;&=\; \frac{1}{2^{\frac{n_{\mathrm{dof}}}{2}} \, \Gamma\!\left(\frac{n_{\mathrm{dof}}}{2}\right)} \int_0^{\infty} t^{\frac{n_{\mathrm{dof}}}{2} - 1} \; e^{-\frac{t}{2}} \; dt \\
&=\; \frac{1}{2^{\frac{n_{\mathrm{dof}}}{2}} \, \Gamma\!\left(\frac{n_{\mathrm{dof}}}{2}\right)} \left(\int_0^{\chi^2} t^{\frac{n_{\mathrm{dof}}}{2} - 1} \; e^{-\frac{t}{2}} \; dt \;+\; \int_{\chi^2}^{\infty} t^{\frac{n_{\mathrm{dof}}}{2} - 1} \; e^{-\frac{t}{2}} \; dt \right) \\
&=\; P_l(\chi^2, n_{\mathrm{dof}}) \;+\; P_u(\chi^2, n_{\mathrm{dof}}) \quad .
\end{aligned} \tag{3.16}$$

The χ^2 PDF is a special case of the Gamma PDF, given by:

$$G(x; b, p) \;=\; \frac{b^p}{\Gamma(p)} \; x^{p-1} \; e^{-bx} \quad , \tag{3.17}$$

when its free parameters $b > 0$ and $p > 0$ are defined as $b = 1/2$, $p = n_{\mathrm{dof}}/2$. Since the Gamma CDF, $C(G(x; b, p))$, can be expressed as a form of the lower regularized incomplete Gamma function $\gamma_l(x; k)$ by:

$$C(G(x; b, p)) = \frac{\gamma_l(b\,x,\, p)}{\Gamma(p)} \;=\; \frac{1}{\Gamma(p)} \int_0^{b\,x} t^{p-1} e^{-t} \; dt \quad , \tag{3.18}$$

all so far mentioned CDF's are forms of the lower- or upper regularized incomplete Gamma functions $\gamma_l(x, k)$, $\gamma_u(x, k)$, especially $P_l(\chi^2, n_{\mathrm{dof}})$, $P_u(\chi^2, n_{\mathrm{dof}})$.

3) Pull values p_i:
   Assume an unbinned one-dimensional distribution of an observable x, that has been fitted by an unbinned maximum likelihood fit with a model $f(x)$. Moreover assume a subsequently applied binning to the distribution. The pull value p_i of a certain bin

i is defined by:

$$p_i = \frac{y(x_i) - f(x_i)}{\sigma_{y(x_i)}} \quad ,$$

where $y(x_i)$: y-value of a data point or bin at position x_i (3.19)

                      $f(x_i)$: fit function value at the position x_i

                      $\sigma_{y(x_i)}$: error on $y(x_i)$.

The calculated pull values for all bins, p_i, result in a pull distribution.

4 Cross Section Determination

The so far measured double open charm production cross sections in pp collisions at LHCb at $\sqrt{s} = 7$ TeV (see [2], [3]) are supplemented by such a measurement at $\sqrt{s} = 2.76$ TeV. The LHCb experiment collected data from pp collisions at a center of mass energy of $\sqrt{s} = 2.76$ TeV and with an integrated luminosity of $\mathscr{L} = 3.3$ pb^{-1} during the time period starting from Feb. 12, 2013 until Feb. 14, 2013. After this period, the LHC and all associated experiments were shut down for maintenance and upgrades.

One group of particle candidates, which can originate from pp interactions are the ones, that contain at least a charm quark, the charm hadrons C. One subgroup thereof is the group of the charm mesons, the other is the group of the charm baryons. Typical elements in the group of charm mesons are the $D^0 = c\bar{u}$, $\bar{D} = \bar{c}u$, $D^+ = c\bar{d}$, $D^- = c\bar{d}$ particles. Such charm mesons can also occur twice as CC. When this doublet contains two charm quarks or two anti-charm quarks, it is referred to as double open charm production, when it comprises a charm and an anti-charm quark, it is referred to as charm pair production. For this analysis the notation of a charm state C includes its anti-particle state $\bar{C}$. This implication of the full charge conjugation results in the fact, that e.g. $D^0 D^0$ denotes $\{D^0 D^0, \bar{D}^0 \bar{D}^0\}$, and $D^0 \bar{D}^0$ denotes $\{D^0 \bar{D}^0, \bar{D}^0 D^0\}$.

The main objective of this analysis is to measure the production cross sections for the single open charm mesons C, double open charm mesons CC and charm pair produced mesons $C\bar{C}$, where $C \in \{D^0, D^+\}$, $\bar{C} \in \{\bar{D}^0, D^-\}$. The determination of the production cross section at LHCb involves a chain of analyses. Chapter 4.1 provides the strategy of the measurement. The charm event candidates need to be identified and isolated from other particle candidates in the data. This is achieved by a system of selection criteria, explained in chapter 4.2. Moreover, it covers the pile-up and feed-down, being two typical background processes, especially when double open charm event candidates are involved. Chapter 4.3 gives an overview of the charm candidates passing the selections. The remaining chapters, i.e. chapter 4.4, 4.5, 4.6, 4.7, 4.8, deal with the different terms of the production cross section formula listed in chapter 4.1 (see equation 4.1). The final chapter 4.9 covers the calculation of the systematic uncertainties in the determination of the production cross section.

4.1 Analysis Strategy

The analysis strategy outlines the procedures, which need to be executed on the data collected by LHCb, in order to get a production cross section for the single open charm meson candidates D^0 and D^+ and double open charm event candidates $D^0 D^0$, $D^0 D^+$ and $D^+ D^+$. For comparison, the production cross sections for the charm pair production event candidates $D^0 \bar{D}^0$, $D^0 D^-$ and $D^+ D^-$ are also determined. This analysis strategy is based on the one described in [2], [3].

As a first step the LHCb detector collects electric signals, which are created by the interaction of particles with the matter of the detector components, and which form the unfiltered data. This data is passed through the data acquisition sytem (DAQ) of the LHCb detector, whose capabilities are mainly limited by the trigger, and is filtered, such that it can be stored permanently on hard disks. This filtering involves the trigger selection, in order to reduce the nominal interaction rate from about $20 - 30$ MHz to $1 - 15$ kHz. This process needs to be executed online, i.e. while the data was taken. Afterwards, the triggered data is stored on disk. All following processing steps are therefore executed offline, i.e. when the data taking was finished.

In a second step, the stored data is reconstructed using Reco14 and subsequently filtered by the Stripping21 algorithm. In this process, the charm event candidates C and CC, where $C \in \{D^0, D^+\}$ are created from their decay products, the K^- and π^+ track candidates. All these candidates are further selected, which is achieved by the stripping selection described in chapter 4.2.1. Due to the short lifetime of the open charm event candidates, they need to be reconstructed from their decay products. For this analysis the decay modes $D^0 \to K^- \pi^+$ and $D^+ \to K^- \pi^+ \pi^+$ are chosen, because they fulfill several requirements [7]. First, the decay modes result in a low number of daughter particles, such that the initial momentum splits into few decay products. Secondly, the branching ratio B_i of the decay modes need to be high enough, such that the corresponding reconstructed mesons are sufficient in numbers for a measurement. This is explained in more detail in chapter 4.3 and 4.4. Thirdly, the event candidates are supposed to be detected as precise as possible by the LHCb detector. This means, that all decay products can be detected directly and should be charged. Fourthly, the decay modes are flavour tagging, such that the charm candidate can be distinguished from its anti particle. This enables the differentiation between double open charm production and open charm pair production.

The third and final step of filtering is the offline selection. It consists of the selection needed to be applied, in order to match the definition of the efficiencies (see chapter 4.6). Most of the efficiencies, being acceptance $\varepsilon_{\mathrm{acc}}$, reconstruction and selection efficiency $\varepsilon_{\mathrm{rec}}$ and particle identification (PID) efficiency $\varepsilon_{\mathrm{PID}}$, are not calculated explicitly for this analysis, but taken from the analysis of associated production of Υ and open charm [28], [29]. In order for the efficiencies to be applicable, the same selection as for the efficiency calculation done in the analysis [28], [29] needs to be applied for this analysis as described in chapter 4.2.1. An important difference to the previous works is, that [28], [29] did not trigger on the open charm, but on $\mu^{\pm}$. After the selection process, the different background contributions of pile-up and feed-down are investigated in chapter 4.2.2.

The production cross sections for the single open charm event candidates D^0, D^+ and the double open charm event candidates $D^0 D^0$, $D^0 D^+$, $D^+ D^+$ in pp collisions at LHCb can be calculated as:

$$\text{Single Charm:} \quad \sigma_C = \frac{N_{c;\,s;\,C}}{\mathscr{L}\ B_C\ \varepsilon_{\text{GEC};C}}$$

$$\text{Double Charm:} \quad \sigma_{CC} = \frac{N_{c;\,s;\,CC}}{\mathscr{L}\ B_C\ B_C\ \varepsilon_{\text{GEC};CC}} \quad,$$

where $\quad N_{c;\,s}$: efficiency corrected signal yield

$\mathscr{L}$: integrated luminosity

B : branching ratio

ε_{GEC} : global event cut efficiency

$C \in \{D^0, D^+\}$: single open charm event candidate(s)

CC , $C \in \{D^0, D^+\}$: double open charm event candidates .

$$(4.1)$$

The simple factorized ansatz of the DPS model (see chapter 2.2) predicts, that the effective cross section, σ_{eff} is constant and independent of the process and the center of mass energy $\sqrt{s}$. Assuming no contamination from soft processes, it is given by:

$$\sigma_{CC} = \alpha\,\frac{\sigma_C\,\sigma_C}{\sigma_{\text{eff}}} \quad,$$

where $\quad \sigma_C$, $C \in \{D^0, D^+\}$: cross sections for the single open charm

event candidates

σ_{CC} : cross-section for the double open charm event candidates

$$\alpha = \begin{cases} 1/4 & ,\ D^0 D^0,\ D^+ D^+ \\ 1/2 & ,\ D^0 D^+ \end{cases} \quad \text{combinatorial factor} \quad.$$

$$(4.2)$$

The measurements of $J/\psi C$ together with the predictions in [2], [3] suggest, that the contamination from the hard process $gg \rightarrow c\bar{c}c\bar{c}$ is indeed small. Formula 4.2 is sometimes referred to as Pocket Formula. It can be solved for σ_{eff} leading to:

$$\sigma_{\text{eff}} = \alpha\,\frac{\sigma_C\,\sigma_C}{\sigma_{CC}} \quad. \tag{4.3}$$

Being a ratio of cross sections, this equation has the advantage, that several systematic uncertainties both in experimental determination as well as in theory calculations do cancel out. The calculation of the terms, which arise in equation 4.1, are explained in chapters 4.4, 4.5, 4.6, 4.7, 4.8.

4.2 Event Selection and Background Determination

In the following, the event selection is described, which includes the trigger selection, stripping selection for the Stripping21 algorithm and the offline selection. These selection processes are the first step in eliminating the background, and are explained in chapter 4.2.1. The influence of two specific types of background, called pileup and feed-down, on the signal of the charm event candidates is described in chapter 4.2.2. The second background elimination step is achieved by the calculation of the efficiency corrected yields $N_{c;s}$ in chapter 4.5.

4.2.1 Event Selection

The data from pp collisions collected by the LHCb detector with a center of mass energy of $\sqrt{s} = 2.76$ TeV has the production identification number 23836 and the run number interval [137147, 137312] [1]. This unfiltered data passes three selection steps.

The first step of selection is the trigger selection, which is done online. The data was taken with the trigger configuration key (TCK) 0x00A90046, a TCK that was used previously in the high integrated luminosity data taking at $\sqrt{s} = 8$ TeV in 2012. The trigger has three stages, the hardware stage L0 and the two software stages Hlt1 and Hlt2. The trigger selection relies on HCAL clusters in L0, a non prompt high p^T track in Hlt1 and the $D^0 \to K^-\pi^+$, $D^+ \to K^-\pi^+\pi^+$ candidates in Hlt2. The names of the trigger lines are L0Hadron for L0, Hlt1TrackAllL0 for Hlt1, Hlt2CharmHadD02KPi for D^0 resp. Hlt2CharmHadD2HHH for D^+ for Hlt2 and are listed in Tab. 4.1. One cut applied at the trigger level is $APT > 2$ GeV for the charm, which translates approximately to $p^T > 2$ GeV. Due to the calculation of the trigger efficiency (see chapter 4.6), every single open charm event candidate is required to be triggered on signal (TOS). In the case of double open charm or open charm pair production event candidates, at least one of the two single open charm event candidates is required to be TOS. Previous analyses, like [28], [29], benefit from using $\mu^\pm$ for the trigger. Compared to hadrons, like $K^\pm$ and $\pi^\pm$, muons are relatively easy to identify by the LHCb muon system and are much less freqent. Therefore the trigger has a lot more work to do when using the L0Hadron trigger instead of the L0Muon trigger. Consequently, the L0Hadron trigger involves harder global event cuts (GEC), in order to keep the readout rate of the trigger within the maximum permissible limit. Moreover, the trigger was not optimized for a low center of mass energy and low instantaneous resp. integrated luminosity, which can be an issue for this analysis. This issue and the resulting consequences are specified further in chapter 4.6, 4.9 and 5.

---

[1] This data can be found in the LHCb Dirac Bookkeeping system under
LHCb/Collision13/Beam1380GeV-VeloClosed-MagDown/Real Data/Reco14/
90000000 (Full stream)/FULL.DST
or in the LHCb run database by a search for the run number.

Candidate	Trigger stage	Trigger line
D^0, D^+	L0	L0Hadron
D^0, D^+	Hlt1	Hlt1TrackAllL0
D^0	Hlt2	Hlt2CharmHadD02KPi
D^+		Hlt2CharmHadD2HHH

Table 4.1: Trigger lines used for the selection of events matching the decay modes $D^0 \to K^-\pi^+$, $D^+ \to K^-\pi^+\pi^+$.

The two remaining selection steps, stripping- and offline selection, are done offline. The stripping selection consists of the Stripping21 algorithm implemented in the stripping LHCb software framework. The used stripping lines are StrippingD02KpiForPromptCharm, StrippingDForPromptCharm, StrippingDiCharmForPromptCharm. Stripping21 selects the triggered data according to the chosen decay modes and the stripping selection criteria, which help to reduce the background. The selection criteria of the stripping- and offline selection are combined into one set, which is splitted into three categories. The first category contains the selection criteria applied on the decay candidates of the decay modes $D^0 \to K^-\pi^+$, $D^+ \to K^-\pi^+\pi^+$, the K^- and π^+ meson candidates. The criteria can be structured in criteria for track reconstruction and PID:

- A good track reconstruction quality is ensured by requiring four criteria for each track event candidate.

  First, the $\chi^2_{\mathrm{trk}}/n_{\mathrm{dof}}$ provided by the track fit is $\chi^2_{\mathrm{trk}}/n_{\mathrm{dof}} < 3$. The track reconstruction software checks for hit patterns, which can form a potential K^- or π^+ track, and combines these hit patterns to track candidates using a fit, called track fit. Since the amount of measurement points is limited and the charged track candidates can scatter in the detector material, wrong combinations of hit patterns can be reconstructed as a track. In order to quantify the goodness of the track fit, the distances between the hit points and the track are summed up and divided by their experimental uncertainty and the number of degrees of freedom n_{dof}, yielding $\chi^2_{\mathrm{trk}}/n_{\mathrm{dof}} = \frac{1}{n_{\mathrm{dof}}} \sum \frac{y(x_i) - f(x_i)}{\sigma_{y(x_i)}}$ (see also chapter 3.1.2).

  Secondly, the transverse momentum is $p^{\mathrm{T}} > 0.25$ GeV.

  Thirdly, the track ghost probability has to be $\mathscr{P}_{\mathrm{tr}} < 0.5$. Ghost tracks are tracks, which are reconstructed from random hit points by mistake.

  Fourthly, to suppress any contribution from duplicate tracks created by the reconstruction, only candidates with a symmetric Kullback-Leibler divergence, Δ_{KL}, calculated with respect to all candidates in the event, of $\Delta_{\mathrm{KL}} > 5000$ are considered [30], [31], [32].

  In addition, K^-, π^+ used for the reconstruction of long lived charm particles, are required not to be produced in primary interaction vertices (PV). To ensure this, only

candidates with a χ^2 of the impact parameter, χ^2_{IP}, with respect to all reconstrcted PV's, of $\chi^2_{\mathrm{IP}} > 9$ are considered. At LHCb, the χ^2_{IP} is calculated as the increase of the χ^2_{vx} of the PV, if one additional track is added to the vertex fit. This can be approximated by $\chi^2_{\mathrm{IP}} \simeq \left(\frac{IP}{\sigma_{\mathrm{IP}}} \right)^2$.

- A PID of good quality is ensured by requiring the following criteria for each track event candidate.

  The track must have left a signal in the RICH detectors catched by its PID system, fulfilled by HASRICH = True [42].

  The momentum, p, required to be in the range 3.2 GeV $< p <$ 100 GeV and the pseudorapidity, η, within $2 < \eta < 4.9$ ensure a good acceptance in the RICH.

  To select well identified K^- (π^+), the combined probabilty of the K^- (π^+), $\mathscr{P}_{K^-}$ ($\mathscr{P}_{\pi^+}$) is required to be $\mathscr{P}_l < 0.1$, $l \in \{K^-, \pi^+\}$. This quantity is the output of an artificial neural net using mainly the Log-Likelihood, $\log \mathcal{L}$, of the K^-, π^+ hypothesis from the RICH reconstruction [42].

  In addition, the difference in the Log-Likelihood of the K^- hypothesis with respect to the π^+ hypothesis, $\Delta_{K^-/\pi^+} \log \mathcal{L}$, is required to be $\Delta_{K^-/\pi^+} \log \mathcal{L} > -5$. In order to quantify the hypothesis, the RICH and the calorimeters are used [42].

These selection criteria are summarized in Tab. 4.2.

Candiate(s)	Variable	Cut	LOKI functor
Track Reconstruction			
K^-, π^+	$\chi^2_{\text{tr}}/n_{\text{dof}}$	< 3	TRCHI2DOF
	p^{T} [GeV]	> 0.25	PT
	$\mathscr{P}_{\text{tr, gh}}$	< 0.5	TRGHOSTPROB
	Δ_{KL}	> 5000	CLONEDIST
	χ^2_{IP}	> 9	MIPCHI2DV
Particle Identification			
K^-, π^+	HASRICH	True	HASRICH
	p [GeV]	$3.2 < p < 100$	P
	η	$2 < \eta < 4.9$	ETA
K^-	$\mathscr{P}_{K^-}$	> 0.1	PROBNNK
	$\Delta_{K^-/\pi^+} \log \mathcal{L}$	> -5	PIDK
π^+	$\mathscr{P}_\pi$	> 0.1	PROBNNpi

Table 4.2: Selection criteria for the K^- and π^+ track candidates, used for the reconstruction of the single open charmed event candidates D^0 and D^+.

The selected K^- and π^+ are then combined to form the single open charm event candidates D^0, D^+ with corresponding decay modes $D^0 \to K^- \pi^+$, $D^+ \to K^- \pi^+ \pi^+$. The second category of selection criteria contains the criteria applied on these open charm event candidates. The criteria can be structured in criteria for the decay chain, the primary vertex (PV) and the pile-up resp. feed-down:

- The K^-, π^+ track candidates shall originate from the open charm event candidates. This is achieved by a vertex fit performed by the vertex reconstruction software, which combines the K^- and π^+ tracks to vertices. The goodness of this fit is estimated by the χ^2_{vx}, which is required to be $\chi^2_{\text{vx}} < 9$ for the D^0 and $\chi^2_{\text{vx}} < 25$ for the D^+ candidates.

  In addition, the transverse momentum of the open charm event candidates has to be within $2 < p_{\text{T}} < 20$ GeV, and the rapidity in the range $2 < y < 4.5$.

- To ensure that the charm meson candidates originate from a PV, the χ^2_{IP} of these candidates with respect to any of the reconstructed PV's is required to be $\chi^2_{\text{IP}} < 9$.

  Moreover, the decay time $c\tau$ of the candidates is required to be $c\tau > 100$ µm. This quantity is extracted from a lifetime fit, which calculates the distance between the

best PV and the decay vertex of the candidates. The PV is determined by the vertex fit as the vertex, which has the smallest distance to the interaction point. The best PV is the PV, which has the smallest χ^2_{vx}, calculated by the vertex fit.

- In order to remove background from pile-up and feed-down (see chapter 4.2.2), it is required, that the momentum direction is consistent with the flight direction calculated from the PV's and SV's. This is acquired by a decay tree fit performed by the DecayTreeFitter tool, which combines vertices to decay chains for the candidates [33]. The $\chi^2_{\text{dtf}}/n_{\text{dof}}$ of this fit gives an estimate of its goodness and is required to be $\chi^2_{\text{dtf}}/n_{\text{dof}} < 5$.

  The invariant mass window for the open charm event candidates of $1.820 < M_C < 1.920$ GeV, where $C \in \{D^0, D^+\}$, is applied.

The selection criteria for the single open charm event candidates are summarized in Tab. 4.3.

Candidate	Variable	Cut	LOKI functor
D^0	χ^2_{vx}	< 9	VFASPF(VCHI2)
	p_T [GeV]	$2 < p^T < 20$	PT
	y	$2 < y < 4.5$	RAP
	χ^2_{IP}	< 9	MIPCHI2DV
	$c\tau$ [μm]	> 100	BPVLTIME(9) $\cdot$ c_light
	$\chi^2_{\text{dtf}}/n_{\text{dof}}$	< 5	DTF_CHI2NDOF
	M [GeV]	$1.820 < M < 1.920$	M
D^+	χ^2_{vx}	< 25	VFASPF(VCHI2)
	p_T [GeV]	$1 < p^T < 20$	PT
	y	$2 < y < 4.5$	RAP
	χ^2_{IP}	< 9	MIPCHI2DV
	$c\tau$ [μm]	> 100	BPVLTIME(9) $\cdot$ c_light
	$\chi^2_{\text{dtf}}/n_{\text{dof}}$	< 5	DTF_CHI2NDOF
	M [GeV]	$1.820 < M < 1.920$	M

Table 4.3: Selection criteria used for the selection of the single open charm event candidates D^0, D^+.

Subsequently, the selected single open charm event candidates D^0, D^+ are paired to form the double open charm event candidates $D^0 D^0$, $D^0 D^+$ and $D^+ D^+$. In addition, the charm pair production candidates $D^0 \bar{D}^0$, $D^0 D^-$, $D^+ D^-$ are studied. The third category

of selection criteria contains the sole criterium applied on these double open charm and charm pair production event candidates:

- In order to reject background from pile-up and feed-down, it is required, that the momentum direction is consistent with the flight direction calculated from the locations of the PV's and SV's. This is aquired analogously by the DecayTreeFitter tool as for the single open charm event candidates. The corresponding $\chi^2_{\mathrm{dtf}}/n_{\mathrm{dof}}$ is required to be $\chi^2_{\mathrm{dtf}}/n_{\mathrm{dof}} < 5$.

This selection criteria is listed in Tab. 4.4.

Candiate(s)	Variable	Cut	LOKI functor
$D^0 D^0$, $D^0 D^+$, $D^+ D^+$, $D^0 \bar{D}^0$, $D^0 D^-$, $D^+ D^-$	$\chi^2_{\mathrm{dtf}}/n_{\mathrm{dof}}$	< 5	DTF_CHI2NDOF

Table 4.4: Selection criterion used for the selection of the double open charm event candidates and charm pair production event candidates.

4.2.2 Pile-Up and Feed-Down

Sometimes it can happen, that two pp collisions occur too close for the detector to distinguish. This canal produces two D mesons falsely identified as double open charm and is referred to as pile-up. The background contributions from pile-up and feed-down in the data are treated using a method that exploits the cut on $\chi^2_{\mathrm{dtf}}/n_{\mathrm{dof}}$ [2], [3]. Events for which the two charm mesons come from the same PV, the following decomposition can be used:

$$\chi^2_{\mathrm{dtf}}/n_{\mathrm{dof}\ CC} \;=\; \chi^2_{\mathrm{dtf}}/n_{\mathrm{dof}\ C} \;+\; \chi^2_{\mathrm{dtf}}/n_{\mathrm{dof}\ C} \quad,$$

$$\text{where} \quad \chi^2_{\mathrm{dtf}}/n_{\mathrm{dof}} : \chi^2 \text{ per number of degrees of freedom} \tag{4.4}$$
$$\text{of the fit using the DecayTreeFitter tool [33]}$$

$$C \in \{D^0, D^+\} : \text{single open charm event candidates} \quad.$$

This identity is exact, if the position of the PV does not change, when the final state tracks (the K^-, π^+) of the charm meson candidates are successively removed, when the PV is refitted. Since the PV position does change a little, the identity is valid up to relatively small corrections. For pileup events, an additional contribution, the χ^2/n_{dof} of the decay-tree-fitter distance between the two PV's of the charm mesons, $\chi^2_{\mathrm{dtf}}/n_{\mathrm{dof}\ \mathrm{PV\text{-}dist}}$, adds to equation 4.4. This contribution is in general substantial, as for instance demonstrated for

the distance in the z-direction δz and its uncertainty $\sigma_{\delta z}$:

$$\chi^2_{\text{dtf}}/n_{\text{dof PV-dist}} = \left(\frac{\delta z}{\sigma_{\delta z}}\right)^2 + ... > \left(\frac{\delta z}{\sigma_{\delta z}}\right)^2 \approx \left(\frac{5 \text{ cm}}{0.2 \text{ mm}}\right)^2 = 6.25 \cdot 10^4$$

where $\quad \delta z$: Distance in z-direction of the two PV's $\hfill$ (4.5)

$\qquad\qquad$ for the charm meson candidates in the case of pileup

$\qquad \sigma_{\delta z}$: Uncertainty on the distance δz

Therefore, all events with $\log_{10}(\chi^2_{\text{dtf}}/n_{\text{dof }CC}) > 5$ can be treated as pileup up to the mentioned small corrections.

The contribution from pileup into the signal region $\chi^2_{\text{dtf}}/n_{\text{dof }CC} < 5$, equal to $\log_{10}(\chi^2_{\text{dtf}}/n_{\text{dof }CC}) \lesssim 0.7$, can be estimated by studying the shape of the $\chi^2_{\text{dtf}}/n_{\text{dof }CC}$ distribution separately in the pileup region $\log_{10}(\chi^2_{\text{dtf}}/n_{\text{dof }CC}) > 5$. From a fit to the $\chi^2_{\text{dtf}}/n_{\text{dof }CC}$ distribution in the pileup region, the contribution from pileup can be extracted and subsequently extrapolated into the signal region. This process is illustrated in Fig. 4.1 a), which shows the $\chi^2_{\text{dtf}}/n_{\text{dof}}$ distribution for $D^0 + Track$ candidates, fitted by a model consisting of four Gamma distributions, one each for the signal, the pile-up and the two feed-down peaks [34], [35].

The $\chi^2_{\text{dtf}}/n_{\text{dof }CC}$ distributions for this analysis are shown in Fig. 4.1 b), c), d). All $\chi^2_{\text{dtf}}/n_{\text{dof }CC}$ distributions contain no events in the pileup region $\log_{10}(\chi^2_{\text{dtf}}/n_{\text{dof }CC}) > 5$. Therefore it is concluded, that the pile-up contribution is negligible. Very low or no pile-up is expected, since the data are taken at low pile-up conditions with an average number of visible interactions of about one ($\mu \simeq 1$).

Another contribution of background, called feed-down, needs to be considered. The term feed-down is used, since charm mesons can originate from the decay of B mesons. Such a feed-down contribution is present in the $\chi^2_{\text{dtf}}/n_{\text{dof }CC}$ distribution at lower values than the contribution from pile-up, i.e. approximately in the region $\log_{10}(\chi^2_{\text{dtf}}/n_{\text{dof }CC}) \in [1, 4.5]$. D mesons originating from B decays do have a small but significant impact parameter with respect to the PV. Therefore with enough statistics, the pile-up and feed-down contributions are clearly distinguishable from each other (see Fig. 4.1 a)). All $\chi^2_{\text{dtf}}/n_{\text{dof }CC}$ distributions contain a few events in the feed-down region. These events can be excluded by the cut $\chi^2_{\text{dtf}}/n_{\text{dof }CC} < 5$, being equal to $\log_{10}(\chi^2_{\text{dtf}}/n_{\text{dof }CC}) \lesssim 0.7$. This cut allows the reduction of the feed-down contribution into the signal region to a negligible level. This contribution is estimated from simulation to be 1.7% for D^0, 1.3% for D^+ using the DPS approach (see [35], Fig. 4.1 a)), which is assigned as a systematic uncertainty for this analysis.
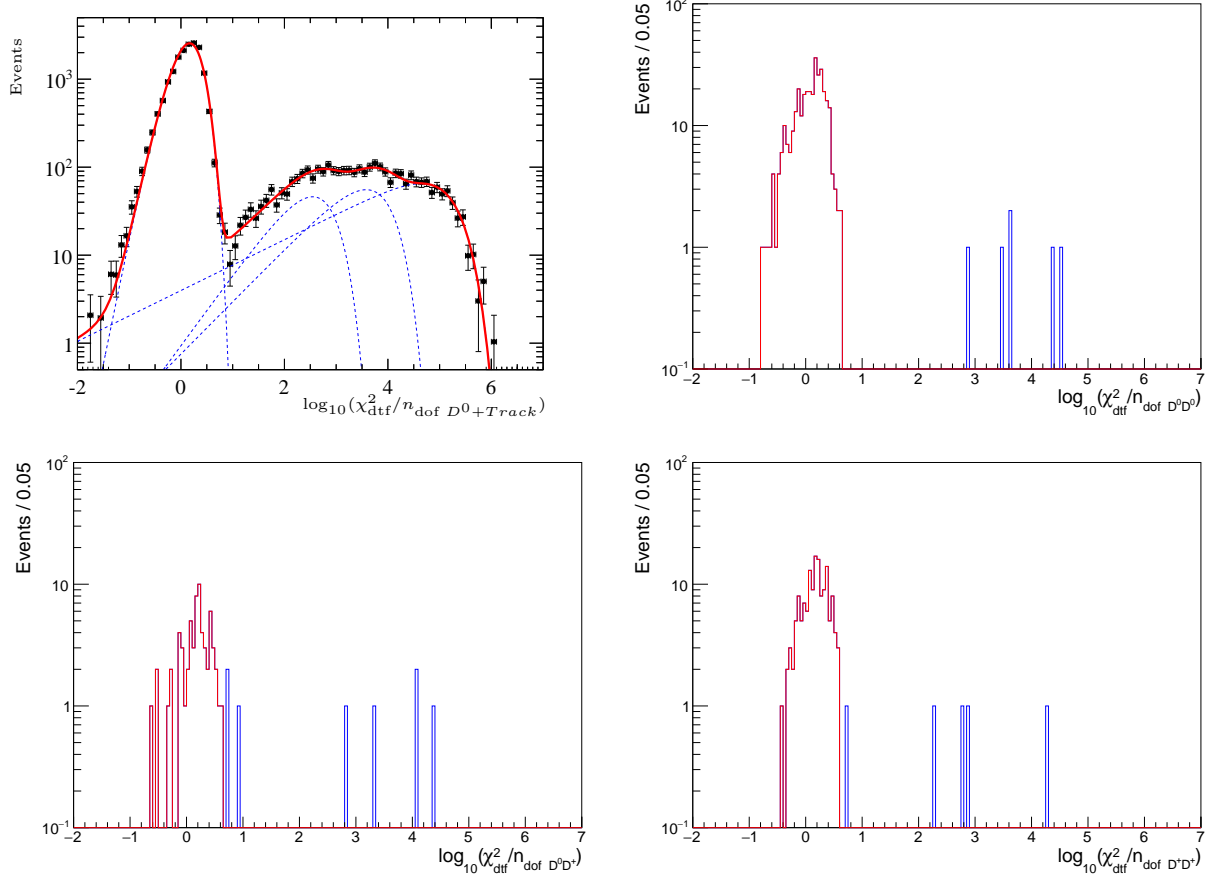
Figure 4.1: $\chi^2_{\mathrm{dtf}}/n_{\mathrm{dof}}$ distribution for different candidates (from top left to bottom right):
1) $D^0 + Track$ candidates, fitted by a model consisting of four Gamma distributions, one each for the signal, the two feed-down and the pile-up peaks (from left to right) [34], [35]. The two feed-down peaks originate from the decays of B mesons with different topologies.
2) $D^0 D^0$
3) $D^0 D^+$
4) $D^0 D^+$
The distributions in b), c), d) are displayed for the Stripping21 selection (blue) and for the additional cut $\chi^2_{\mathrm{dtf}}/n_{\mathrm{dof}\ CC} < 5$ (red).

4.3 Selected Candidates

This chapter illustrates the selected single open charm event candidates D^0 and D^+ modes $D^0 \to K^-\pi^+$, $D^+ \to K^-\pi^+\pi^+$ and the selected double open charm event candidates D^0D^0, D^0D^+ and D^+D^+ with corresponding decay modes $D^0D^0 \to 2 \cdot D^0 \to 2 \cdot (K^-\pi^+)$, $D^0D^+ \to D^0 + D^+ \to (K^-\pi^+) + (K^-\pi^+\pi^+)$, $D^+D^+ \to 2 \cdot D^+ \to 2 \cdot (K^-\pi^+\pi^+)$.

The total number of events N_{tot} is extracted from the invariant mass distributions of the single and double open charm event candidates, M_C, M_{CC}, where $C \in \{D^0, D^+\}$, with fully applied event selection (see ch. 4.2.1). They are shown in Tab. 4.5, whereas the corresponding invariant mass distributions are shown in Fig. 4.2 for D^0 and D^+, in Fig. 4.3 for D^0D^0, D^0D^+ and D^+D^+ and in Fig. 4.4 for $D^0\bar{D}^0$ and D^+D^-. Surprisingly no D^0D^- events were observed. So for this combination only the double open charm channel but not the pair production channel is seen. This is considered a statistical fluctuation. Since N_{tot} for all double open charm event candidates is small, there is no need to consider even rarer candidates like D^{*0}, D^{*+}, D_s^0, D_s^+.

Candidate	N_{tot}, standard selection	N_{tot}, ($p^T > 4$ GeV, $y > 2.25$) selection
D^0	96441	82087
D^+	59708	54138
D^0D^0	8	5
D^0D^+	11	4
D^+D^+	3	1
$D^0\bar{D}^0$	79	21
D^0D^-	0	0
D^+D^-	48	25

Table 4.5: The total number of events for the single open charm, double open charm and open charm pair production event candidates. The standard selection is the selection applied in chapter 4.2.1, the ($p^T > 4$ GeV, $y > 2.25$) selection is the one according to chapter C (see also chapter 4.6).
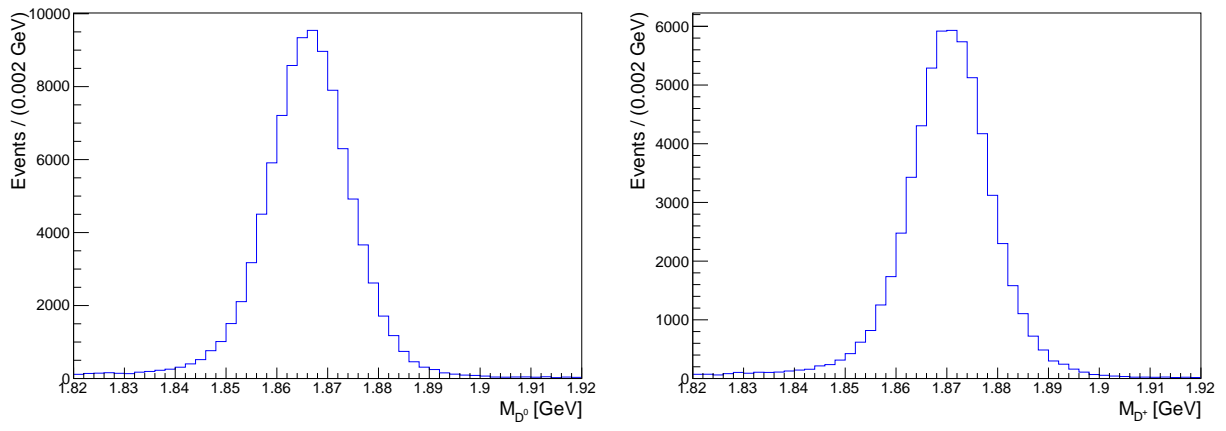
Figure 4.2: Invariant mass distributions of the single open charm event candidates D^0 (left) and D^+ (right).
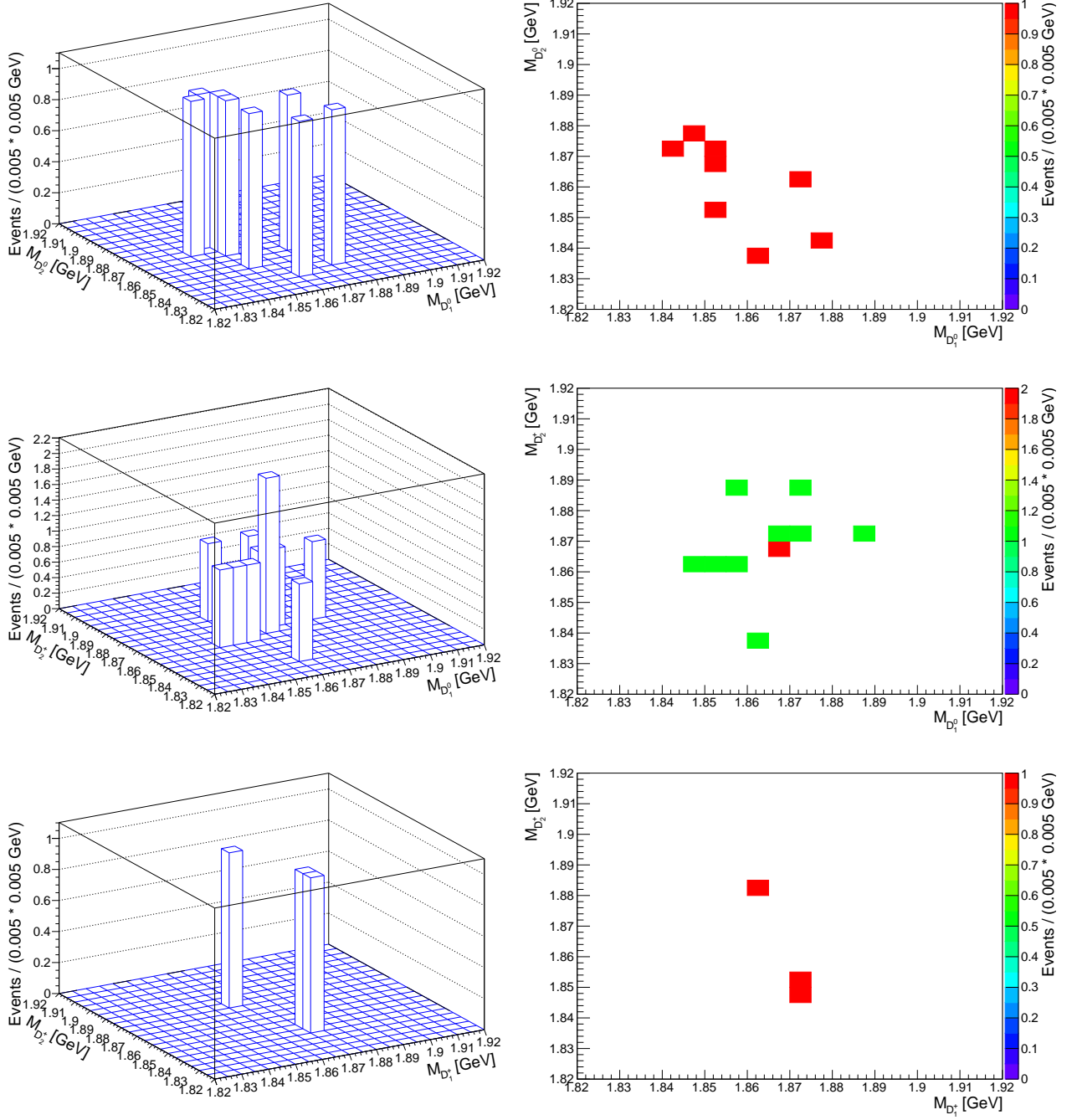
Figure 4.3: Invariant mass distributions for the double open charm event candidates $D^0 D^0$ (1st row), $D^0 D^+$ (2nd row) and $D^+ D^+$ (3rd row).
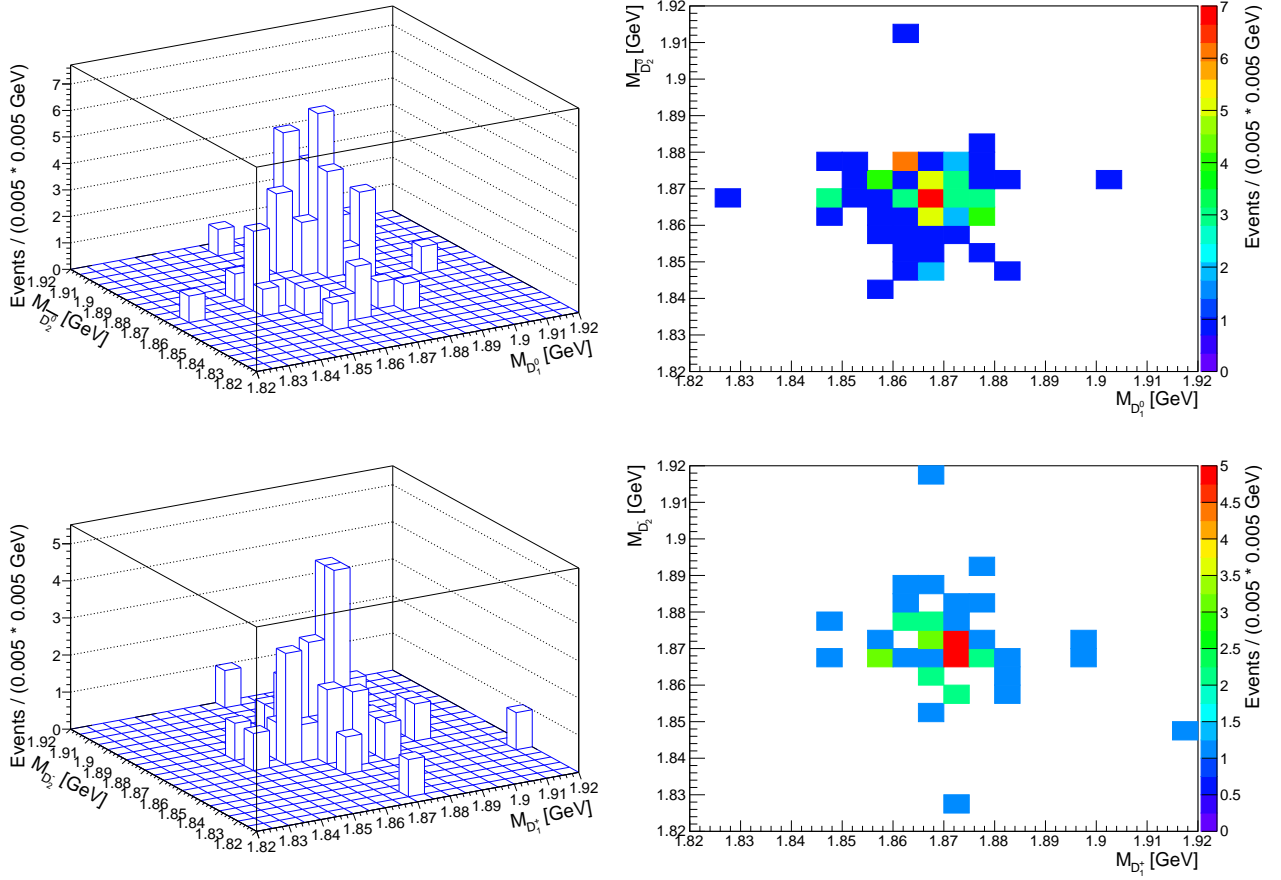
Figure 4.4: Invariant mass distributions for the charm pair production event candidates $D^0\bar{D}^0$ (1st row) and D^+D^- (2nd row). No event candidates are observed for the case D^0D^-.

4.4 Invariant Mass Fits

The number of signal events is extracted by unbinned maximum likelihood fits to the invariant mass distributions of the single and double open charm event candidates, M_C and M_{CC}, where $C \in \{D^0, D^+\}$ using the RooFit v3.60 package within the ROOT framework v6.06.02 [36]. The fits give an estimate of the normalization parameter for the signal, which is the number of signal events. The quality of this estimate depends on the chosen fit model. Three models are tested to find the one, which gives the best estimate. The simplest option for a model is given by a Gaussian probability density function (PDF), the second by a Bukin PDF and the third by a Double Crystal Ball PDF. Each model consists of a signal component $S(M)$, given by the three options, and a background component $B(M)$, given by an Exponential PDF. In order to evaluate the quality of the fits, three goodness of fit criteria are imposed. The first is the reduced χ^2, χ^2/n_{dof}, the second the upper tail probability or upper p-value of the corresponding χ^2 distribution, $P_u(\chi^2, n_{\text{dof}})$ and the third the distribution of the pull values p_i (see ch. 3.1.2). In contrast to the Gaussian PDF, the Bukin and Double Crystal Ball PDF can describe initial and final state radiation. The Gaussian model is used to gauge the pull distributions for a wrong model. Since the layout for the construction of the fit models for M_C is different than for M_{CC}, the invariant mass fits for the two open charm event cases are separated, providing a better overview.

Single Open Charm Event Candidates

The invariant mass distributions for the single open charm event candidates D^0, D^+, M_{D^0}, M_{D^+}, are one dimensional. Therefore the fit model F with its components $S(M)$, $B(M)$ is also one dimensional. The functional form of the fit model is:

$$F(S(M), B(M)) \;=\; N_S \cdot S(M) + N_B \cdot B(M) \quad ,$$

where M : invariant mass of the single open charm
            event candidates D^0, D^+

$\qquad\qquad$ $S(M)$, N_S : signal component with its normalization parameter $\qquad$ (4.6)
$\qquad\qquad\qquad\qquad$ (number of signal events)

$\qquad\qquad$ $B(M)$, N_B : background component with its normalization parameter
$\qquad\qquad\qquad\qquad$ (number of background events)   .

The functional form of the signal component $S(M)$ is given according to the three options:

1) Gaussian PDF:

$$S(M) \;=\; Gauss(M; \mu, \sigma)$$

$$=\; \exp\left(-\frac{(M-\mu)^2}{2\,\sigma^2}\right) \quad,$$

where $\quad\mu$: peak position, i.e. expectation value of the PDF

σ : peak width, i.e. standard deviation defined by $\sigma = \dfrac{\text{FWHM}}{2\,\sqrt{2\ln(2)}}$.

$$\text{(4.7)}$$

2) Bukin PDF:

$$S(M) \;=\; Bukin(M; \mu, \sigma, \xi, \rho_l, \rho_r)$$

$$=\;
\begin{cases}
\frac{1}{2}\exp\left(\frac{\sqrt{2\ln(2)}\;\xi\;\sqrt{\xi^2+1}\;(M-m_1)}{\sigma\left(\sqrt{\xi^2+1}-\xi\right)^2\ln\left(\sqrt{\xi^2+1}+\xi\right)} + \rho_l\left(\frac{M-m_1}{\mu-m_1}\right)^2\right) & ,\; M < m_1 \\[3em]
\exp\left(-\ln(2)\;\left(\frac{\ln\left(1 + 2\xi\sqrt{\xi^2+1}\;\frac{M-\mu}{\sigma\;\sqrt{2\ln 2}}\right)}{\ln\left(1+2\xi^2-2\xi\sqrt{\xi^2+1}\right)}\right)^2\right) & ,\; m_1 < M < m_2 \\[3em]
\frac{1}{2}\exp\left(\frac{\sqrt{2\ln(2)}\;\xi\;\sqrt{\xi^2+1}\;(M-m_2)}{\sigma\left(\sqrt{\xi^2+1}-\xi\right)^2\ln\left(\sqrt{\xi^2+1}+\xi\right)} + \rho_r\left(\frac{M-m_2}{\mu-m_2}\right)^2\right) & ,\; M > m_2
\end{cases} \quad,$$

where $\quad\mu$: peak position, i.e. expectation value of the PDF

σ : peak width, i.e. standard deviation defined by $\sigma = \dfrac{\text{FWHM}}{2\,\sqrt{2\ln(2)}}$

ξ : asymmetry parameter

ρ_l, ρ_r : left and right tail parameters

$$m_{1,2} \;=\; \mu \;+\; \sigma\;\sqrt{2\ln(2)}\;\left(\frac{\xi}{\sqrt{\xi^2+1}} \mp 1\right) \quad.$$

$$\text{(4.8)}$$

3) Double Crystal Ball PDF:

$$
\begin{aligned}
S(M) \;=\;& DCB(M; \mu, \sigma, \alpha_l, \alpha_r, n_l, n_r) \\[6pt]
=\;& r
\begin{cases}
\left(\frac{n_l}{|\alpha_l|}\right)^{n_l} \exp\left(-\frac{|\alpha_l|^2}{2}\right) \left(\frac{n_l}{|\alpha_l|} - |\alpha_l| - \frac{M-\mu}{\sigma}\right)^{-n_l} & , \quad \frac{M-\mu}{\sigma} < -|\alpha_l| \\[10pt]
\exp\left(-\frac{(M-\mu)^2}{2\,\sigma^2}\right) & , \quad \frac{M-\mu}{\sigma} >= -|\alpha_l|
\end{cases} \\[14pt]
+\;& (1-r)
\begin{cases}
\left(\frac{n_r}{|\alpha_r|}\right)^{n_r} \exp\left(-\frac{|\alpha_r|^2}{2}\right) \left(\frac{n_r}{|\alpha_r|} - |\alpha_r| + \frac{M-\mu}{\sigma}\right)^{-n_r} & , \quad \frac{M-\mu}{\sigma} < -|\alpha_r| \\[10pt]
\exp\left(+\frac{(M-\mu)^2}{2\,\sigma^2}\right) & , \quad \frac{M-\mu}{\sigma} >= -|\alpha_r|
\end{cases} \; ,
\end{aligned}
$$

where μ : peak position, i.e. expectation value of the PDF

σ : peak width, i.e. standard deviation defined by $\sigma = \dfrac{\text{FWHM}}{2\,\sqrt{2\ln 2}}$

$\alpha_l > 0, \alpha_r < 0$: turning points of the left and right tail

n_l, n_r : left and right tail parameters

$0 \leq r \leq 1$: normalization parameter   .

$$\tag{4.9}$$

The functional form of the background component B(M) is given by an Exponential PDF:

$$
B(M) \;=\; \exp\left(\tau\, M\right) \quad ,
$$

where τ : slope parameter of the PDF   .

$$\tag{4.10}$$

The Gaussian model has 5 free parameters for the overall shaping and behaves robustly with respect to the starting values for the fit. The Bukin model has 8 free parameters for the overall shaping and has poorer robustness compared to the Gaussian model. The tail and background parameters behave unstable, such that a simultaneous fit of the signal and background components is difficult. Instead, the background component $B(M)$ of the Bukin model was fitted first in the ranges $[1.82, 1.83]$ GeV and $[1.91, 1.92]$ GeV, where the background fraction in the events is the highest. Then, the free parameters of $B(M)$, i.e. the slope τ and N_B, are fixed before the fit using the complete Bukin model in the complete range of $[1.82, 1.92]$ GeV is executed. The Double Crystal Ball model has 10 free parameters for the overall shaping and has an even inferior robustness compared to the Bukin model. Despite the usage of the same fit procedure as for the Bukin model, the handling of the unstable tail and background parameters remains difficult.

The results of the fits to the invariant mass distributions M_{D^0}, M_{D^+} are shown in Fig. 4.5 and Fig. 4.6 respectively. The corresponding results for the fit parameters are listed in Tab. A.1, A.2, A.3. The best fit model describing M_{D^0}, M_{D^+} is found by a comparison of the three goodness of fit criteria for the models. A good model has a χ^2-value and an upper P-value close to 1 and a preferably flat pull distribution. Therefore, the model, which describes both M_{D^0} and M_{D^+} distributions the best, is the Double Crystal Ball,

closely followed by the Bukin model. The fit quality of the Gaussian model is inferior to the Bukin and Double Crystal Ball models, also clearly visible by eye. This is expected, since the Gaussian model neglects the tails of the invariant mass distributions, which are known to be present in LHCb data. Since the Double Crystal Ball model has two more free parameters than the Bukin model, it is in principle expected to describe the invariant mass distribution better. The direct comparison of the pull distributions of the Bukin and Double Crystal Ball models in Fig. 4.7 reveals, that the Bukin model has more difficulties to describe the lower tail of the invariant mass distributions than the Double Crystal Ball model, whereas both models describe the upper tail nearly equivalently good. The small difference in the fit quality of these two models can therefore be caused by the difference in the amount of free parameters. The disagreement to the previous analysis can also be caused by the smaller available center of mass energy $\sqrt{s}$ and total number of events of the invariant mass distributions. It is concluded, that the Double Crystal Ball model does not describe the invariant mass distributions significantly better than the Bukin model. Not enough justification is found in order abandon the commonly used Bukin model in preference of the Double Crystal Ball model, i.e. the difference in the fit quality of the two models is so small, that it is considered irrelevant in the further analysis. Therefore, the Bukin model is chosen to describe the invariant mass of the single open charm event candidates.

Figure 4.5: Results of the unbinned maximum likelihood fits to the invariant mass distribution for the single open charm event candidate D^0, M_{D^0}. Three options for the fit model are tested. The first row shows the results for the Gaussian model, the second row the results for the Bukin model, the third row the results for the Double Crystal Ball model. In the right column the pull distributions for the corresponding model are shown.
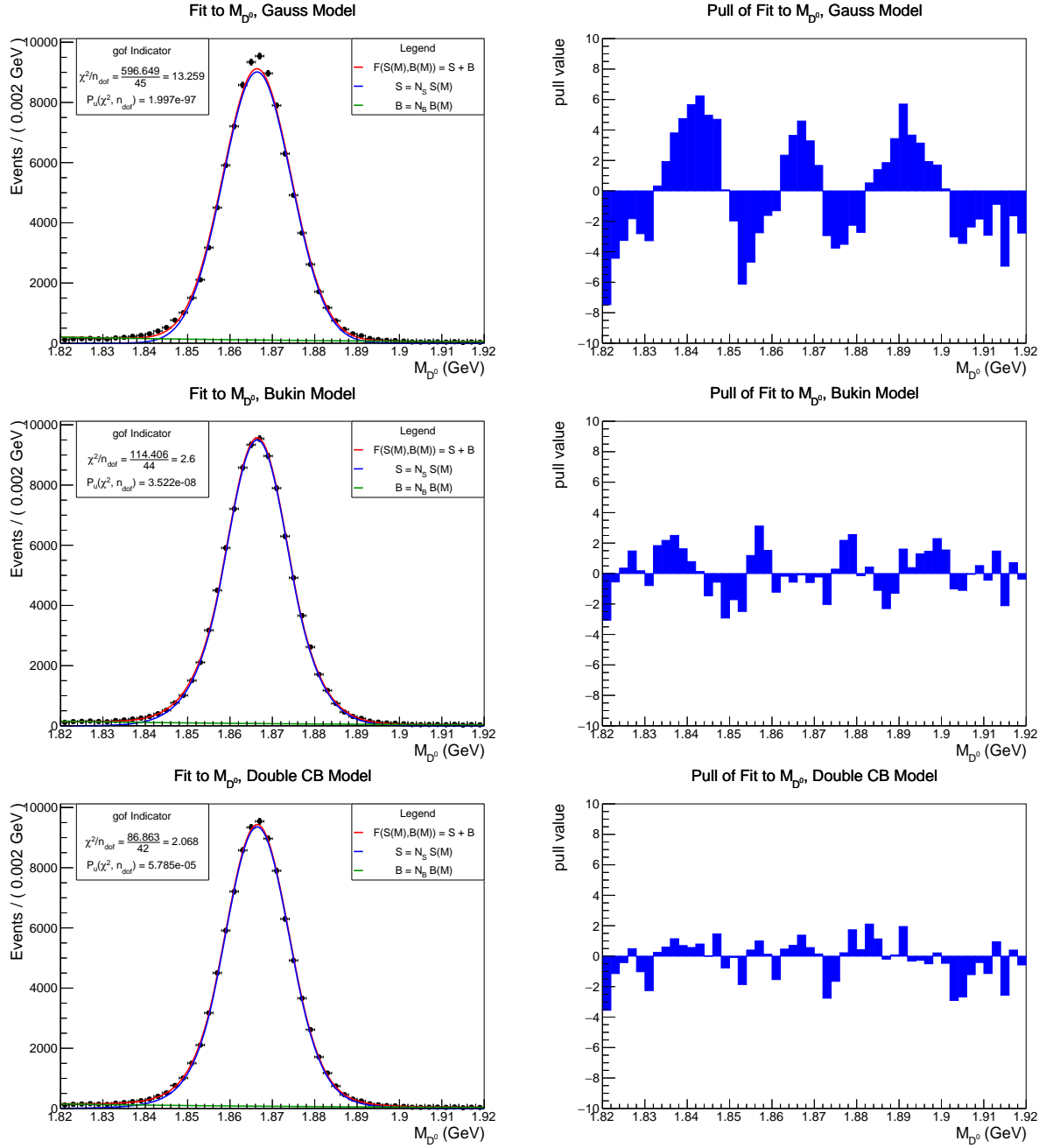
Figure 4.6: Results of the unbinned maximum likelihood fits to the invariant mass distribution for the single open charm event candidate D^+, M_{D^+}. Three options for the fit model are tested. The first row shows the results for the Gaussian model, the second row the results for the Bukin model, the third row the results for the Double Crystal Ball model. In the right column the pull distributions for the corresponding model are shown.
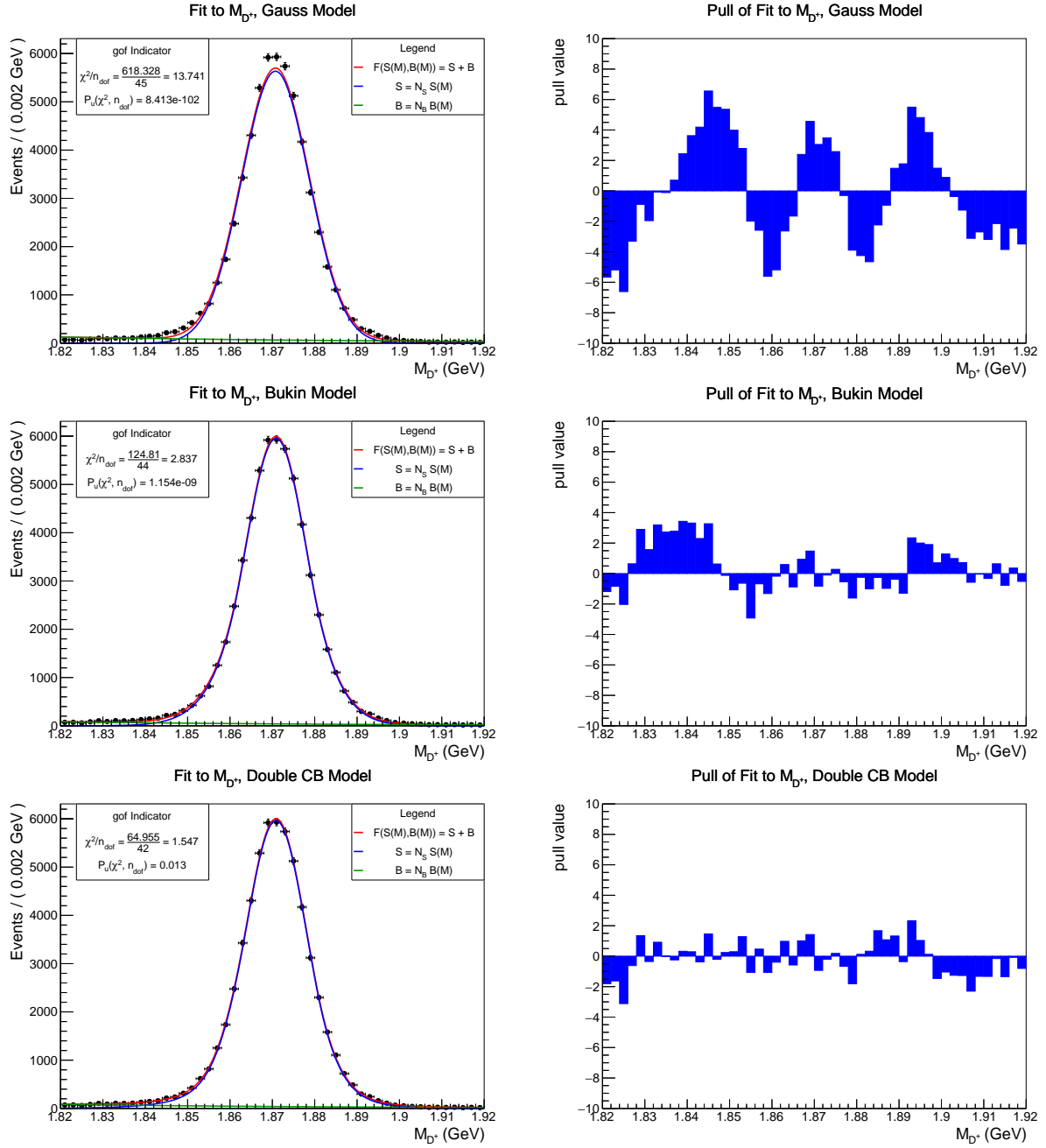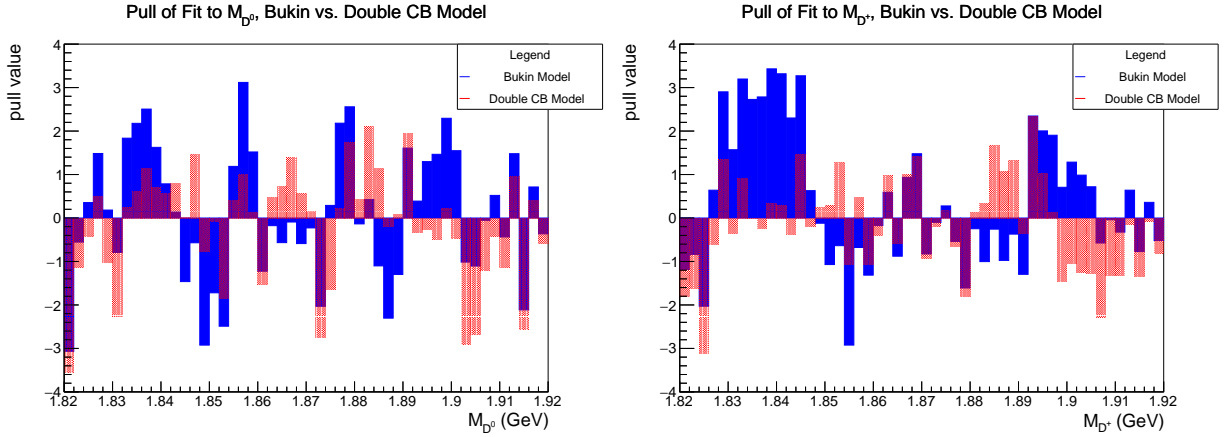
Figure 4.7: The pull distributions of the maximum likelihood fits to the invariant mass distributions M_{D^0} (left) and M_{D^+} (right) for the Bukin model (blue) and the Double Crystal Ball model (red) in direct comparison.

Double Open Charm resp. Open Charm Pair Production Event Candidates

Due to the low total number of events in the double charm meson cases D^0D^0, D^0D^+, D^+D^+, the fit model for the two dimensional mass distributions is constructed based on the ones used for the single charm meson cases. All shape related fit parameters for the signal were determined on the single open charm sample and then fixed and used for the double open charm sample, whereas the fit parameters for the background shape are left free. In order to increase the total number of events of the mass distributions M_{CC}, the double open charm production and pair production samples are temporarily merged, i.e. $D^0D^0 := \{D^0D^0 \cup D^0\bar{D}^0\}$, $D^0D^+ := \{D^0D^+ \cup D^0D^-\}$ and $D^+D^+ := \{D^+D^+ \cup D^+D^-\}$. These samples are separated from each other in chapter 4.5. For the D^0D^0 and D^+D^+ cases, the D^0, D^+ candidates are assigned randomly to be first or second. The notation $M_{C_1C_2}$ originates only from the definition, that M_{C_1} is related to the x-axis and M_{C_2} is related to the y-axis of the two dimensional invariant mass distributions. The functional form of the fit model is:

$$F(S_1(M_{C_1}), S_2(M_{C_2}), B_1(M_{C_1}), B_2(M_{C_2}))$$

$$= N_{S_1 S_2} \, S_1(M_{C_1}) \, S_2(M_{C_2}) \; + \; N_{B_1 B_2} \, B_1(M_{C_1}) \, B_2(M_{C_2})$$
$$+ \; N_{S_1 B_2} \, S_1(M_{C_1}) \, B_2(M_{C_2}) \; + \; N_{S_2 B_1} \, S_2(M_{C_2}) \, B_1(M_{C_1}) \quad ,$$

where $\quad M_{C_l}$, $C_l \in \{D^0, D^+\}$, $l \in \{1, 2\}$:

invariant mass of the single open charm components to the corresponding double open charm event candidates (including open charm pair production) $\{D^0 D^0 \cup D^0 \bar{D}^0\}$, $\{D^0 D^+ \cup D^0 D^-\}$ and $\{D^+ D^+ \cup D^+ D^-\}$

S_l, $l \in \{1, 2\}$: signal component of the single charm components to the corresponding double open charm event candidates (including open charm pair production)

B_l, $l \in \{1, 2\}$: background component of the single open charm components to the corresponding double open charm event candidates (including open charm pair production)

$N_{S_1 S_2}, N_{S_1 B_2}, N_{S_2 B_1}, N_{B_1 B_2}$:
normalization parameters for the four components of the fit model   .

(4.11)

The functional form of $S_l(M_{C_l})$, $B_l(M_{C_l})$, where $C_l \in \{D^0, D^+\}$, $l \in \{1, 2\}$ is described in equation 4.6.

According to this functional form, the fit model for the double open charm event candidates consists of the following components illustrated in Fig. 4.8:

1) Signal (Fig. 4.8 top left): It is modeled by a product PDF of the individual signal components for the first and second single open charm event candidate, denoted by $S_1(M_{C_1})$, $S_2(M_{C_2})$. In the fit, the signal has the normalization $N_{S_1 S_2}$, being the only free parameter.

2) Pure combinatorial background (Fig. 4.8 top right): It is modeled by a product PDF of the individual background components for the first and second single open charm event candidate, denoted by $B_1(M_{C_1})$, $B_2(M_{C_2})$. In the fit, this background has the normalization $N_{B_1 B_2}$ and the exponential slope parameters $\tau_{B_1, c}$, $\tau_{B_2, c}$ as free parameters. $\tau_{B_1, c}$, $\tau_{B_2, c}$ are constrained to be the same for $D^0 D^0$, $D^+ D^+$.

3) The signal for the first single open charm event candidate together with the combinatorial background for the second one (Fig. 4.8 bottom left). It is modeled by a product PDF of the signal- and background components for the first and second single open charm event candidate, denoted by $S_1(M_{C_1})$ and $B_2(M_{C_2})$. In the fit, this background has the normalization $N_{S_1 B_2}$ and the exponential slope parameter τ_{B_2} as free parameters.

4) The signal for the second single open charm event candidate together with the combinatorial background for the first one (Fig. 4.8 bottom right). It is modeled by a product PDF of the signal- and background components for the second and first single open charm event candidates, denoted by $S_2(M_{C_2})$ and $B_1(M_{C_1})$. In the fit, this background has the normalization $N_{S_2 B_1}$ and the exponential slope parameter τ_{B_1} as free parameters.

In analogy to the fit model for the single open charm event cases, the signal components $S_1(M_{C_1})$, $S_2(M_{C_2})$ are described by three models, the Gaussian, Bukin and Double Crystal Ball PDF's, whereas the backround components $B_1(M_{C_1})$, $B_2(M_{C_2})$ are described by an Exponential PDF (see equation 4.6, ff.). All shape parameters, except from the ones related to $B_1(M_{C_1})$, $B_2(M_{C_2})$, i.e. the τ and N parameters, are determined from the single charm sample and then fixed.

The results of the fits to the invariant mass distributions $M_{D^0 D^0}$, $M_{D^0 D^+}$, $M_{D^+ D^+}$ (including open charm pair production), are shown as projections of $M_{D_1^0}$, $M_{D_2^0}$, $M_{D_1^+}$, $M_{D_2^+}$ in Fig. 4.9, Fig. 4.10, Fig. 4.11, Fig. 4.12, Fig. 4.13, Fig. 4.14. The correponding results for the fit parameters are listed in Tab. A.4, A.5, A.6. Unlike the fit for the single open charm event candidates, the comparison of the three goodness of fit criteria results in the conclusion, that all three models describe the distributions $M_{D^0 D^0}$, $M_{D^0 D^+}$, $M_{D^+ D^+}$ with almost the same quality. Especially, the fit qualities for the Double Crystal Ball model and the Bukin model are almost indistinguishably close together (see Fig. 4.15). Therefore all models can be used to describe the invariant mass distributions of the double open charm event candidates (including open charm pair production). Consequently the Bukin and the

Double Crystal Ball models yield almost identical numbers of signal events $N_{S_1 S_2}$, while the Gaussian model yields consistantly smaller but compatible values. This behaviour is expected, since $M_{D^0 D^0}$, $M_{D^0 D^+}$, $M_{D^+ D^+}$ have a small number of events compared to M_{D^0}, M_{D^+}. For consistency with the single open charm event cases, the Bukin model is used to describe the invariant mass distributions $M_{D^0 D^0}$, $M_{D^0 D^+}$, $M_{D^+ D^+}$. The results for $N_{S_1 S_2}$ clearly suggest a signal for $D^0 D^0 \cup D^0 \bar{D}^0$ and $D^+ D^+ \cup D^+ D^-$ (see Tab. 4.6).

Candidate	$N_{S_1 S_2}$	$N_{B_1 B_2}$	$N_{S_1 B_2}$	$N_{S_2 B_1}$
$D^0 D^0 \cup D^0 \bar{D}^0$	78.1 ± 7.4	$2.7 \cdot 10^{-6}$	4.0 ± 2.5	4.9 ± 2.7
$D^0 D^+ \cup D^0 D^-$	9.4 ± 3.7	$1.3 \cdot 10^{-6} \pm 190.2$	1.2 ± 1.2	0.4 ± 3.4
$D^+ D^+ \cup D^+ D^-$	44.3 ± 7.8	1.4 ± 1.9	4.3 ± 3.1	0.9 ± 5.0

Table 4.6: Normalization parameters of the unbinned maximum likelihood fits to the invariant mass of the double open charm event candidates (including open charm pair production), taken from Tab. A.5 for the Bukin model.
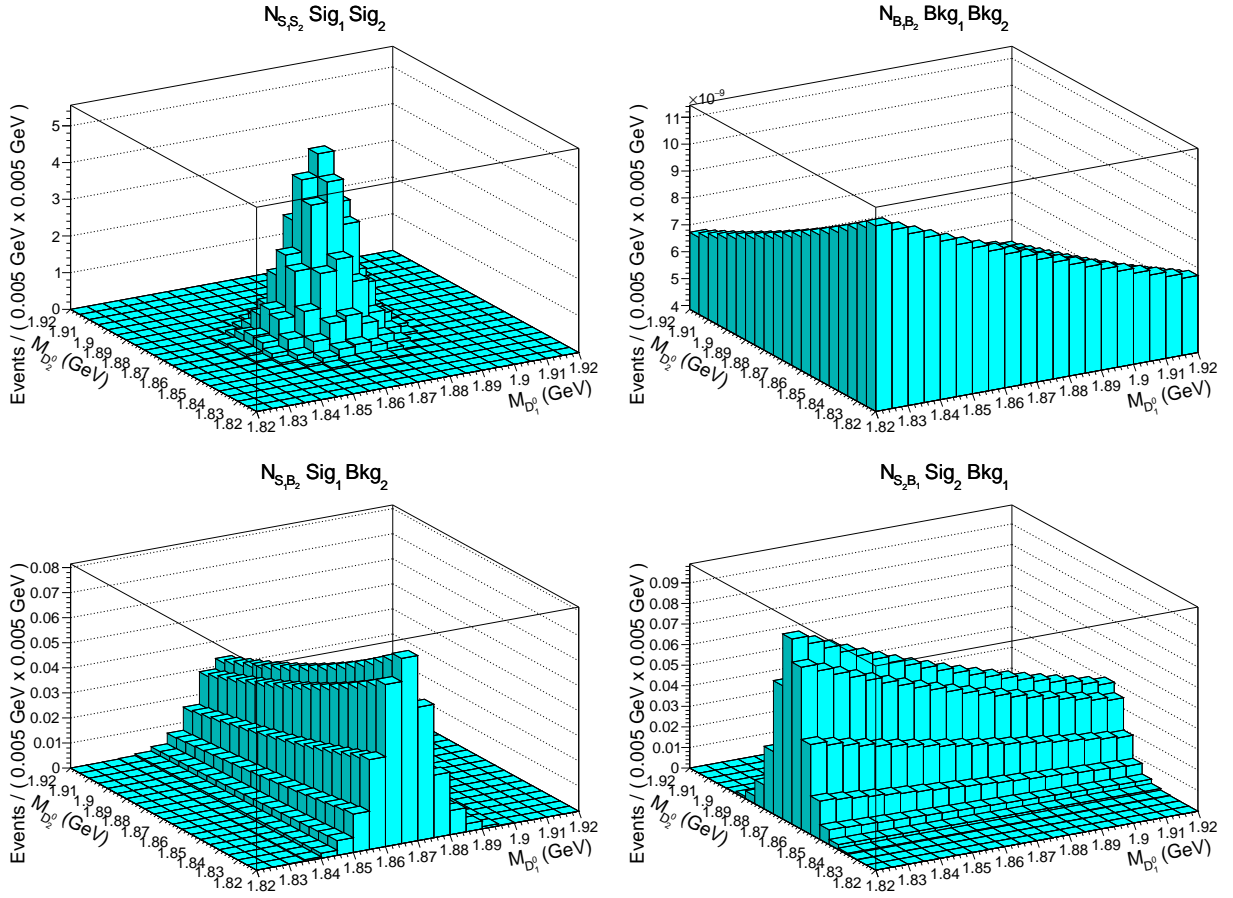
Figure 4.8: Graphical illustration of the functional form of the fit model for the double open charm event candidates $D^0 D^0$ (including open charm pair production). The four images show the four components of the fit model: $N_{S_1 S_2}\ Sig_1\ Sig_2$ (top left), $N_{B_1 B_2}\ Bkg_1\ Bkg_2$ (top right), $N_{S_1 B_2}\ Sig_1\ Bkg_2$ (bottom left) and $N_{S_2 B_1}\ Sig_2\ Bkg_1$ (bottom right).

Figure 4.9: Results of the unbinned extended maximum likelihood fits to the invariant mass distribution for the double open charm event candidate D^0D^0 (including open charm pair production), $M_{D^0D^0}$, as $M_{D_1^0}$ projection. Three options for the fit model are tested. The first row shows the results for the Gaussian model, the second row the results for the Bukin model, the third row the results for the Double Crystal Ball model. In the right column the pull distributions for the corresponding model are shown.

Figure 4.10: Results of the unbinned extended maximum likelihood fits to the invariant mass distribution for the double open charm event candidate D^0D^0, $M_{D^0D^0}$ (including open charm pair production), as $M_{D_2^0}$ projection. Three options for the fit model are tested. The first row shows the results for the Gaussian model, the second row the results for the Bukin model, the third row the results for the Double Crystal Ball model. In the right column the pull distributions for the corresponding model are shown.
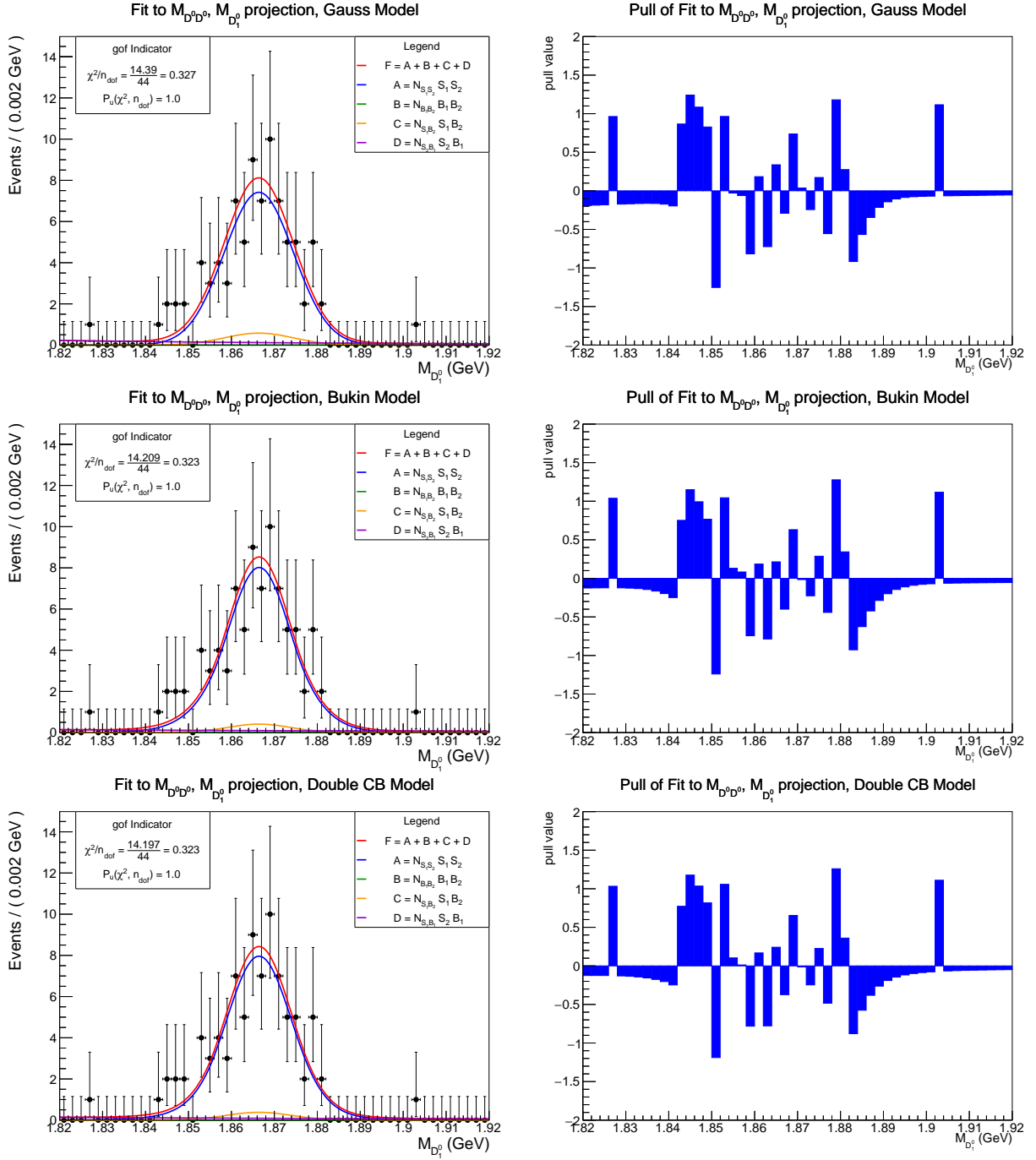
Figure 4.11: Results of the unbinned extended maximum likelihood fits to the invariant mass distribution for the double open charm event candidate D^0D^+ (including open charm pair production), $M_{D^0D^+}$, as $M_{D_1^0}$ projection. Three options for the fit model are tested. The first row shows the results for the Gaussian model, the second row the results for the Bukin model, the third row the results for the Double Crystal Ball model. In the right column the pull distributions for the corresponding model are shown.

Figure 4.12: Results of the unbinned extended maximum likelihood fits to the invariant mass distribution for the double open charm event candidate D^0D^+ (including open charm pair production), $M_{D^0D^+}$, as $M_{D_2^+}$ projection. Three options for the fit model are tested. The first row shows the results for the Gaussian model, the second row the results for the Bukin model, the third row the results for the Double Crystal Ball model. In the right column the pull distributions for the corresponding model are shown.
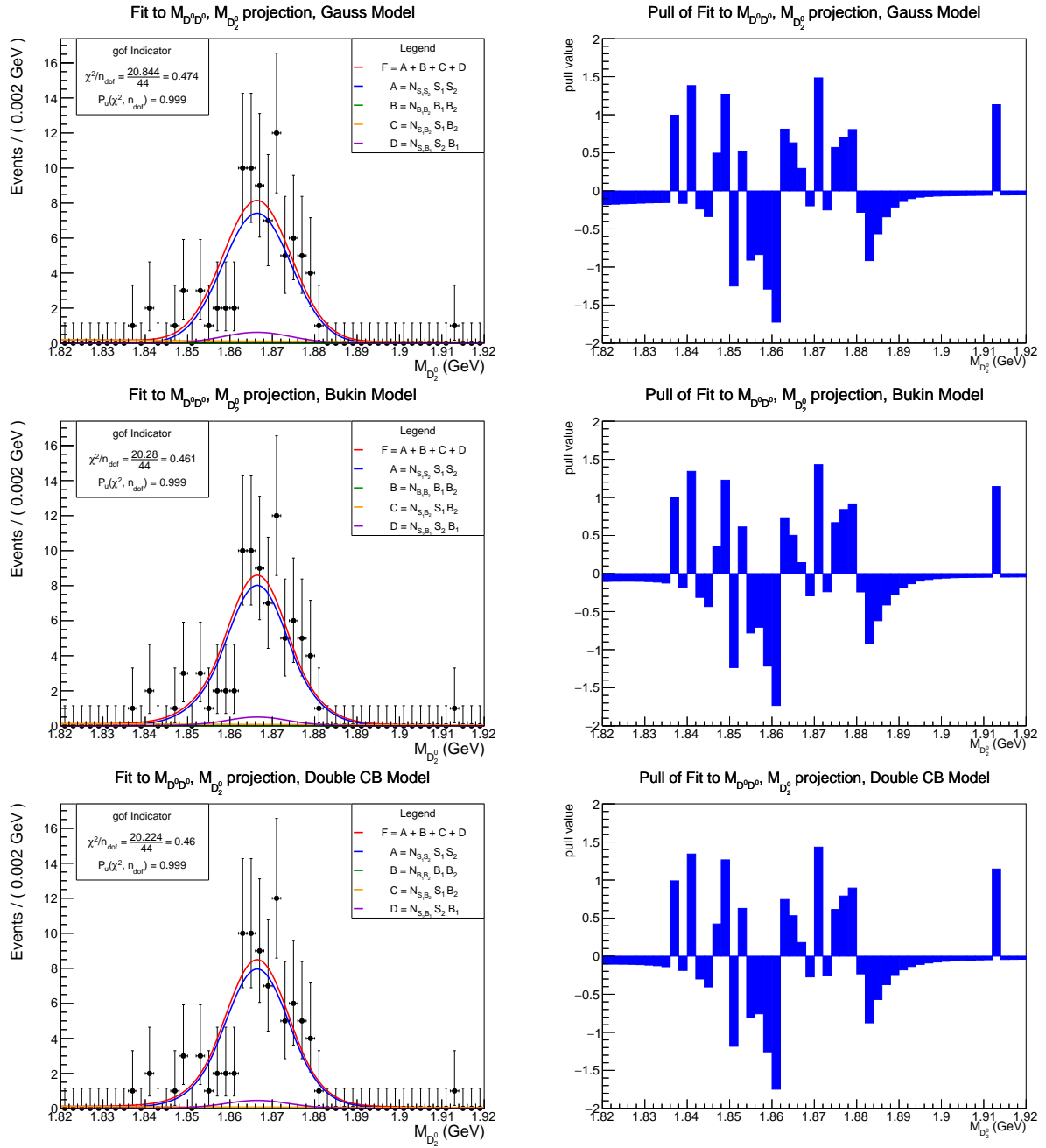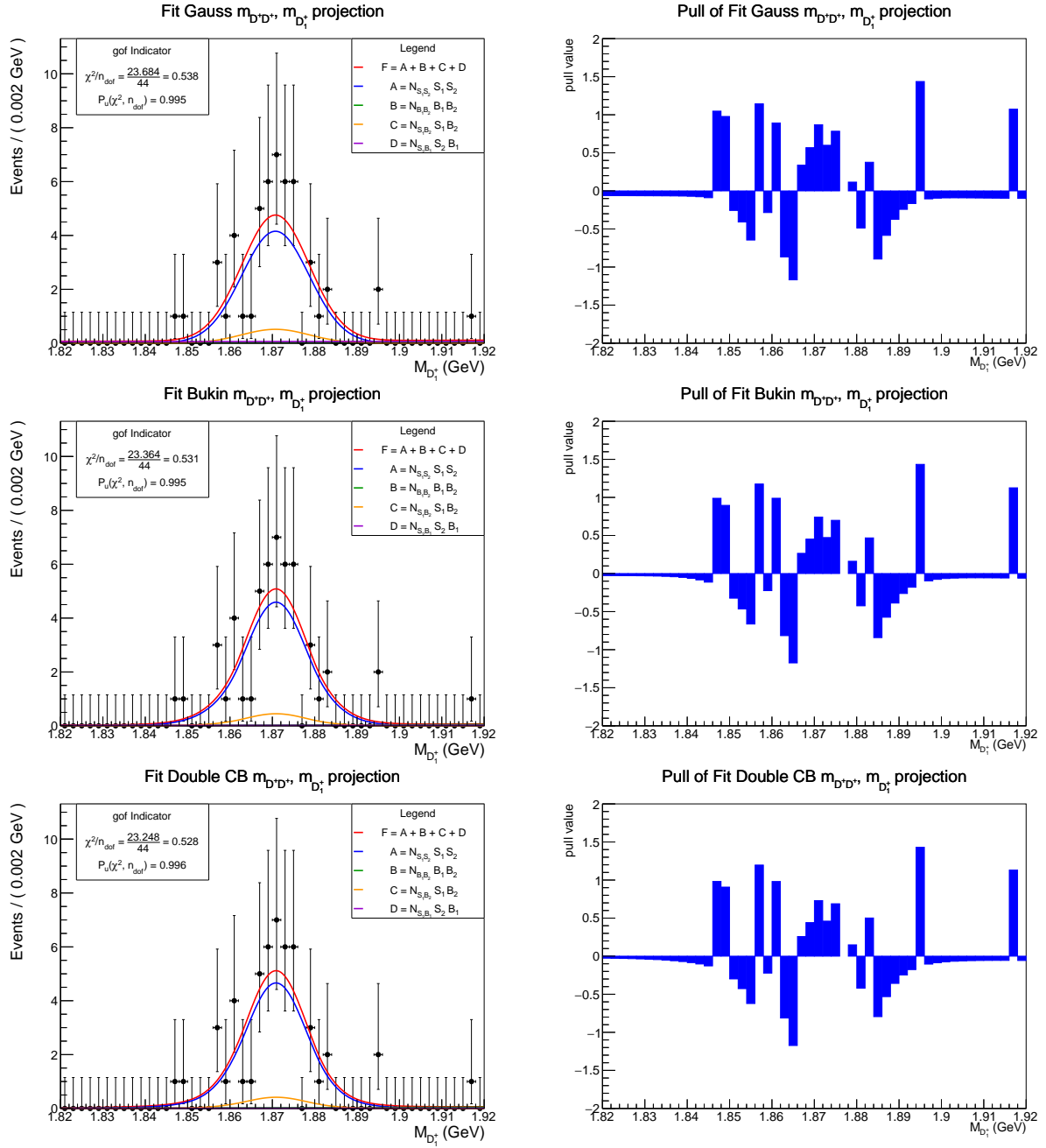
Figure 4.13: Results of the unbinned extended maximum likelihood fits to the invariant mass distribution for the double open charm event candidate D^+D^+ (including open charm pair production), $M_{D^+D^+}$, as $M_{D_1^+}$ projection. Three options for the fit model are tested. The first row shows the results for the Gaussian model, the second row the results for the Bukin model, the third row the results for the Double Crystal Ball model. In the right column the pull distributions for the corresponding model are shown.
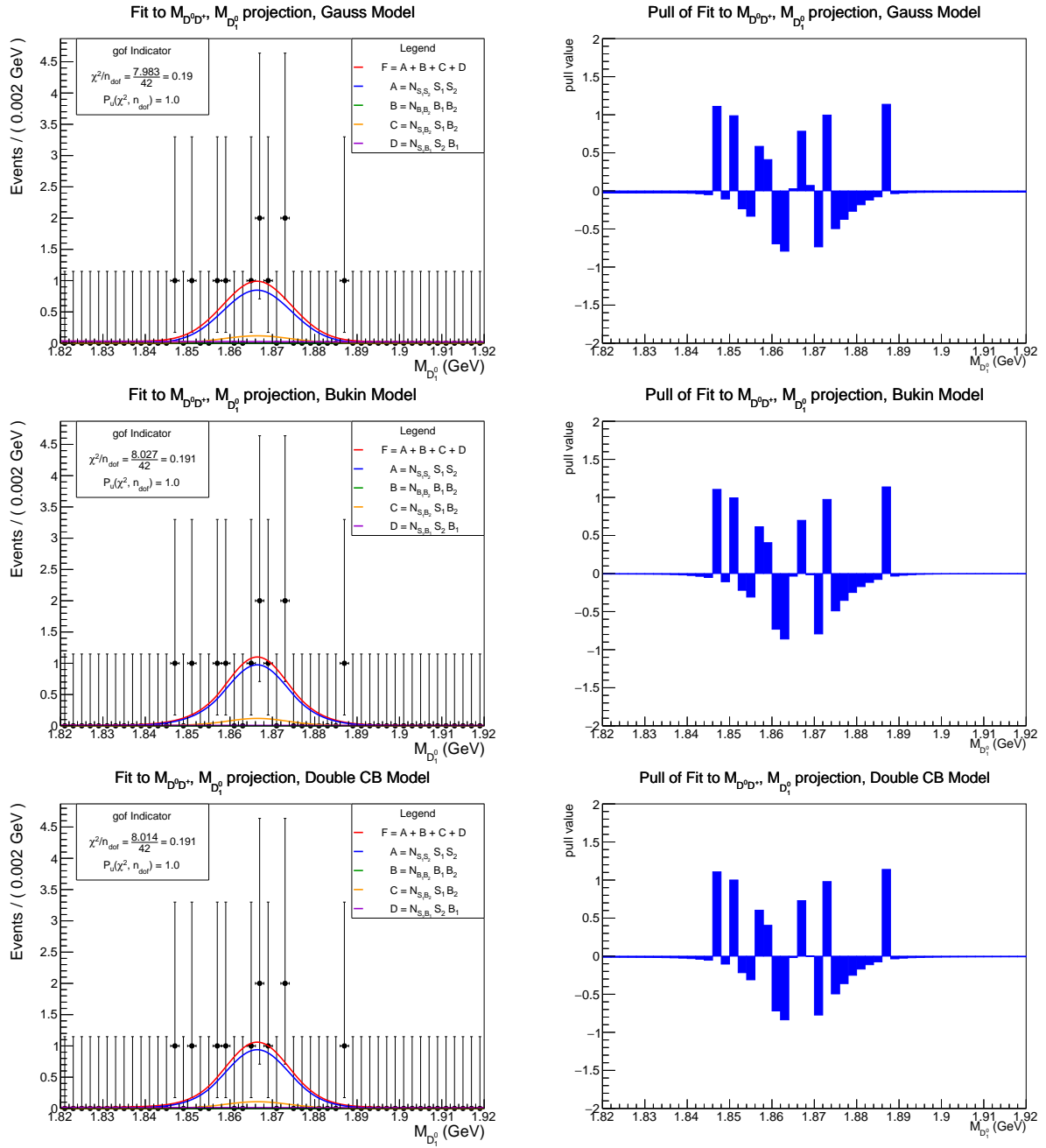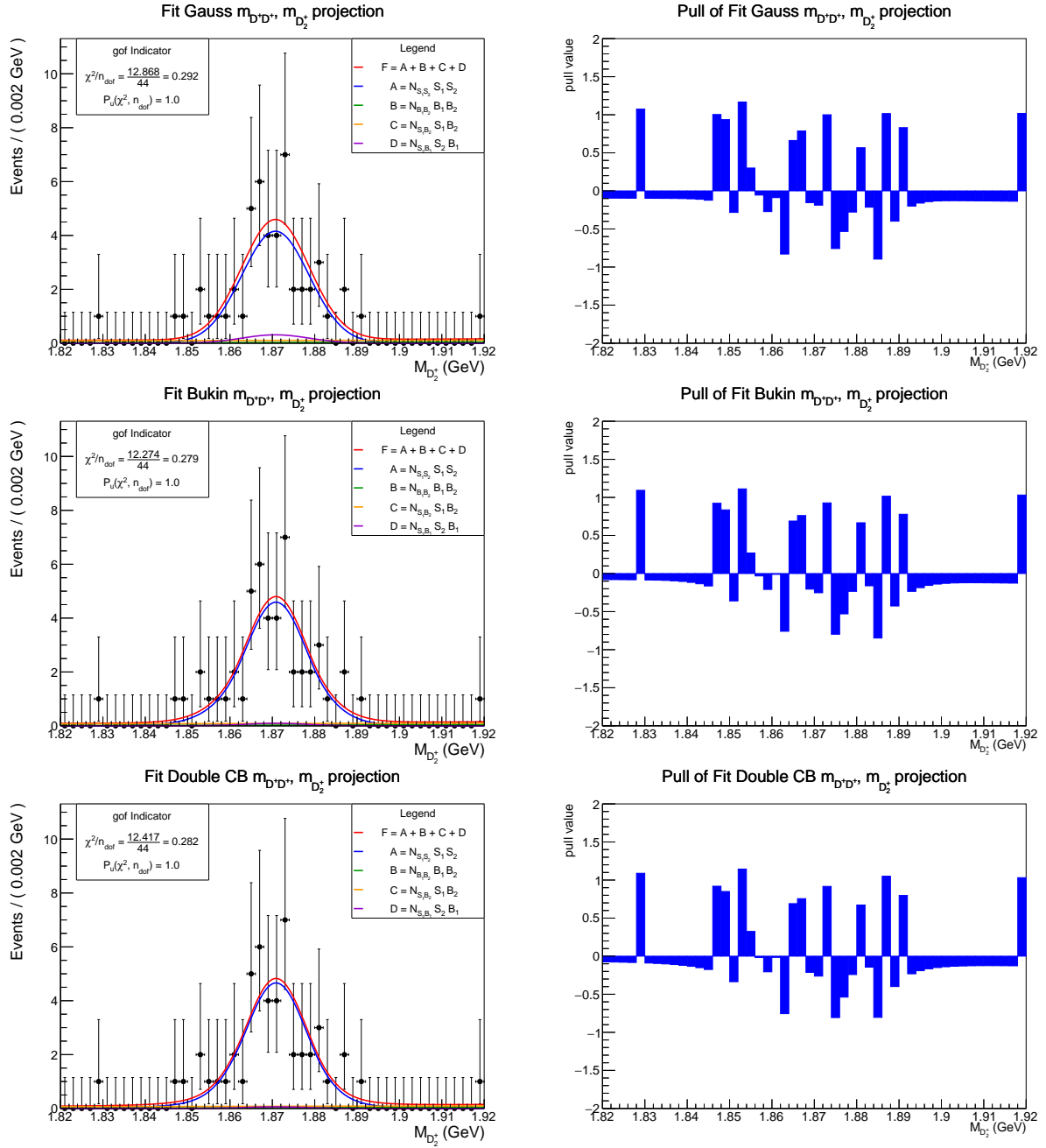
Figure 4.14: Results of the unbinned extended maximum likelihood fits to the invariant mass distribution for the double open charm event candidate D^+D^+ (including open charm pair production), $M_{D^+D^+}$, as $M_{D_2^+}$ projection. Three options for the fit model are tested. The first row shows the results for the Gaussian model, the second row the results for the Bukin model, the third row the results for the Double Crystal Ball model. In the right column the pull distributions for the corresponding model are shown.
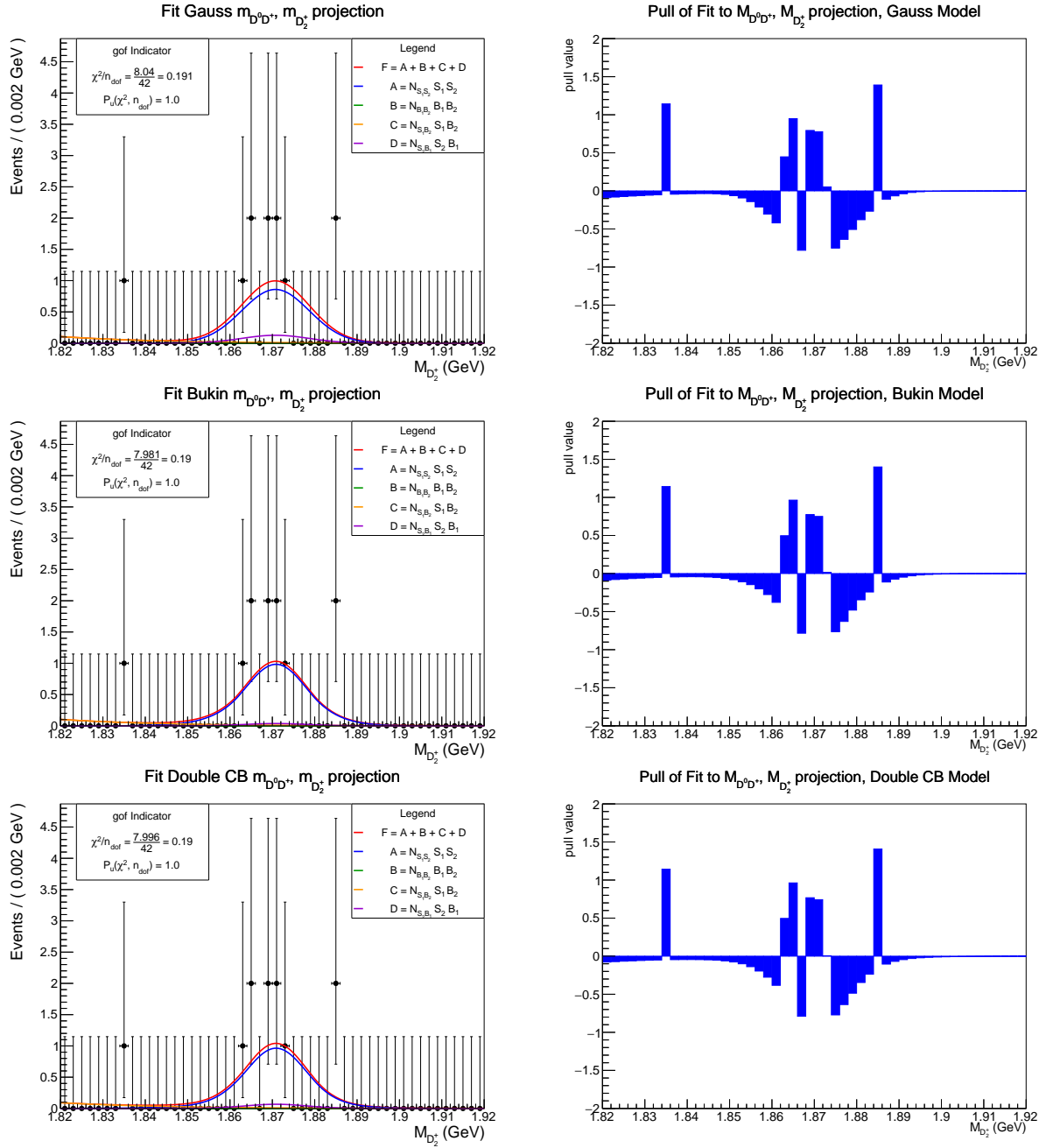
Figure 4.15: The pull distributions of the maximum likelihood fits to the invariant mass distributions $M_{D^0 D^0}$ (1st row), $M_{D^0 D^+}$ (2nd row) and $M_{D^+ D^+}$ (3rd row) (including open charm pair production) for the Bukin model (blue) and the Double Crystal Ball model (red) in direct comparison. The first column shows the $M_{D_1^0}$ projection, the second column the $M_{D_2^0}$ projection.

4.5 Efficiency Corrected Yields
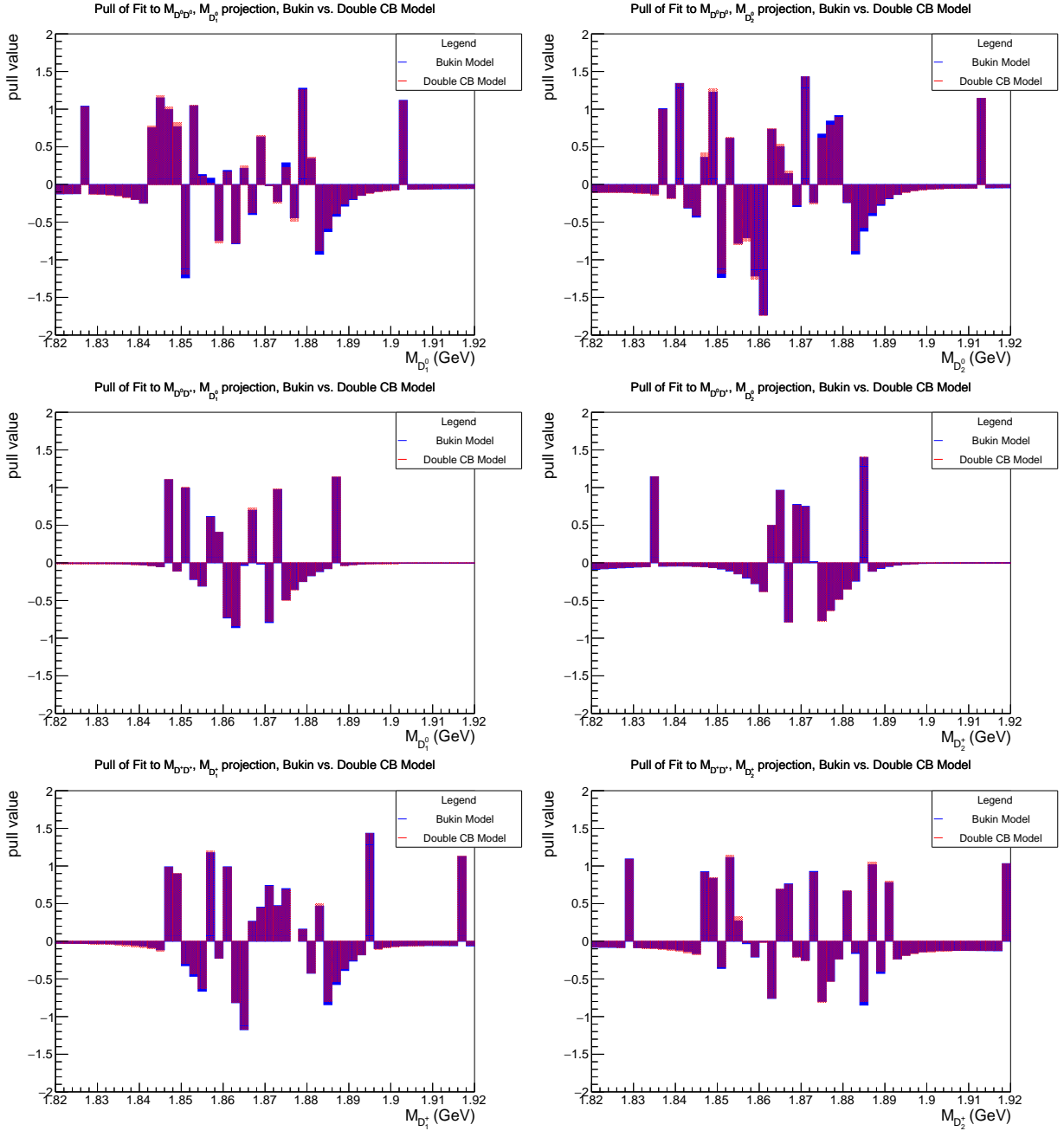
The unbinned maximum likelihood fit to the invariant mass distributions of the single resp. double open charm event candidates (including open charm pair production) provides the number of signal events N_S resp. $N_{S_1 S_2}$ and the number of background events N_B resp. $N_{B_1 B_2}$, $N_{S_1 B_2}$, $N_{S_2 B_1}$ of these event candidates (see chapter 4.4). These number of signal- or background events are the number of events expected on the average for the signal or background. Using these two average numbers, the $_s\mathcal{P}lot$ method allows to calculate the weights for each event to be signal or background [37].

Depending on the values of the fit model for the signal and background, $f_i(y_e)$, and the covariance matrix of the fit, V_{ij}, each event candidate e in the mass distribution is given a weight $w_{i,e}(y_e) \in (0,1)$, called sWeight, to be signal s and background b, where $i \in \{s,b\}$, $e \in \{1,\ldots,N_{\text{tot}}\}$, N_{tot} is the total number of events in the invariant mass distribution M and y_e is the set consisting of all parameters of the fit model inclusively the observable M. Therefore the $_s\mathcal{P}lot$ method allows to separate the desired signal events from the background events. Consequently, only the sWeights for the signal, $w_{s,e}(y_e)$, are considered in the further calculations. Including the total efficiency for each event candidate e, $\varepsilon_{\text{tot};e}(x_e)$, the efficiency corrected signal yield can be calculated by:

$$N_{c;s} = \sum_{e=0}^{N_{\text{tot}}} \frac{w_{s,e}(y_e)}{\varepsilon_{\text{tot};e}(x_e)} \quad ,$$

where $\qquad N_{\text{tot}}$: total number of events

$\qquad\qquad w_{s,e}(y_e) \in (0,1)$: weight for an event candidate e to be signal s

$\qquad\qquad \varepsilon_{\text{tot};e}(x_e)$: total efficiency for an event candidate e (see equation 4.15) .

$$\tag{4.12}$$

whereas its statistical uncertainty, $\sigma_{N_{c;s}}$, is given by:

$$\sigma_{N_{c;s}} = \sqrt{\sum_{e=0}^{N_{\text{tot}}} \left(\frac{w_{s,e}(y_e)}{\varepsilon_{\text{tot};e}(x_e)} \right)^2} \quad . \tag{4.13}$$

x_e is a set which does not consist any element of the set y_e. For example, x_e consists of p^T, η, y.

For the double open charm event candidates D^0C and $D^0\bar{C}$, where $C \in \{D^0, D^+\}$, the signal yields $N_{c,\,D^0C;\,s}$, $N_{c,\,D^0\bar{C};\,s}$ need to be corrected to take the double Cabibbo suppressed decay mode $D^0 \to K^+\pi^-$ into account, that effectively mix the D^0C and $D^0\bar{C}$ final states. This correction is given by [2], [3]:

$$N_{c,\,dcs,\,D^0C;\,s} = \frac{1}{\sqrt{1-r^2}} \left(N_{c,\,D^0C;\,s} - r\, N_{c,\,D^0\bar{C};\,s} \right)$$

$$N_{c,\,dcs,\,D^0\bar{C};\,s} = \frac{1}{\sqrt{1-r^2}} \left(-r\, N_{c,\,D^0C;\,s} + N_{c,\,D^0\bar{C};\,s} \right)$$

where $N_{c,\,D^0C;\,s}$, $N_{c,\,D^0\bar{C};\,s}$: efficiency corrected signal yields given by equation 4.12

$$r = \frac{B(D^0 \to K^+\pi^-)}{B(D^0 \to K^-\pi^+)} = (3.79 \pm 0.17) \cdot 10^{-3} \quad \text{Double Cabibbo suppression factor}$$

(4.14)

For the D^0D^0 and $D^0\bar{D}^0$ cases the value of $r_1 = 2r$ is used.

This $_s\mathcal{P}lot$ method has some disadvantages. First, it works only optimal, if the correlation between the set of variables x_e and y_e is nonexistent. The stronger the correlation is, the more difficulties the method exhibits to estimate the weights $w_{e,i}(y_e)$ properly. Since there is a correlation between M and p^T for instance, it is assumed, that the correlation between y_e and x_e is small enough, in order to let the method work properly. Secondly, the used covariance matrix V_{ij} is provided by the unbinned maximum likelihood fit to the invariant mass distributions M_C, M_{CC}. Since V_{ij} is calculated numerically, it is less accurate than the direct calculation from the log-Likelihood function by matrix inversion. However, $_s\mathcal{P}lot$ has a major advantage for this analysis. The method provides a convenient way to statistically separate all signal events from all background events. No additional selection needs to be applied, which could result in a further loss of signal events. This feature is of particular importance, since the number of event candidates is rather low due to the small dataset (e.g. compare with [2], [3]).

The distributions of the signal sWeights $w_{e,s}$ are shown in Fig. 4.16 for the single open charm event candidates D^0, D^+ and in Fig. 4.17 for the double open charm event candidates (including open charm pair production) $D^0D^0 \cup D^0\bar{D}^0$, $D^0D^+ \cup D^0D^-$, $D^+D^+ \cup D^+D^-$. The sWeights for the background have been substracted in these distributions. Bins with background events can therefore be negative. Since the double open charm and open charm pair production samples are merged, the background fractions for the double charm and pair production are assumed to be identical.

In order to separate double open charm from open charm pair production, a cut is applied on the merged samples (see Tab. 4.7). The associated functor of the cut returns the signed PDG Id of the candidate as defined by the decay descriptor. A positive value is associated with a particle, a negative value with an anti-particle. Using this cut, a charm candidate can be distinguished from its anti-charm candidate. Effectively, the cut uses the charge of the kaon for the separation, such that a differentiation between $K^-\pi^+$, $K^-\pi^+\pi^+$ and $K^+\pi^-$, $K^+\pi^-\pi^-$ final states is possible.

Candidate	Cut	Loki Functor
$D^0 D^0$	$(ID_{D_1^0} > 0 \;\&\&\; ID_{D_2^0} > 0) \;\|\|\; (ID_{D_1^0} < 0 \;\&\&\; ID_{D_2^0} < 0)$	ID
$D^0 D^+$	$(ID_{D_1^0} > 0 \;\&\&\; ID_{D_2^+} > 0) \;\|\|\; (ID_{D_1^0} < 0 \;\&\&\; ID_{D_2^+} < 0)$	ID
$D^+ D^+$	$(ID_{D_1^+} > 0 \;\&\&\; ID_{D_2^+} > 0) \;\|\|\; (ID_{D_1^+} < 0 \;\&\&\; ID_{D_2^+} < 0)$	ID
$D^0 \bar{D}^0$	$(ID_{D_1^0} > 0 \;\&\&\; ID_{D_2^0} < 0) \;\|\|\; (ID_{D_1^0} < 0 \;\&\&\; ID_{D_2^0} > 0)$	ID
$D^0 D^-$	$(ID_{D_1^0} > 0 \;\&\&\; ID_{D_2^+} < 0) \;\|\|\; (ID_{D_1^0} < 0 \;\&\&\; ID_{D_2^+} > 0)$	ID
$D^+ D^-$	$(ID_{D_1^+} > 0 \;\&\&\; ID_{D_2^+} < 0) \;\|\|\; (ID_{D_1^+} < 0 \;\&\&\; ID_{D_2^+} > 0)$	ID

Table 4.7: Cut on the ID Loki Functor in order to separate the double open charm from charm pair production events.

Figure 4.16: The distribution of the sWeights $w_{e,s}$ applied to the invariant mass distribution M for the single open charm event candidates D^0 (left) and D^+ (right).

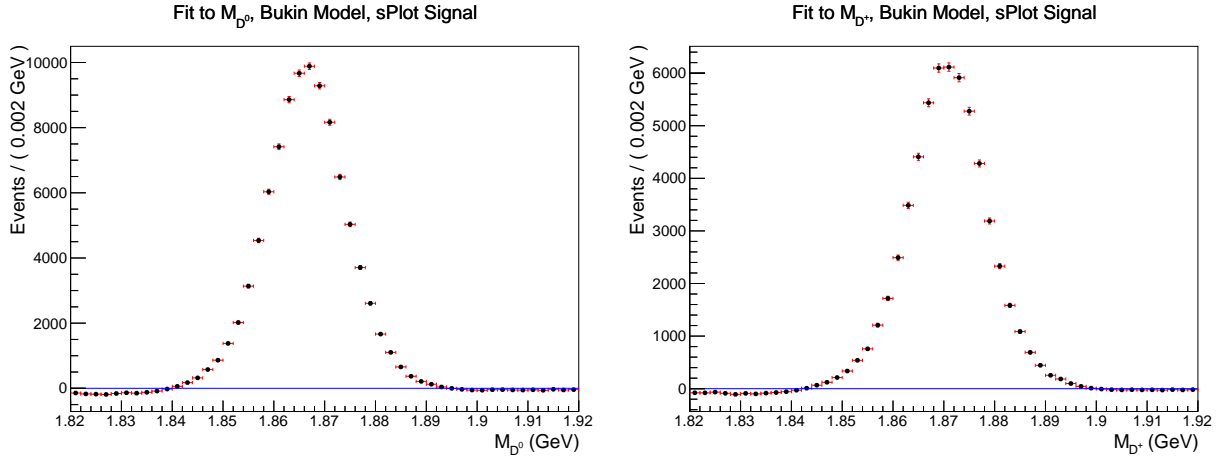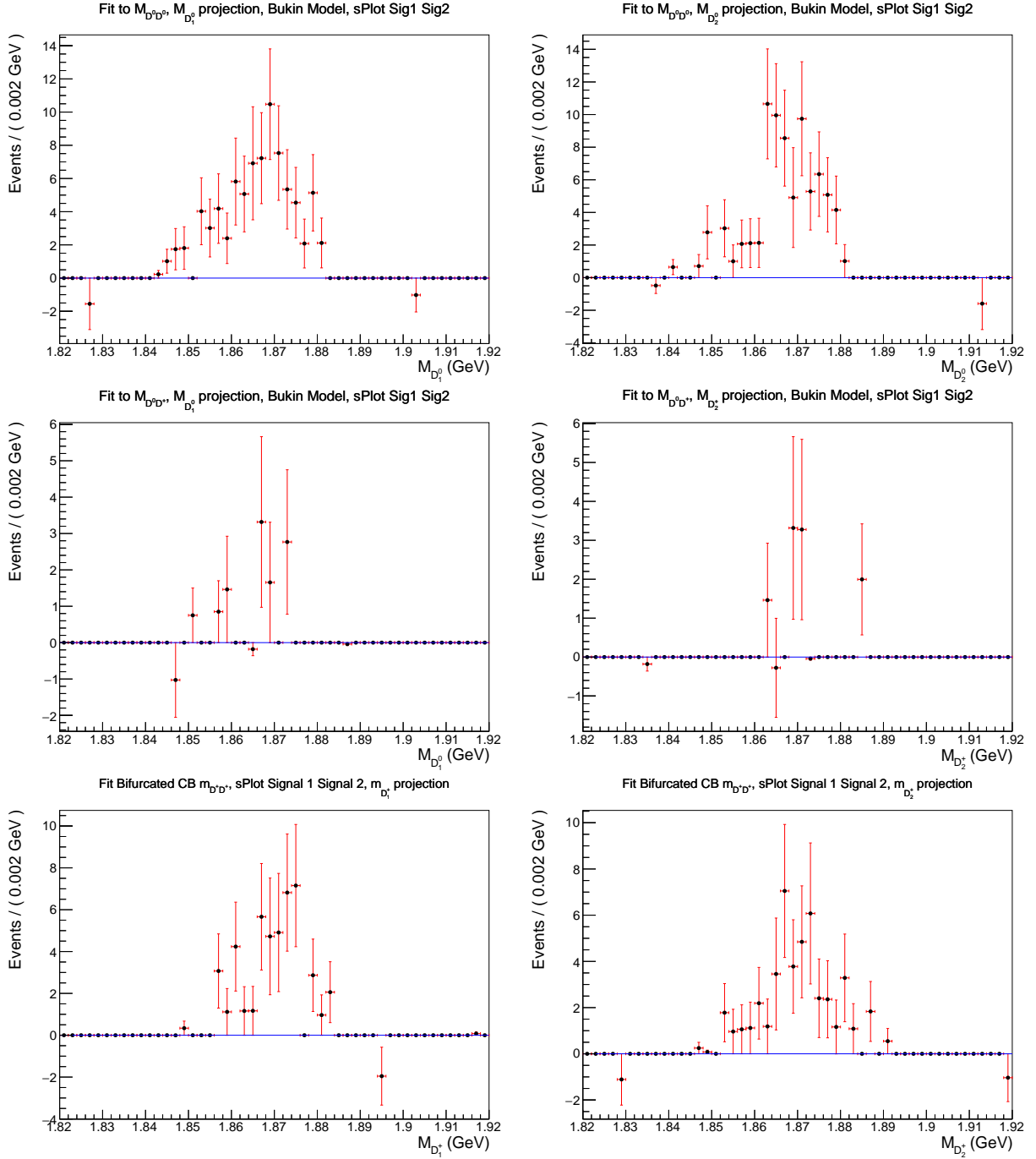Figure 4.17: The distribution of the sWeights $w_{e,s}$ applied to the invariant mass distribution M for the double open charm event candidates $D^0 D^0$ (1st row), $D^0 D^+$ (2nd row) and $D^+ D^+$ (3rd row). Due to the construction of the fit model, the sWeight distributions are 2-dimensional. The left column shows the C_1 projection, the right column the C_2 projection, whereas $C_1, C_2 \in \{D^0, D^+\}$.

4.6 Efficiency

The total efficiency for each event candidate e, $\varepsilon_{\text{tot};e}$, is a product of four terms:

$$\varepsilon_{\text{tot};e} = \varepsilon_{\text{acc};e}\ \varepsilon_{\text{rec};e}\ \xi_{\text{trk};e}\ \varepsilon_{\text{PID};e}\ \varepsilon_{\text{trg};e} \quad ,$$

$$\text{where} \quad \begin{aligned} &\varepsilon_{\text{acc};e} : \text{ acceptance} \\ &\varepsilon_{\text{rec};e} : \text{ reconstruction and selection efficiency} \\ &\xi_{\text{trk};e} : \text{ tracking efficiency correction factor} \\ &\varepsilon_{\text{PID};e} : \text{ particle identification efficiency} \\ &\varepsilon_{\text{trg};e} : \text{ trigger efficiency} \quad . \end{aligned} \tag{4.15}$$

Except for the trigger efficiency ε_{trg}, all other efficiencies, i.e. ε_{acc}, ε_{rec} (including ξ_{trk}), ε_{PID}, are taken from the analysis [28] resp. [29]. Therefore the same event selection as in [28], [29] needs to be applied for this analysis as explained in chapter 4.2.1. The efficiency for an event e is extracted by a two- resp. three-dimensional linear interpolation for that event e. The functional dependence determines the dimensionality of the interpolation. Due to the p^T and y dependence, the two-dimensional interpolation is used for the acceptance, the reconstruction and selection efficiency and the trigger efficiency. Since the PID efficiency depends on p, η and N_{tracks}, a three-dimensional linear interpolation is required.

Since a cut on the invariant mass for the single open charm candidates is applied (see chapter 4.2.1, Tab. 4.3), there is in principle a corresponding efficiency to be calculated. The cut $1.82 < M_C < 1.92$ GeV, $C \in \{D^0, D^+\}$ is applied, in order to set M_{D^0} and m_{D^+} distributions to the same range for the fits (see chapter 4.4). Initially M_{D^0} had a range of $[1.79, 1.94]$, M_{D^+} a range of about $[1.816, 1.924]$. Considering the sWeight distributions for the single open charm event candidates (see Fig. 4.16), the small signal contribution within the ranges $[1.82, 1.83]$ and $[1.91, 1.92]$, can be neglected. Since the signal contribution is not expected to rise below 1.82 GeV and above 1.92 GeV, it can be assumed, that no signal candidate is lost when applying $1.82 < M_C < 1.92$ GeV. Therefore the efficiency correponding to the mass window can be set to unity.

Acceptance ε_{acc}

The acceptance needs to be introduced, since the LHCb detector has a finite spatial acceptance. Only the forward region in the pseudorapidity range $2 < \eta < 5$ is instrumented (equal to a range of the scattering angle θ of about 10 mrad $< \theta <$ 250 mrad), so only particles flying inside this region can be detected.

The acceptance is obtained from Monte Carlo simulation using the GAUSS v45r3 framework [38], [39]. It is estimated by:

$$\varepsilon_{\text{acc}} = \frac{N_{\text{acc}}}{N_{\text{prompt}}} \quad , \tag{4.16}$$

where N_{prompt} is the number of generated prompt charm candidates in a (p^T, y)-bin and N_{acc} is the number of charm hadrons in that (p^T, y)-bin, which pass the generator-level

cuts (see [28], [29]). The estimator $\varepsilon_{\mathrm{acc}}$ is a Binomial distributed random variable, whereas the Binomial PDF is given by:

$$\mathfrak{B}(p; k, n) = \binom{n}{k} p^k (1-p)^{n-k} \quad ,$$

where n : number of trials in a counting experiment
k : number of successes
$p \in (0, 1)$: probability of success . (4.17)

Consequently the corresponding statistical uncertainty is estimated by:

$$\sigma_{\varepsilon_{\mathrm{acc}}} = \sqrt{\frac{\varepsilon_{\mathrm{acc}}(1 - \varepsilon_{\mathrm{acc}})}{N_{\mathrm{prompt}}}} \quad . \tag{4.18}$$

The acceptance for the open charm event candidates D^0 and D^+ is shown in Fig. 4.18. The estimated statistical uncertainties are in general not symmetric, which would lead to asymmetric uncertainties in each (p^T, y)-bin in Fig. 4.18. However, they are approximated symmetrically, which holds, if the corresponding efficiency in a certain (p^T, y)-bin is not too small or large.

$\varepsilon_{\mathrm{acc}}$ for the double open charm event candidates (including open charm pair production) can be decomposed into the efficiency of the single open charm event candidates:

$$\varepsilon_{\mathrm{acc}; e} = \begin{cases} \varepsilon_{\mathrm{acc}, C; e} & \text{single open charm event} \\ \varepsilon_{\mathrm{acc}, C; e} \, \varepsilon_{\mathrm{acc}, C; e} & \text{double open charm event} \end{cases} \quad ,$$

where $\varepsilon_{\mathrm{acc}, C; e}$, $C \in \{D^0, D^+\}$: Acceptance for the single open charm event candidate(s) . (4.19)
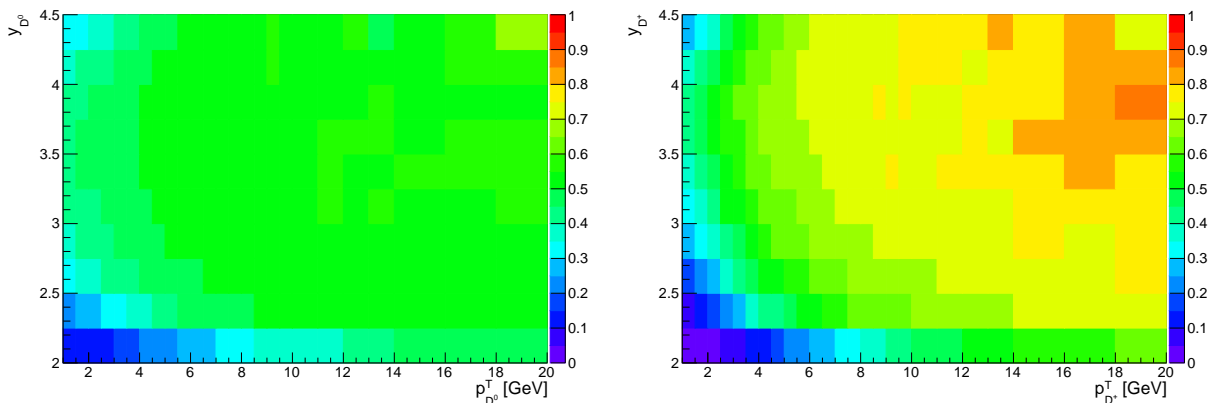
Figure 4.18: The acceptance $\varepsilon_{\mathrm{acc}}$ as a function of p^T and y for $D^0 \to K^- \pi^+$ (left) and $D^+ \to K^- \pi^+ \pi^+$ (right) decays, taken from the analysis [28], [29]. The statistical errors in each (p^T, y)-bin are symetrically approximated.

Reconstruction and Selection Efficiency $\varepsilon_{\mathbf{rec}}$

$\varepsilon_{\text{rec};e}$ is given by the product of the efficiencies for the event reconstruction and for the applied event selection without any PID cuts (see chapter 4.2.1). The PID efficiency correponding to the PID selection is determined separately. The reconstruction and selection efficiency is determined in the same way as the acceptance (see equation 4.17, 4.18). Consequently, ε_{rec} is determined from Monte-Carlo simulation and is a function of the open charm candidate's p^{T} and y. The obtained reconstruction and selection efficieny is corrected by the factor ξ_{trk} [40]. This correction factor is determined in an independent study of a pure $J\psi \rightarrow \mu^+\mu^-$ sample by a tag and probe method. It corrects for the differences in the track reconstruction between the Monte Carlo simulation and the data sample and is a function of the track momentum p_{trk} and pseudorapidity η_{trk}. The reconstruction and selection efficiency together with the correction factor is shown in Fig. 4.19. The statistical uncertainties in each (p^T, y)-bin are symmetrically approximated as for the acceptance. Since ξ_{trk} is limited to $p \in [5, 201)$ GeV and $\eta \in [1.9, 4.9)$, the correction factor for candidates with a (p, η), which exceed those limits, are given the efficiency corresponding to $p = 5.001$ resp. 199.9 GeV and $\eta = 2.001$ resp. 4.899.

For the double open charm event candidates (including open charm pair production), ε_{rec} can be decomposed into the efficiency of the single open charm event candidates and the correction factors:

$$\varepsilon_{\text{rec};e} = \begin{cases} \varepsilon_{\text{rec}, C;e}\, \xi_{\text{trk};e} & \text{single open charm event} \\ \varepsilon_{\text{rec}, C;e}\, \xi_{\text{trk};e}\, \varepsilon_{\text{rec}, C;e}\, \xi_{\text{trk};e} & \text{double open charm event} \end{cases} ,$$

where $\qquad \varepsilon_{\text{rec}, C;e},\, C \in \{D^0 D^+\}$: reconstruction and selection efficiency for the $\qquad\qquad\qquad\qquad\qquad\qquad$ single open charm event candidate(s) $\qquad$ (4.20)

$\xi_{\text{trk};e}$: correction factor for the single open charm
$\qquad\qquad$ event candidate(s) .

$\xi_{\text{trk};e}$ for a single open charm event candidate is given by the product of the correction factors for each track produced by this open charm event:

$$\xi_{\text{trk};e} = \prod_{j=\text{trk}} \xi_{e, j}\, (p_j, \eta_j) \quad ,$$

where $\qquad \xi_{e, j}(p_j, \eta_j)$: correction factor per track j $\qquad\qquad\qquad\qquad\qquad$ (4.21)

$\displaystyle\prod_{j=\text{trk}}$: product running over all final state tracks of the
$\qquad\qquad$ associated single open charm event, i.e. the K^- and π^+ .
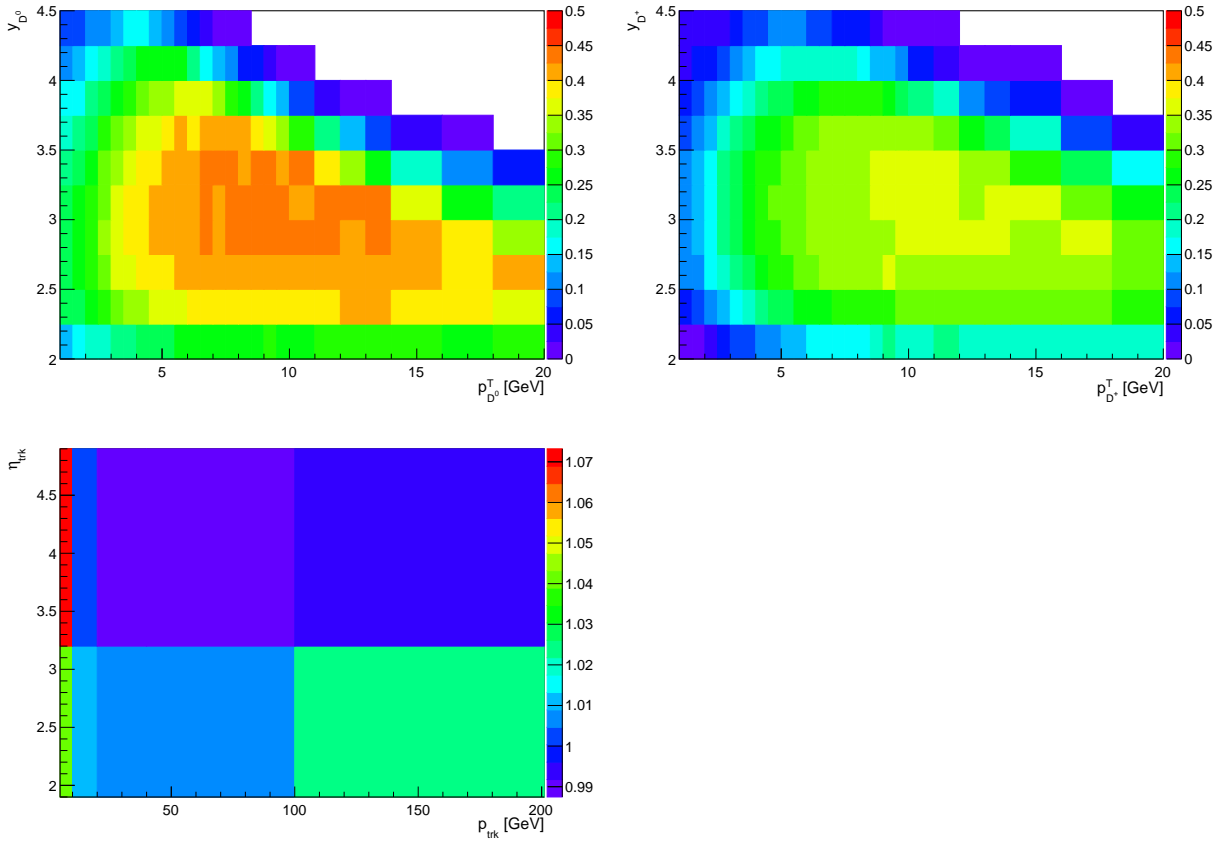
Figure 4.19: The reconstruction and selection efficiency $\varepsilon_{\mathrm{rec}}$ as a function of p^T and y for $D^0 \to K^-\pi^+$ (top left) and $D^+ \to K^-\pi^+\pi^+$ (top right) decays and for the correction factor ξ_{trk} as a function of p and η for the track candidates K^- and π^+ (bottom left), taken from the analysis [28], [29]. The statistical errors in each (p^T, y)-bin are symetrically approximated.

PID Efficiency $\varepsilon_{\mathbf{PID};e}$

The PID efficiency for the kaon and pion have been determined in [28], [29] from the analysis of calibration samples of the decay $D^{*+} \to \left(D^0 \to K^- \pi^+\right) \pi^+$ using the PIDCalib framework [42], [43], [44], [45]. $\varepsilon_{\mathrm{PID}}$ is estimated by:

$$\varepsilon_{\mathrm{PID}} = \frac{N_{\mathrm{acc}}}{N_{\mathrm{acc}} + N_{\mathrm{rej}}} = \left(1 + \frac{N_{\mathrm{rej}}}{N_{\mathrm{acc}}}\right)^{-1} \quad , \tag{4.22}$$

where N_{acc} is the number of accepted kaon resp. pion candidates in a $(p, \eta, N_{\mathrm{tracks}})$-bin, N_{rej} is the number of rejected kaon resp. pion candidates in that $(p, \eta, N_{\mathrm{tracks}})$-bin, according to the PID selection criteria (see chapter 4.2.1) and N_{tracks} is the number of track multiplicities. N_{acc} and N_{rej} are given by sums over per event weights:

$$\begin{aligned} N_{\mathrm{acc}} &= \sum_{i=acc} w_i \\ N_{\mathrm{rej}} &= \sum_{j=rej} w_j \quad . \end{aligned} \tag{4.23}$$

These weights w_i, w_j can be determined using the *sPlot* method (see chapter 4.5). Due to this, the estimator $\varepsilon_{\mathrm{PID}}$ is not a Binomial distributed random variable, and the statistical uncertainty $\sigma_{\varepsilon_{\mathrm{PID}}}$ needs to be estimated differently than for $\varepsilon_{\mathrm{acc}}$. The PID efficiency for the kaon and pionpion final states is illustrated in Fig. 4.20 resp. Fig. 4.21. Similar to the acceptance the statistical uncertainties in each $(p, \eta, N_{\mathrm{tracks}})$-bin are symmetrically approximated, since they are in general not symmetric. For certain $(p, \eta, N_{\mathrm{tracks}})$-bins the PID efficiency has values $\varepsilon_{\mathrm{PID}} \notin (0, 1]$. For these cases the bin color in Fig. 4.20, 4.21 is white. The reason for this is, that for a low number of calibration events, equation 4.22 can yield unphysical numbers for the efficiency [29]. The corresponding event candidates, which would fall into such a bin by the interpolation, is assigned a PID efficiency of $\varepsilon_{\mathrm{PID};e} = 0.5 \pm 0.5$. This occurs at the boundaries of the acceptance and is rare.

$\varepsilon_{\mathrm{PID}}$ for a single or double open charm event candidate (including open charm pair production) is given by the product of all identification efficiencies for the K^- and π^+ final state tracks:

$$\varepsilon_{\mathrm{PID};e} = \prod_{j=K^-} \varepsilon_{K^-;e,j} \prod_{j=\pi^+} \varepsilon_{\pi^+;e,j} \quad ,$$

where $\quad \varepsilon_{K^-;e,j}, \ \varepsilon_{\pi^+;e,j}$: efficiencies for K^- and π^+ identification

$\displaystyle \prod_{j=K^-}, \prod_{j=\pi^+}$: products running over all K^- resp. π^+ final state tracks of the associated single or double open charm event (including open charm pair production) .

$$\tag{4.24}$$
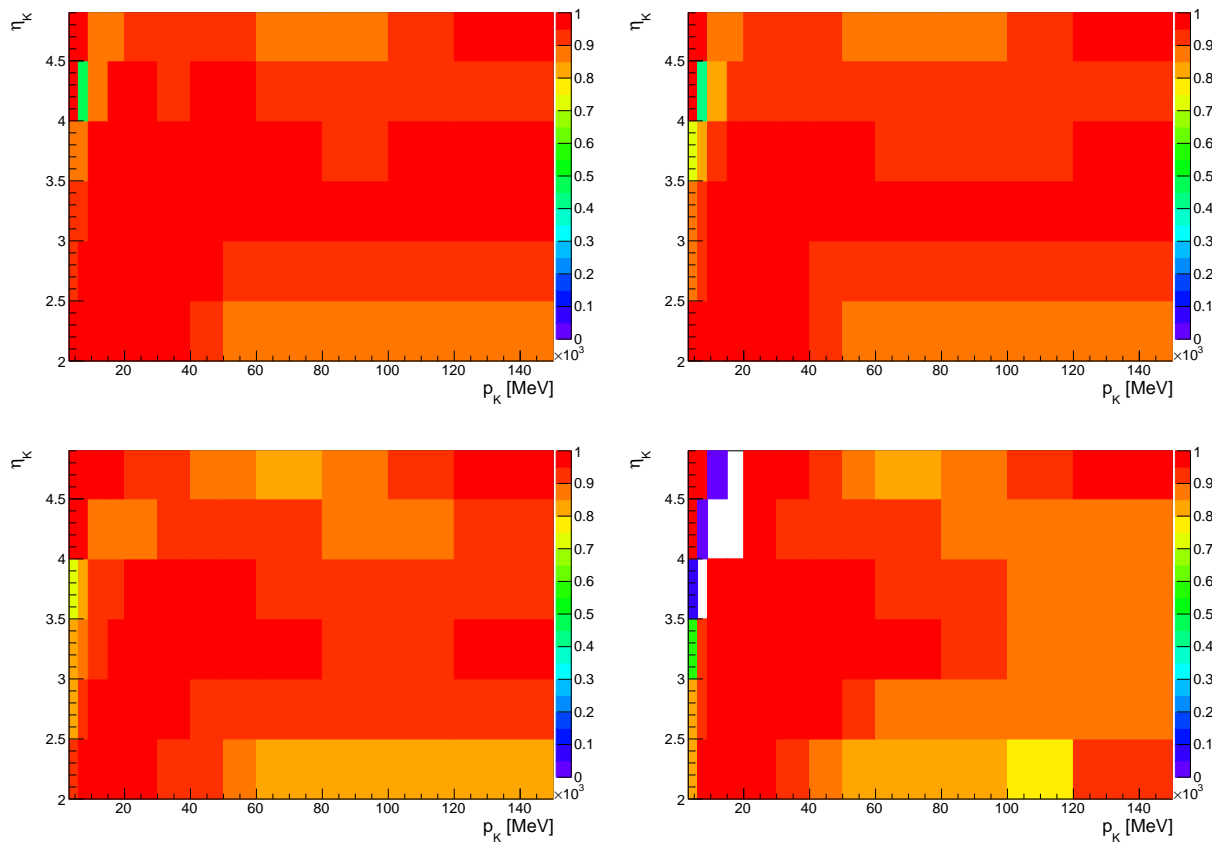
Figure 4.20: The PID efficiency $\varepsilon_{\mathrm{PID};e}$ as a function of p and η for the kaon candidates for four bins in the track multiplicity N_{tracks}: $N_{\mathrm{tracks}} \in [0, 150)$ (top left), $N_{\mathrm{tracks}} \in [150, 250)$ (top right), $N_{\mathrm{tracks}} \in [250, 400)$ (bottom left) and $N_{\mathrm{tracks}} \in [400, 1000)$ (bottom right), taken from the analysis [28], [29]. The statistical errors in each $(p, \eta, N_{\mathrm{tracks}})$-bin are symetrically approximated.

Figure 4.21: The PID efficiency $\varepsilon_{\mathrm{PID};e}$ as a function of p and η for the pion candidates for four bins in the track multiplicity N_{tracks}: $N_{\mathrm{tracks}} \in [0, 150)$ (top left), $N_{\mathrm{tracks}} \in [150, 250)$ (top right), $N_{\mathrm{tracks}} \in [250, 400)$ (bottom left) and $N_{\mathrm{tracks}} \in [400, 1000)$ (bottom right), taken from the analysis [28], [29]. The statistical errors in each $(p, \eta, N_{\mathrm{tracks}})$-bin are symetrically approximated.

Trigger Efficiency ε_{trg}

The trigger efficiency is determined directly on the data sample using the TISTOS method. It exploits the fact, that events with single open charm candidates can be triggered either by the selected decay products of the single open charm candidates (TOS: trigger on signal) or by the rest of the event (TIS: trigger independently of signal) [2], [3], [46], [47], [48], [49], [50] [51]. The overlap between these two cases allows the trigger efficiency to be calculated:

$$\varepsilon_{\text{trg}} = \frac{N_{\text{TOS} \wedge \text{TIS}}}{N_{\text{TIS}}} \quad , \tag{4.25}$$

where $N_{\text{TOS} \wedge \text{TIS}}$ is the number of TIS and TOS events in a (p^T, y)-bin, N_{TIS} is the number of TIS events in that (p^T, y)-bin and $\wedge$ is the logical and-operator (logical conjunction). Likewise to the accept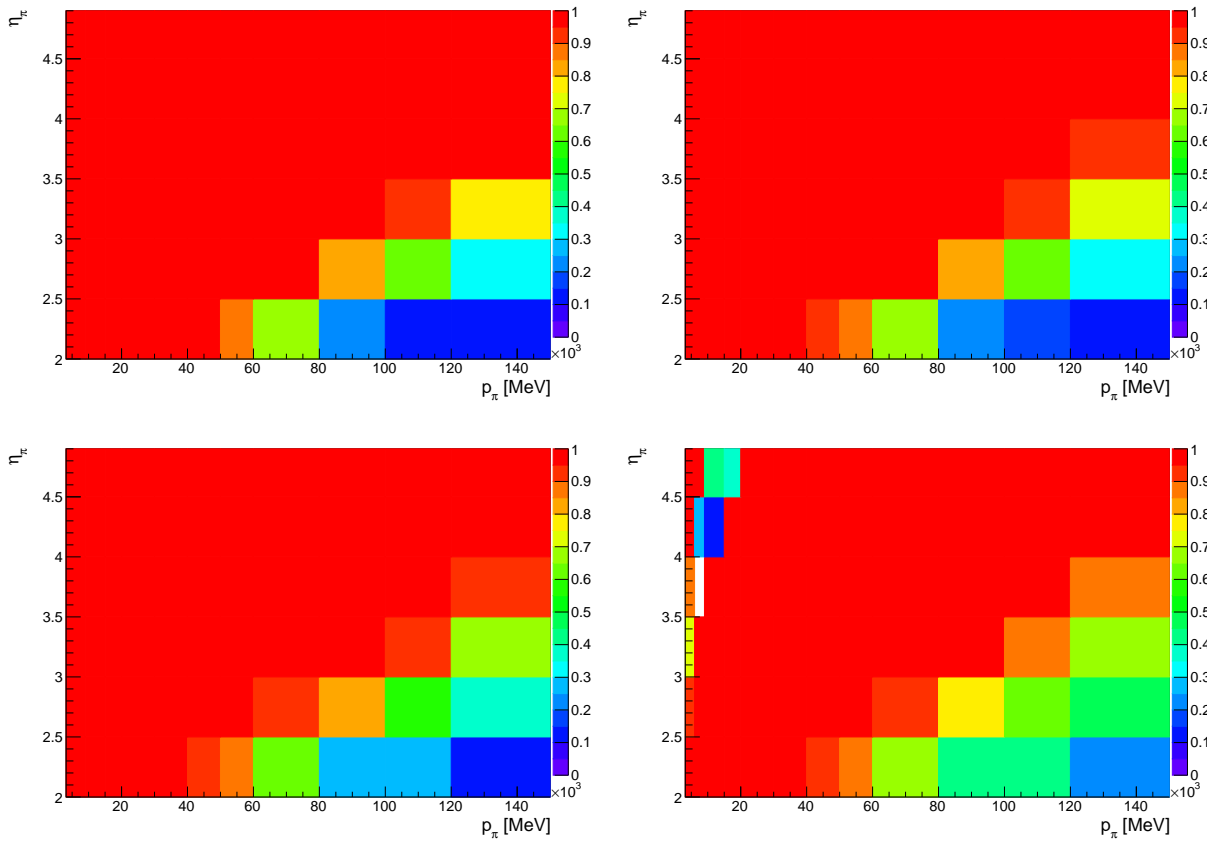ance, the trigger efficiency is estimated as a Binomial distributed random variable (see equation 4.17). However, the statistical uncertainties are estimated by the Clopper-Pearson intervals x_l and x_u within the 68.3% confidence level [52], recommended by the PDG [7]. x_l, x_u are given by:

$$\frac{1 \pm 0.683}{2} = P_l(x, a, b) = \frac{1}{\mathcal{B}(a,b)} \int_0^x t^{a-1} (1-t)^{b-1} \, dt \quad ,$$

where $\quad \mathcal{B}(a, b) = \frac{\Gamma(a)\Gamma(b)}{\Gamma(a+b)} = \int_0^1 t^{a-1}(1-t)^{b-1} \, dt$

Beta function (Euler's integral of the first kind)

x_l is given by $P_l(x, a, b) = \dfrac{1 - 0.683}{2}$ for $a = k$, $b = n - k + 1$

x_u is given by $P_l(x, a, b) = \dfrac{1 + 0.683}{2}$ for $a = k + 1$, $b = n - k$

$\mathcal{B}(p; k, n) = P_l(x; a = k, b = n - k + 1)$

Relation between the Binomial PDF and Beta PDF

used for the calculation .

$$\tag{4.26}$$

$P_l(x, a, b)$ is the lower tail probability related to the Beta PDF (see chapter 3.1.2, formula 3.13 and 3.14). Similar to equation 3.16 the Beta CDF can be splitted into the lower and upper tail probability, i.e. $C(\beta(x; a, b)) = P_l(x, a, b) + P_u(x, a, b)$, where the Beta PDF $B(x; a, b)$ and its CDF $C(B(x; a, b))$ are given by:

$$B(x; a, b) = \frac{1}{\mathcal{B}(a, b)} \, x^{a-1} \, (1-x)^{b-1}$$

$$C(B(x; a, b)) = \frac{1}{\mathcal{B}(a, b)} \int_0^1 t^{a-1} \, (1-t)^{b-1} \, dt \quad , \tag{4.27}$$

$$\text{where} \quad x \in (0, 1) : \text{observable}$$
$$a > 0, b > 0 : \text{shape parameters} \quad .$$

Moreover, $C(B(x; a, b))$ can be expressed in terms of the lower- and upper regularized incomplete Beta functions $\beta_l(x, a, b)$, $\beta_u(x, a, b)$, such that $P_l(x, a, b)$ and $P_u(x, a, b)$ are forms of $\beta_l(x, a, b)$ and $\beta_u(x, a, b)$.

The TISTOS method requires, that all single open charm event candidates are selected to be triggered as signal. This is because it determines the efficiency for an event to be triggered on signal, rather than the probability for an event to be triggered at all. Therefore all those candidates passing the trigger lines listed in Tab. 4.1 (see also chapter 4.2.1) must fulfill the TOS requirement in addition. In the case of a double open charm or open charm pair production event candidate, one of two choices can be realized. The first is to require one of the two single open charm candidates to be TOS, the second to require both to be TOS. In order not to loose event candidates unnecessarily, the first choice is picked. This leads to the combination formula 4.28. The trigger efficiency for the open charm event candidates D^0 and D^+ is shown in Fig. 4.22.

Similar to the acceptance, ε_{trg} for the double open charm event candidates (including open charm pair production) can be decomposed into the efficiency for the single open charm event candidates:

$$\varepsilon_{\text{trg};e} = \begin{cases} \varepsilon_{\text{trg},C;e} & \text{single open charm event} \\ 1 - (1 - \varepsilon_{\text{trg},C;e})(1 - \varepsilon_{\text{trg},C;e}) & \text{double open charm event} \end{cases}$$
$$\tag{4.28}$$

$$\text{where} \quad \varepsilon_{\text{trg},C;e} \, , \; C \in \{D^0, D^+\} : \text{Trigger efficiency for the single open charm}$$
$$\text{event candidate(s)}$$

Even though allowing to trigger on any of the D mesons rather than requiring both D mesons to be TOS increases the trigger efficiency, it also increases the uncertainty on the measurement of the cross sections. Unfortunately due to the small integrated luminosity only a small number of events remain for double open charm and pair production candidates (see 4.5).
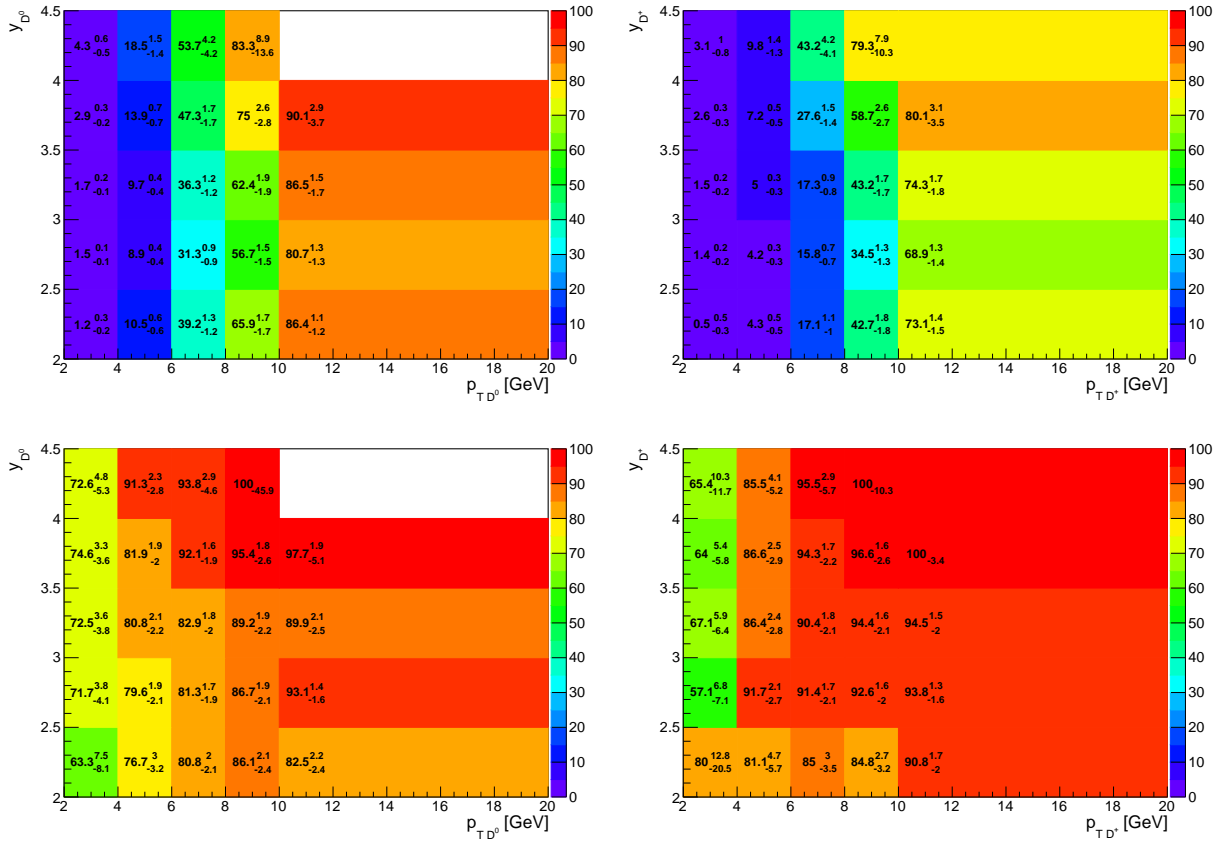
Figure 4.22: The trigger efficiency $\varepsilon_{\mathrm{trg}}$ as a function of p^T and y for the decays $D^0 \to K^-\pi^+$ (1ˢᵗ column) and $D^+ \to K^-\pi^+\pi^+$ (2ⁿᵈ column). The first row shows the efficiency for L0, the second row the one for Hlt1. The bin-wise efficiencies are given in %-values. The efficiency for the Hlt2 trigger line is given as one value: $\varepsilon_{\mathrm{Hlt2};D^0} = (80.2 \pm {}^{4.3}_{5.1})\%$ resp. $\varepsilon_{\mathrm{Hlt2};D^+} = (77.9 \pm {}^{4.1}_{4.6})\%$.

The acceptance, reconstruction and selection and trigger efficiencies can be very small for low (p^T, y)-bins (cf. Fig. 4.18, 4.19 and 4.22). Consequently, when evaluating these individual efficiencies for the candidates and combining them with equation 4.15, initially small individual efficiencies lead to an even smaller total efficiency for certain (p^T, y) events. The following example illustrates this effect. Assume, that the three efficiencies $\varepsilon_{\mathrm{acc}}$, $\varepsilon_{\mathrm{rec}}$ and $\varepsilon_{\mathrm{trg}}$ are evaluated for a single open charm event candidate e as $\varepsilon_{\mathrm{acc};e} = 0.1$, $\varepsilon_{\mathrm{rec};e} = 0.1$ and $\varepsilon_{\mathrm{trg};e} = 0.1$. When neglecting the correction factor and the PID efficiency, i.e. setting $\xi_{\mathrm{trk};e} = 1$ and $\varepsilon_{\mathrm{PID}} = 1$, the total efficiency for that event candidate e is $\varepsilon_{\mathrm{tot};e} = 0.1^3 = 0.001$. For comparison, the case $\varepsilon_{\mathrm{acc};e} = 0.5$, $\varepsilon_{\mathrm{rec};e} = 0.5$ and $\varepsilon_{\mathrm{trg};e} = 0.5$ results in $\varepsilon_{\mathrm{tot};e} = 0.5^3 = 0.125$. The evaluated total efficiency for the single open charm event candidates is shown in Fig. 4.23 and for the double open charm envent candidates (including open charm pair production) in Fig. 4.24. It is observed, that a significant amount of the event candidates have a small total efficiency. The smaller the total per event efficiency is, the

larger weight receives the correponding event in the fraction in equation 4.12 and the more dominant is the contribution of that event to the cross section (see equation 4.1). Moreover small efficiencies lead to large uncertainties because carry a much larger relative uncertainty than the large efficiencies. The major contribution leading to a small total efficiency is the trigger efficiency for the L0Hadron trigger line. It has the smallest bin contents for low (p^T, y)-bins within the largest (p^T, y)-bin range among all efficiencies. Because the trigger is optimized for high luminosity and high center of mass energy at $\sqrt{s} = 7$ TeV with high thresholds on p^T and E^T, it is not well suited for a measurement involving low p^T and low luminosity.

As a consequence, additional cuts on (p^T, y) are applied to the single open charm event candidates, in order to exclude the events with a corresponding total efficiency, which lies below a certain threshold (see Tab. 4.8). Fig. 4.25 serves as example for which all events with a corresponding total efficiency below 2% are excluded. The cut $(p^T, y) >$ (6 GeV, 2.25) is found to be well applicable for the D^0 and D^+ candidates. The loss of about 60% of the candidates is not a big issue, since there are enough candidates left for the measurement. However, the situation is different for the double open charm event candidates (including open charm pair production). The cut $(p^T, y) >$ (6 GeV, 2.25) on the two open charm does not result in any increase in the total efficiency threshold for the $D^0 D^0 \cup D^0 \bar{D}^0$ and $D^+ D^+ \cup D^+ D^-$ candidates compared to $(p^T, y) >$ (6 GeV, 2.25). Therefore the loss of event candidates is not justified and the cut $(p^T, y) >$ (4 GeV, 2.25) is found to offer best deal between gain of total efficiency and loss of event candidates. The $(p^T, y) >$ (4 GeV, 2.25) is applied for all event candidates in a special analysis (see appendix C). The effects of this additionally applied cut are further discussed in chapter 4.9, 5 and 6.

Candidate	Cut on $(p^T \text{ [GeV]}, y)$	$\varepsilon_{\text{tot, thres}}$ [%]	$f_{cut} = \frac{N_{\text{tot, cut}}}{N_{\text{tot, init}}}$ [%]
D^0	$(2, 2)$	0.02	100
	$(4, 2.25)$	0.29	85.1
	$(6, 2.25)$	1.89	54.9
D^+	$(2, 2)$	0.01	100
	$(4, 2.25)$	0.08	90.7
	$(6, 2.25)$	0.61	68.4
$D^0 D^0 \cup D^0 \bar{D}^0$	$(2, 2)$	0.02	100
	$(4, 2.25)$	0.02	72.4
	$(6, 2.25)$	0.02	56.3
$D^0 D^+ \cup D^0 D^-$	$(2, 2)$	0.03	100
	$(4, 2.25)$	0.03	100
	$(6, 2.25)$	0.15	72.7
$D^+ D^+ \cup D^+ D^+$	$(2, 2)$	0.003	100
	$(4, 2.25)$	0.06	84.3
	$(6, 2.25)$	0.06	80.4

Table 4.8: Additional applied cuts on (p^T, y) for the single open charm event candidates D^0, D^+ and double open charm event candidates (including open charm pair production) $\{D^0 D^0 \cup D^0 \bar{D}^0\}$,$\{D^0 D^+ \cup D^0 D^-\}$ and $\{D^+ D^+ \cup D^+ D^-\}$. The corresponding total efficiencies of all selected events is above $\varepsilon_{\text{tot, thres}}$ [%]. Compared to the initial cut of $(p^T, y) > (2 \text{ GeV}, 2)$, the fraction f_{cut} [%] remain in the dataset. (see 4.3).
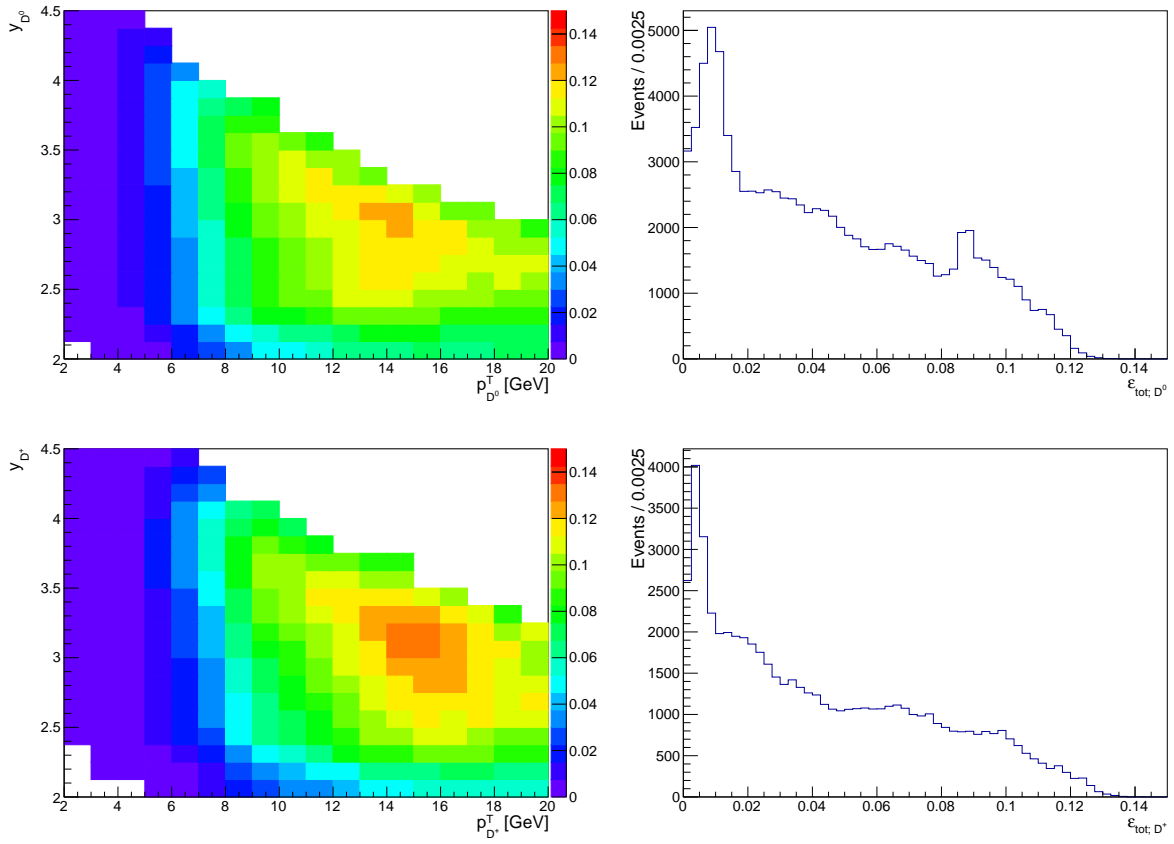
Figure 4.23: The bin-wise averaged evaluated total efficiency $\varepsilon_{\text{tot};e}$ as a function of p^T and y for the single open charm event candidates D^0 (1st row) and D^+ (2nd row).
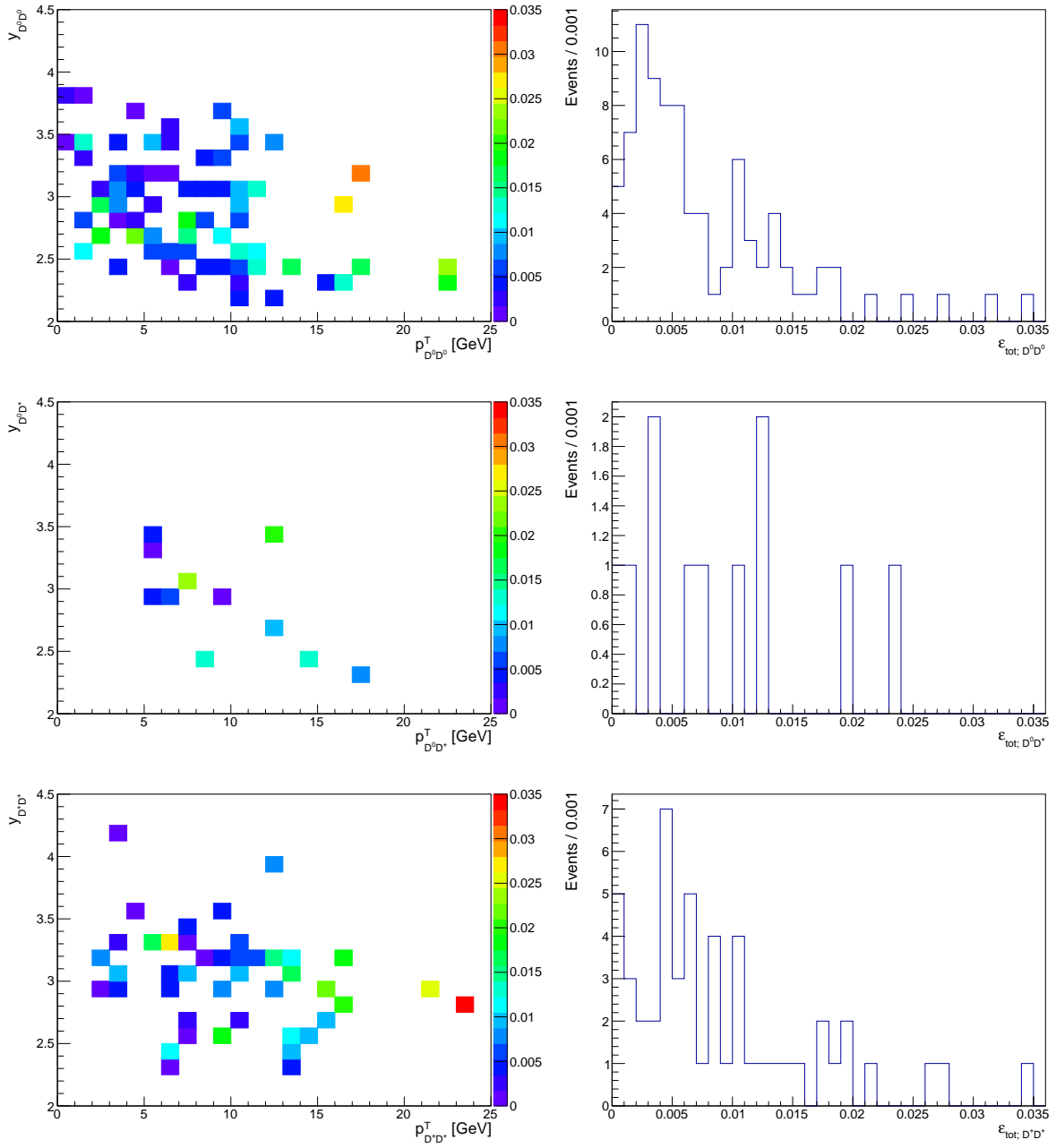
Figure 4.24: The bin-wise averaged evaluated total efficiency $\varepsilon_{\mathrm{tot};e}$ as a function of p^T and y for the double open charm event candidates $D^0 D^+$ (1st row), $D^0 D^+$ (2nd row) and $D^+ D^+$ (3rd row).
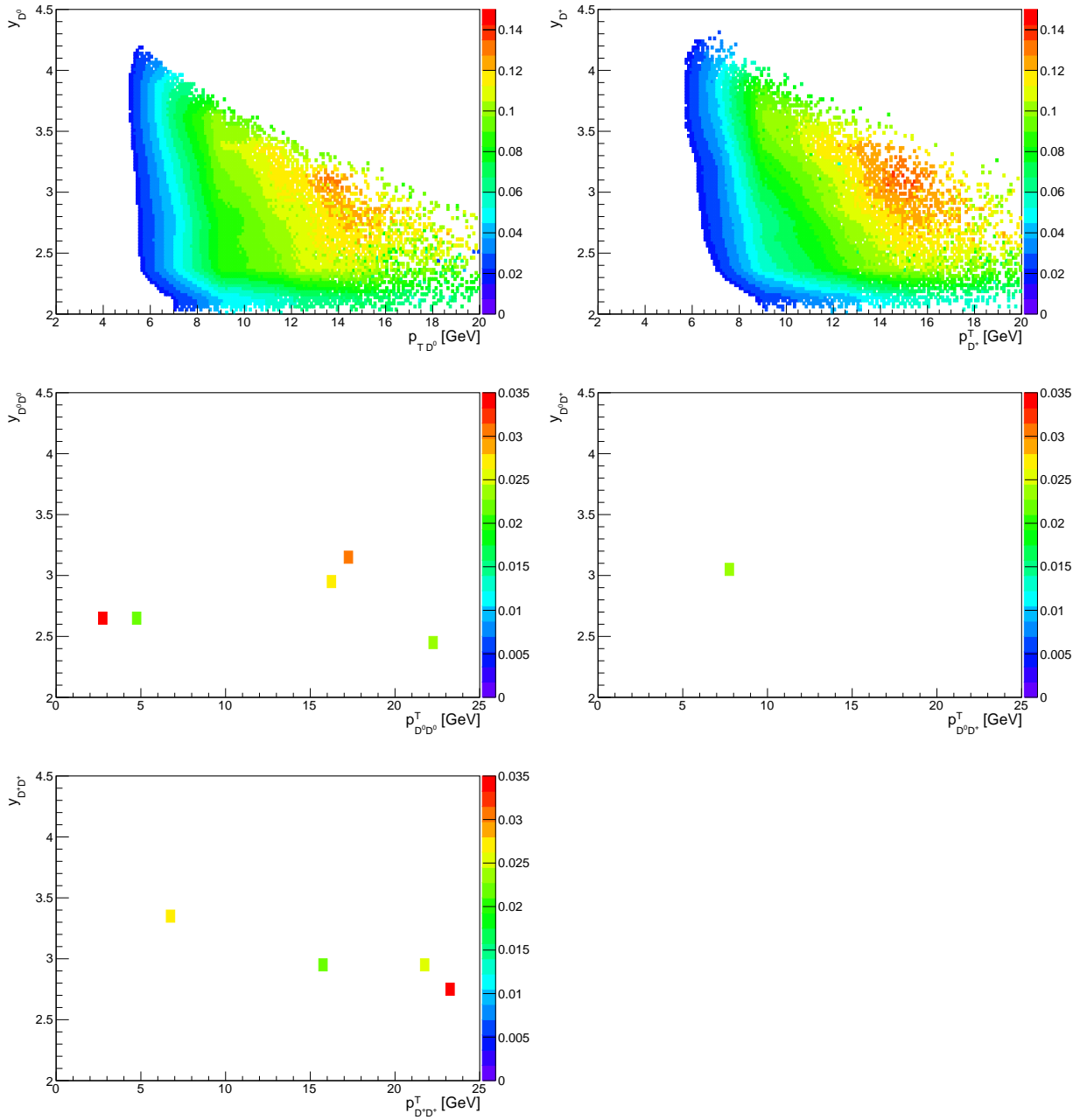
Figure 4.25: The bin-wise averaged evaluated total efficiency $\varepsilon_{\text{tot};e}$ as a function of p^T and y of the single open charm and combined double open charm (or open charm pair production) system for the D^0 (top left), D^+ (top right), $D^0 D^0 \cup D^0 \bar{D}^0$ (center left), $D^0 D^+ \cup D^0 D^-$ (center right) and $D^+ D^+ \cup D^+ D^-$ (bottom right) event candidates for an efficiency threshold of $\varepsilon_{\text{tot, thres};e} > 2\%$.

4.6.1 Global Event Cut Efficiency

The global event selection is applied on the trigger level in order to reject events with a large number of hits in the detector. For the trigger lines L0Hadron_Dec and Hlt1TrackAllL0_Dec, a cut is applied on the number of SPD hits, $N_{\mathrm{SPD}} < 600$. SPD is the abbreviation for the scintillating pad detector in the calorimetry system of the LHCb detector (see ch. 3.1.1). Initially the global event selection consisted of two cuts, $N_{\mathrm{SPD}} < 600$ and $N_{\mathrm{OT}} < 10000$. In the whole data sample there is only one event that passes the event selection but not the requirement on N_{OT}. This event passes the trigger on another trigger line. Therefore its effect on the N_{OT} distribution is neglected and the global event cut (GEC) efficiency $\varepsilon_{\mathrm{GEC}}$, can be calculated without taking N_{OT} into account. Consequently, the GEC efficiency, $\varepsilon_{\mathrm{GEC}}$, can be calculated solely from an unbinned maximum likelihod fit to the distribution of N_{SPD}, the SPD hit multiplicities. For the single open charm event candidates, a Double Gamma PDF, G, is chosen to model the distribution. This PDF is described by:

$$G(x; \mu_1, \mu_2, \gamma_1, \gamma_2, \beta_1, \beta_2) \;=\; n_1 \; g_1(x; \mu_1, \gamma_1, \beta_1) + \; n_2 \; g_2(x; \mu_2, \gamma_2, \beta_2) \quad,$$

where
$$g_i(x; \mu_i, \gamma_i, \beta_i) \;=\; \begin{cases} \frac{n_i}{\beta_i\,\Gamma(\gamma_i)} \left(\frac{x - \mu_i}{\beta_i} \right)^{\gamma_i - 1} e^{-\frac{x-\mu_i}{\beta_i}} & ,\; x - \mu_i > 0 \\ 0 & ,\; x - \mu_i < 0 \end{cases} \; , \; i \in \{1, 2\}$$

Single Gamma PDF components

$$\Gamma(k_i) \;=\; \int_0^\infty t^{k_i - 1}\, e^{-t}\, dt \quad \text{Gamma function (Euler's integral form)}$$

x : observable, i.e. N_{SPD} for the single and double charm event candidates

$k_i > 0$, $\theta_i > 0$, μ_i : free parameters of the PDF

n_i : normalization factors   .

(4.29)

For the double open charm event candidates and open charm pair produced event candidates a simpler Single Gamma PDF is chosen to model the N_{SPD} distribution. In the same way as in chapter 4.4 the double open charm and open charm pair production samples are merged, i.e. $CC \in \{D^0 D^0, D^0 D^+, D^+ D^+\} \cup \{D^0 \bar{D}^0, D^0 D^-, D^+ D^-\}$ to increase the total number of events in the corresponding N_{SPD} distributions. The result of the fit is shown for the D^0 and D^+ candidates in Fig. 4.26 and for the $D^0 D^0$, $D^0 D^+$, $D^+ D^+$ including the $D^0 \bar{D}^0$, $D^0 D^-$, $D^+ D^-$ candidates in Fig. 4.27, the corresponding fit parameters in Tab. B.1 and Tab. B.2.

As alternative fit models for the single open charm event candidates, the simpler Single Gamma PDF and stretched Beta PDF have been tested (see equation B.1). However they pion describe the tail of the N_{SPD} distribution as well as the Double Gamma PDF G (cf. Fig. 4.26, 4.28, 4.29 and corresponding fit parameters in Tab. B.1, B.3, B.4). However, the Single Gamma PDF is able to model the N_{SPD} distribution for the double open charm event candidates due to the lower statistics.

In the actual fitting algorithm the factors n_i, $1/\beta_i$, $1/\Gamma(\gamma_i)$ are absorbed into the overall

normalization N_i, i.e. $N_i = \frac{n_i}{\beta_i \Gamma(\gamma_i)}$, $i \in \{1, 2\}$. These overall normalization factors do not represent the number of events anymore. To have access to normalization factors representing number of events, an integral representation can be used. The number of events in a given interval $[a, b]$, $N_{[a, b]}$ are given by:

$$N_{[a, b]} = \int_a^b G(x; \mu_1, \mu_2, \gamma_1, \gamma_2, \beta_1, \beta_2) \; dx \quad , \, a > 0, \, b > 0, \, b > a \quad ,$$

where $\quad G(x; \mu_1, \mu_2, \gamma_1, \gamma_2, \beta_1, \beta_2)$: Double Gamma PDF $\hfill (4.30)$

$\quad\quad\quad x$: observable, i.e. N_{SPD} for the cases of the single and double

$\quad\quad\quad\quad$ open charm event candidates .

The GEC efficiency $\varepsilon_{\mathrm{GEC}}$ can then be determined from $N_{[n_{\mathrm{cutoff}}, \infty]}$, where $n_{\mathrm{cutoff}} = 600$, and $N_{[0, \infty]}$ by:

$$
\begin{aligned}
\varepsilon_{\mathrm{GEC}} &= \frac{N_{[0, n_{\mathrm{cutoff}}]}}{N_{[0, \infty]}} = \frac{\int_0^{n_{\mathrm{cutoff}}} G(x; \mu_1, \mu_2, \gamma_1, \gamma_2, \beta_1, \beta_2) \; dx}{\int_0^{\infty} G(x; \mu_1, \mu_2, \gamma_1, \gamma_2, \beta_1, \beta_2) \; dx} \\
&= 1 - \frac{N_{[n_{\mathrm{cutoff}}, \infty]}}{N_{[0, \infty]}} = 1 - \frac{\int_{n_{\mathrm{cutoff}}}^{\infty} G(x; \mu_1, \mu_2, \gamma_1, \gamma_2, \beta_1, \beta_2) \; dx}{\int_0^{\infty} G(x; \mu_1, \mu_2, \gamma_1, \gamma_2, \beta_1, \beta_2) \; dx} \quad .
\end{aligned}
\tag{4.31}
$$

Due to the cut $N_{\mathrm{SPD}} < 600$, the fit model needs to be extrapolated into the region $N_{\mathrm{SPD}} \geq 600$, in order to determine the number of events in that region, $N_{[n_{\mathrm{cutoff}}, \infty]}$. For the calculation of the total number of events, $N_{[0, \infty]}$, it is not possible to implement the infinity, ∞, numerically. Instead, the representation $\infty := 100000$ is used. This number is much larger than the number of cells in the SPD detector, i.e. the maximal value for N_{SPD}. Using uncorrelated systematical error propagation, the uncertainty on $\varepsilon_{\mathrm{GEC}}$, $\sigma_{\varepsilon_{\mathrm{GEC}}}$, is given by:

$$\sigma_{\varepsilon_{GEC}} = \sigma_{N_{[n_{\mathrm{cutoff}}, \infty]}} \frac{1}{N_{[0, \infty]}} + \sigma_{N_{[0, \infty]}} \frac{N_{[n_{\mathrm{cutoff}}, \infty]}}{N_{[0, \infty]}^2} \tag{4.32}$$

The GEC efficiencies for each single and double open charm event candidate (including open charm pair production) are listed in Tab. 4.9. It is observed, that the GEC efficiency is $\varepsilon_{\mathrm{GEC}} > 0.9999$ in all cases. Therefore the effect on the cross section is very small, such that it can be neglected, i.e. $\varepsilon_{\mathrm{GEC}}$ can be set to unity. This is a much larger GEC efficiency than it is usually observed in high luminosity data taking. This is due to the reduced number of visible interactions ($\mu \simeq 1$) in the used data taking period for this measurement.

Candidate	$1 - \varepsilon_{\mathrm{GEC}}$
D^0	$(2.38 \pm 0.36) \cdot 10^{-5}$
D^+	$(2.05 \pm 0.43) \cdot 10^{-5}$
$D^0 D^0 \cup D^0 \bar{D}^0$	$(1.06 \pm 6.19) \cdot 10^{-5}$
$D^0 D^+ \cup D^0 D^-$	$(4.03 \pm 5.07) \cdot 10^{-7}$
$D^+ D^+ \cup D^+ D^-$	$(7.10 \pm 22.86) \cdot 10^{-6}$

Table 4.9: Results of the global event cut inefficiency for the single open charm event candidates D^0, D^+ and double open charm event candidates (including open charm pair production) $\{D^0 D^0 \cup D^0 \bar{D}^0\}$,$\{D^0 D^+ \cup D^0 D^-\}$ and $\{D^+ D^+ \cup D^+ D^-\}$.
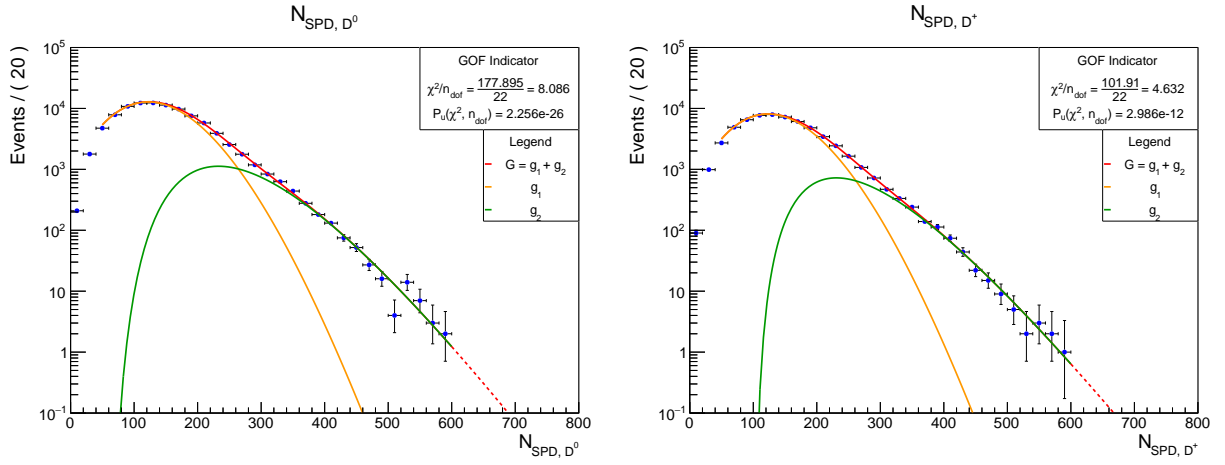
Figure 4.26: Results of the unbinned maximum likelihood fit using the Double Gamma model to the N_{SPD} distribution for the single open charm event candidates D^0 (left) and D^+ (right).
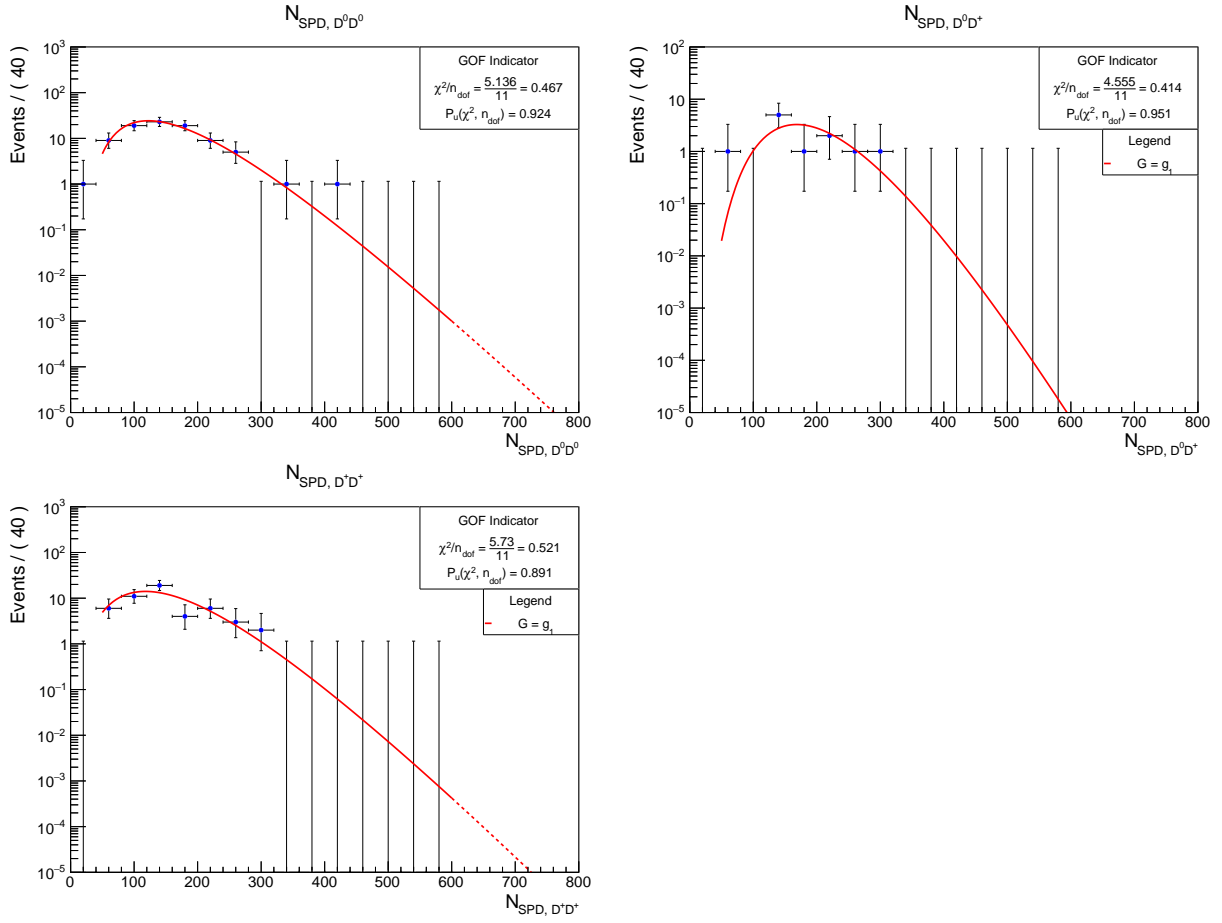
Figure 4.27: Results of the unbinned maximum likelihood fit using the double Gamma model to the N_{SPD} distribution for the double open charm event candidates (including open charm pair production) $\{D^0 D^0 \cup D^0 \bar{D}^0\}$ (top left), $\{D^0 D^+ \cup D^0 D^-\}$ (top right), $\{D^+ D^+ \cup D^+ D^-\}$ (bottom left).
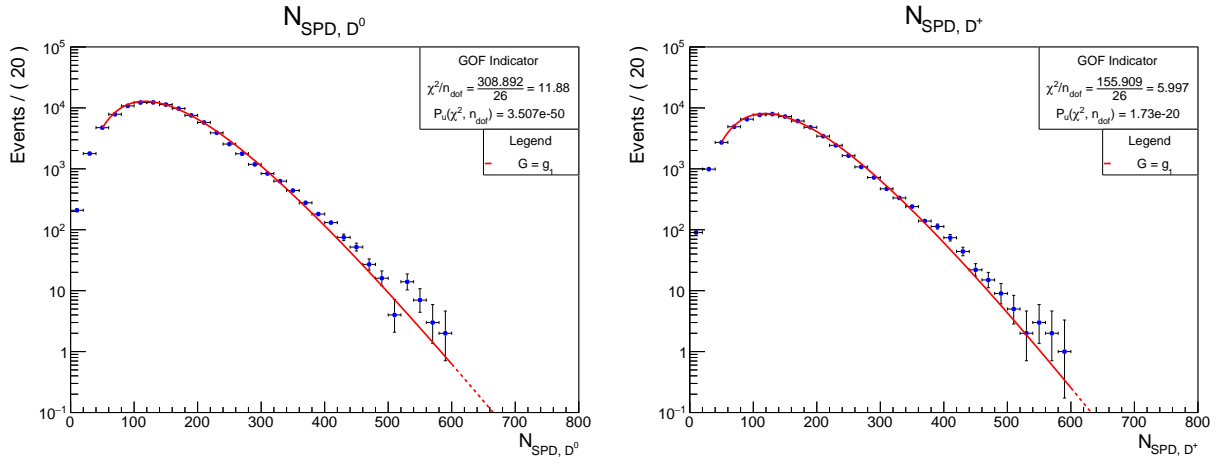
Figure 4.28: Result of the unbinned maximum likelihood fit to the N_{SPD} distribution using a Single Gamma model for the single open charm event candidates D^0 (left), D^+ (right).
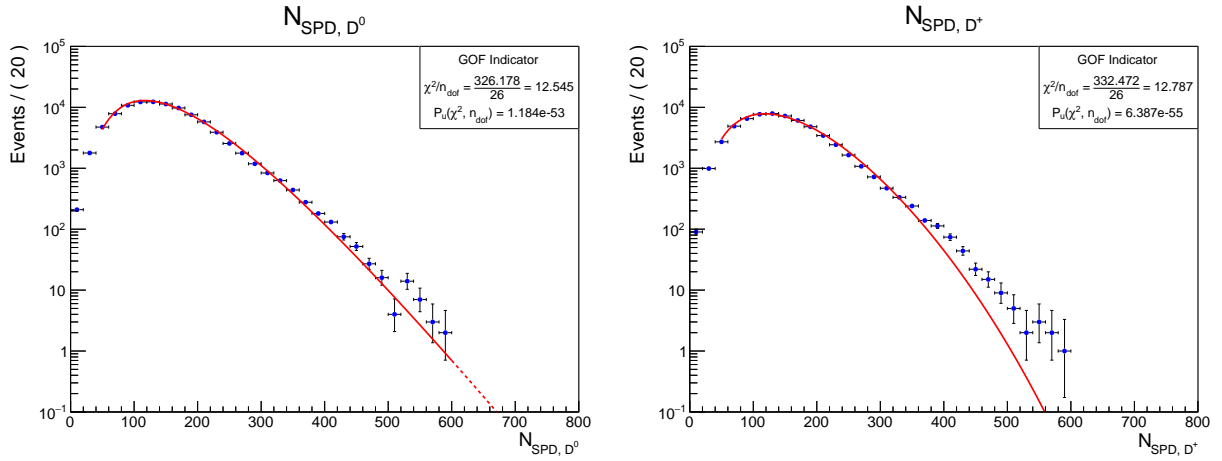
Figure 4.29: Result of the unbinned maximum likelihood fit to the N_{SPD} distribution using a Beta model for the single open charm event candidates D^0 (left), D^+ (right).

4.7 Integrated Luminosity

The integrated luminosity $\mathscr{L}$ together with its uncertainty $\sigma_{\mathscr{L}}$ of $\mathscr{L} = 3.31 \pm 0.07$ pb^{-1} is given by the common LHCb luminosity tool implemented in the DaVinci software package for LHCb. This tool uses two measurement methods to determine the luminosity, the Van-der-Meer scan and the Beam-Gas-Interaction method [53], [54], [55]. $\sigma_{\mathscr{L}}$ is treated as a systematical uncertainty in the error propagation for the cross section. The influence of $\sigma_{\mathscr{L}}$ on the cross section uncertainty can then be stated as a separate value.

4.8 Branching Ratios

The branching ratios for the D^0 and D$^+$ open charm event candidates are taken from the PDG [7]. They are listed in Tab. 4.10. For the double open charm event candidates D^{0}D^0, D^{0}D$^+$ and D$^+$D$^+$, these branching ratios are combined to one value before entering the cross section formula (see eqn. 4.1). $B_{D^0 \to K^+\pi^-}$ is used for the correction in equation 4.14. As for the luminosity, the uncertainty on the branching ratio is treated as a systematical uncertainty, such that its influence on the cross section uncertainty can be stated as a separate value.

Candidate	B
$D^0 \to K^-\pi^+$	$(3.93 \pm 0.04) \cdot 10^{-2}$
$D^0 \to K^+\pi^-$	$(1.49 \pm 0.07) \cdot 10^{-4}$
$D^+ \to K^-\pi^+\pi^+$	$(9.46 \pm 0.24) \cdot 10^{-2}$

Table 4.10: Branching ratios for the decay modes $D^0 \to K^-\pi^+$, $D^0 \to K^+\pi^-$ (double cabibbo suppressed) and $D^+ \to K^-\pi^+\pi^+$ [7].

4.9 Systematic Uncertainties

The major source of systematic uncertainty originates from the determination of the efficiencies defined by equation 4.15. Any other source is not considered in this analysis. The systematic uncertainty is estimated by a toy Monte Carlo method. First, the efficiencies ε_{acc}, ε_{rec}, ε_{PID}, provided by the analysis [28] resp. [29], and ε_{trg} are randomly varied within their uncertainties. ξ_{trk} is not varied, since the corrections are small. For each bin i in the histograms, its bin content ε_i is substituted by $\varepsilon_i \to \varepsilon_i'$. For ε_{acc}, ε_{rec}, ε_{PID} the variation ε_i' is given by a Gaussian distributed random value truncated to the interval $(0, 1]$, while for ε_{trg} the variation is given by a Beta distributed random value. The bin contents ε_i represent the means μ_i and the symmetrically approximated bin errors σ_i the standard deviations $\sigma_{\text{gaus};\, i}$ of the Gaussian PDF needed to generate the corresponding random values in each bin i. The Gaussian PDF is given by:

$$
N(x; \mu, \sigma) \;=\; \frac{1}{\sqrt{2\,\pi}\,\sigma} \; \exp\left(-\frac{1}{2} \left(\frac{x - \mu}{\sigma} \right)^2 \right) \quad ,
$$

$$
\begin{aligned}
\text{where} \qquad &x : \text{Observable} \\
&\mu : \text{Mean; also being the expectation value} \\
&\sigma : \text{Standard deviation}
\end{aligned}
$$

(4.33)

For the trigger efficiency the number of events being TOS and TIS, $N_{\text{TOS} \wedge \text{TIS}}$, and the number of events being TIS, N_{TIS}, can be identified as the k and n parameters of the Binomial distribution, repectively (see equation 4.17). Since the Beta distribution is interpreted as the continuous generalization of the Binomial distribution for real k and n within the interval $(0, 1)$, the parametrization $a = k+1$, $b = n-k+1$ is used determine the two shape parameters a and b of the Beta PDF needed to generate the corresponding random value in each bin i (see equation 4.27, 4.26). The case of an unphysical efficiency, i.e. for certain bins of ε_{PID}, resulting a uniform PDF within $(0, 1)$, is included in this representation.

Then, all steps to evaluate the the total efficiency for each event candidate e, $\varepsilon_{\text{tot};\, e}$, are executed for each variation ε_i'. This leads to variations for the total efficiency $\varepsilon_{\text{tot};\, e,\, j}'$ for each event candidate e and for each variation j. Using equation 4.1, the procedure leads to variations for the cross section, σ_j'. The cross section distributions obtained from these toy experiments are shown in Fig. 4.31 for the single open charm event candidates and in Fig. 4.32 and 4.33 for the double open charm event candidates (including open charm pair production). It is observed, that these distributions have an upper tail. This behavior is likely caused by those events, which have the smallest total efficiency.

Since the trigger efficiency is observed to be the major cause for small event-wise total efficiencies (see chapter 4.6), the choice of the Beta PDF is important. It is expected, that when using the Gaussian PDF for the variation of the trigger efficiency instead of the Beta PDF, the cross section distribution obtained from the toy experiments have an even larger upper tail.

The tendency for large tails is the reason, that the standard deviation of the variations is not a viable estimator for the systematical uncertainty on the cross section $\sigma_{\mathrm{ana};\sigma}$:

$$\sigma_{\mathrm{ana};\sigma} = \sqrt{\frac{1}{n_j - 1} \sum_{j=1}^{n_j} \left(\sigma'_j - \mu(\sigma'_j)\right)^2}$$

$$\text{where} \quad \mu(\sigma'_j) = \frac{1}{n_j} \sum_{j=1}^{n_j} \sigma'_j \quad \text{Mean of the variations } \sigma'_j \tag{4.34}$$

$$\sum_{j=1}^{n_j} : \text{Sum running over all variations } \sigma'_j$$

Large variated cross section values have a bigger contribution in this equation than small ones, resulting in an overestimation of the systematic uncertainty $\varepsilon_{\mathrm{ana};\sigma}$. Therefore, this systematic uncertainty is determined differently by using the cross section distribution for the toy experiments. The confidence interval is calculated as the smallest interval, containing 68.3% of the toy experiments. In case $n_j \cdot 0.683$ does not yield an integer, it is set to the next larger integer. The lower- and upper interval boundaries, denoted as *LowerBound* and *UpperBound*, are then given by the center value between the variated cross section value lying inside the interval and the next variated cross section value lying outside the interval (see Fig. 4.30). Then, the lower- resp. upper systematic uncertainties are estimated as:

$$\begin{aligned} \sigma_{\mathrm{ana,\ low};\sigma} &= Mode - LowerBound \\ \sigma_{\mathrm{ana,\ high};\sigma} &= UpperBound - Mode \quad . \end{aligned} \tag{4.35}$$

The *Mode* is calculated analogously to *Lower Bound* and *Upper Bound* as the center between the the interval boundaries corresponding to the confidence interval of 0.1. It is drawn as a red star, while the systematic uncertainty estimations are drawn as black error bars in Fig. 4.31 to 4.33. This estimate for the systematic uncertainty is referred to as the systematic uncertainty related to the analysis in chapter 5. For comparison, the unvaried cross section values, the mean, the median and the standard deviation are denoted as *Best Value, Mean, Median* and *RMS*. The latter three quantities are calculated based on the binned cross section distributions. The *Best Value* is drawn as a green star in Fig. 4.31 to 4.33. A substantial number of toy experiments are required, such that statistical fluctuations can balance out. The number of variations $n_j = 1000$ leads to reasonable populated histograms, expecially needed in order to determine the *Mode* properly.

Bias of the Method

For some candidates, the cross section values obtained from the toy experiments tend to be smaller than the *Best Value*. Sometimes the *Best Value* is higher than the *Lower Bound* (see Fig. 4.31). This is expected, since the way the efficencies are varied, lead to efficiency values with a slight bias towards high efficiencies, i.e. low cross sections. This arises from truncating the Gaussian PDF to (0, 1] or using the asymmetric Beta PDF for efficiencies

less than 0.5. The first hypothesis during the analysis was, that the usage of the truncated Gaussian PDF yielding a finite probability density for efficiencies close to zero leads to the excessive event weights. This was the reason for replacing the truncated Gaussian PDF with a Beta PDF for the smallest efficiencies, i.e. the trigger efficiencies. This solves the problem in a large part, since the bias in the total efficiency and in every event is small, as it can be seen in Fig. 4.34. The current interpretation of this behavior is, that the Central Limit Theorem holds for sums but not for products like the total efficiency (see equation 4.15). This explains why the RMS is an inferior estimator for the confidence interval. Since the bias is small, the method to propagate the systematic uncertainties on the efficiencies to the cross section is useful. However, the distributions of the cross sections get more biased the smaller the involved efficiencies are. As expected, the method works better for the cross section ratios.
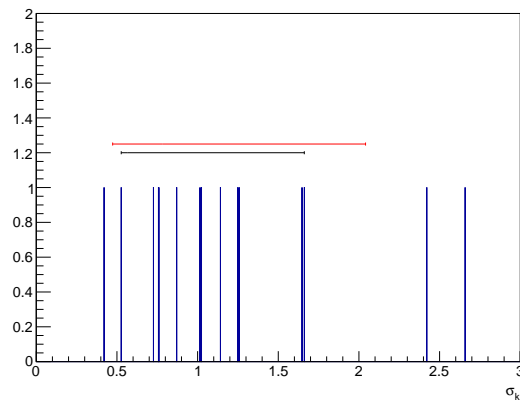
Figure 4.30: Illustration of the procedure used to estimate the systematic uncertainty on the cross section σ_{ana}. In this example of a toy experiment 15 cross section values are calculated, where $k \leq 15$.
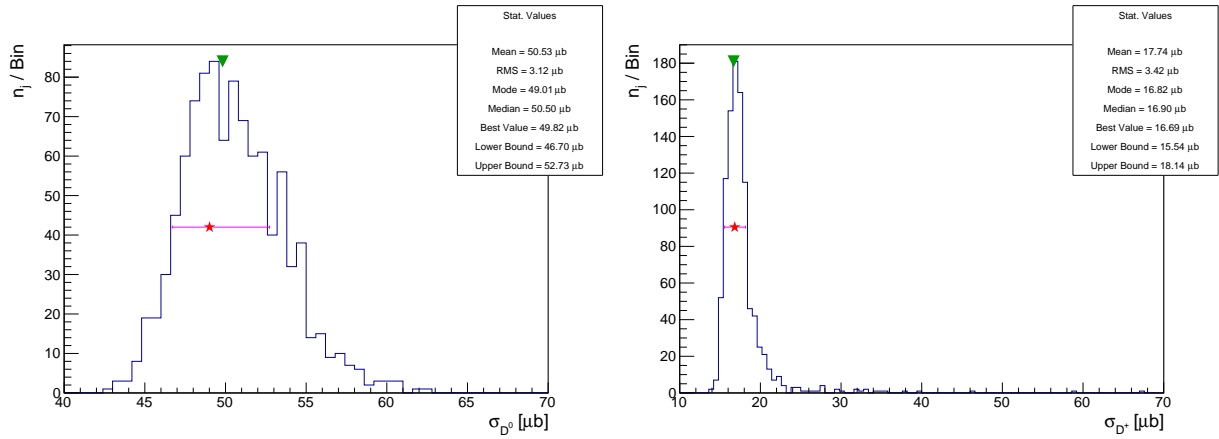
Figure 4.31: Cross section distributions obtained from the toy experiments for the single open charm event candidates D^0 (left) and D^+ (right). The mode of a distributions is denoted as *Mode* and drawn as a red star, while the cross section value calculated by the analysis is denoted as *Best Value* and drawn as green triangle. The parameters *Lower Bound* and *Upper Bound* correspond to the lower and upper end points of the error bar, drawn in pink. The other statistics parameter calculated from the binned distributions are the mean, median and standard deviation, denoted as *Mean*, *Median* and *RMS*.

Figure 4.32: Cross section distributions obtained from the toy experiments for the double open charm event candidates $D^0 D^0$ (top left), $D^0 D^+$ (center left), $D^+ D^+$ (bottom left) and for the open charm pair production event candidates $D^0 \bar{D}^0$ (top right) and $D^+ D^-$ (bottom right). No event candidate is observed for the $D^0 D^-$. The mode of a distributions is denoted as $Mode$ and drawn as a red star, while the cross section value calculated by the analysis is denoted as $BestValue$ and drawn as green triangle. The parameters $LowerBound$ and $UpperBound$ correspond to the lower and upper end points of the error bar, drawn in pink. The other statistics parameter calculated from the binned distributions are the mean, median and standard deviation, denoted as $Mean$, $Median$ and RMS.
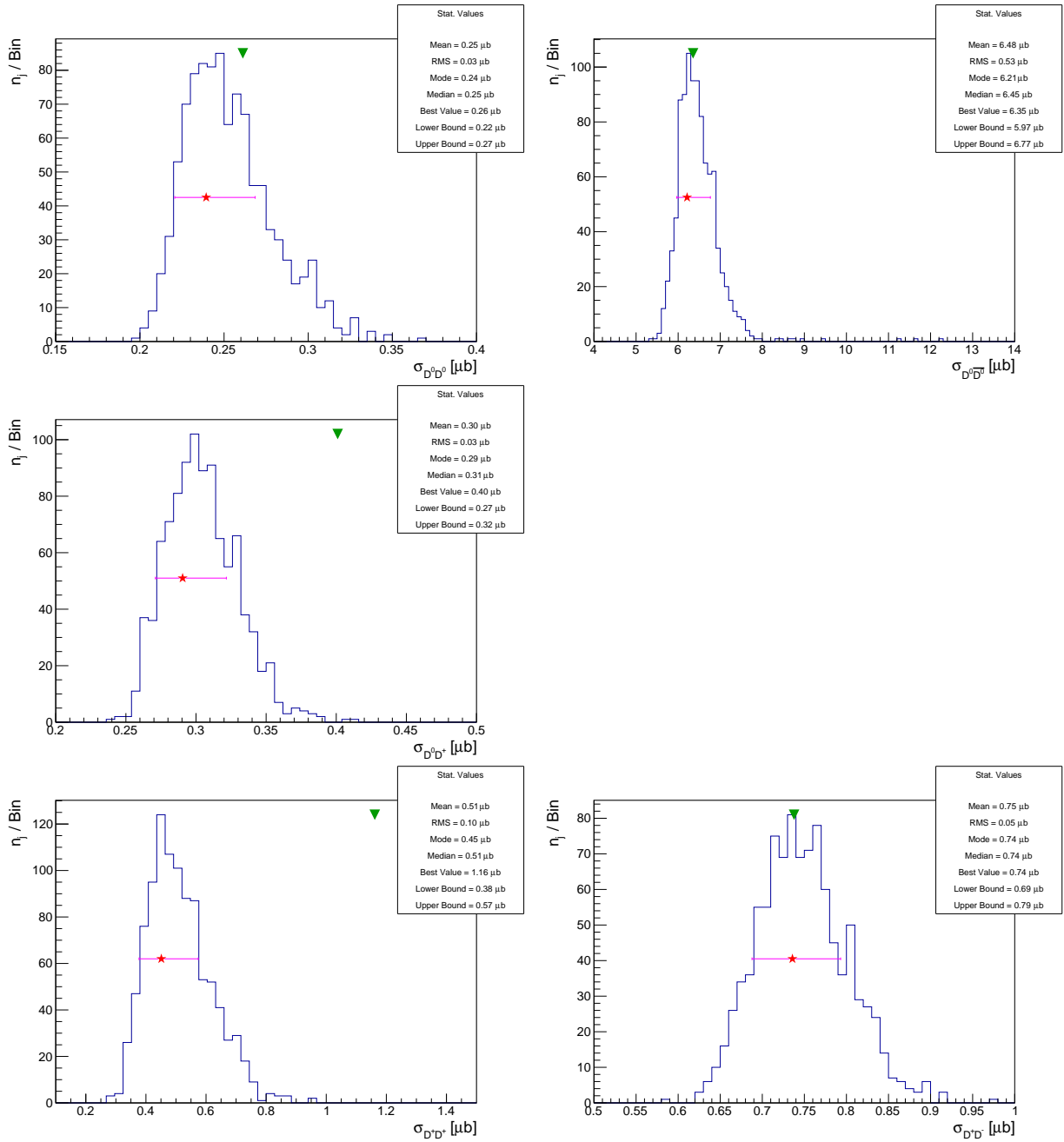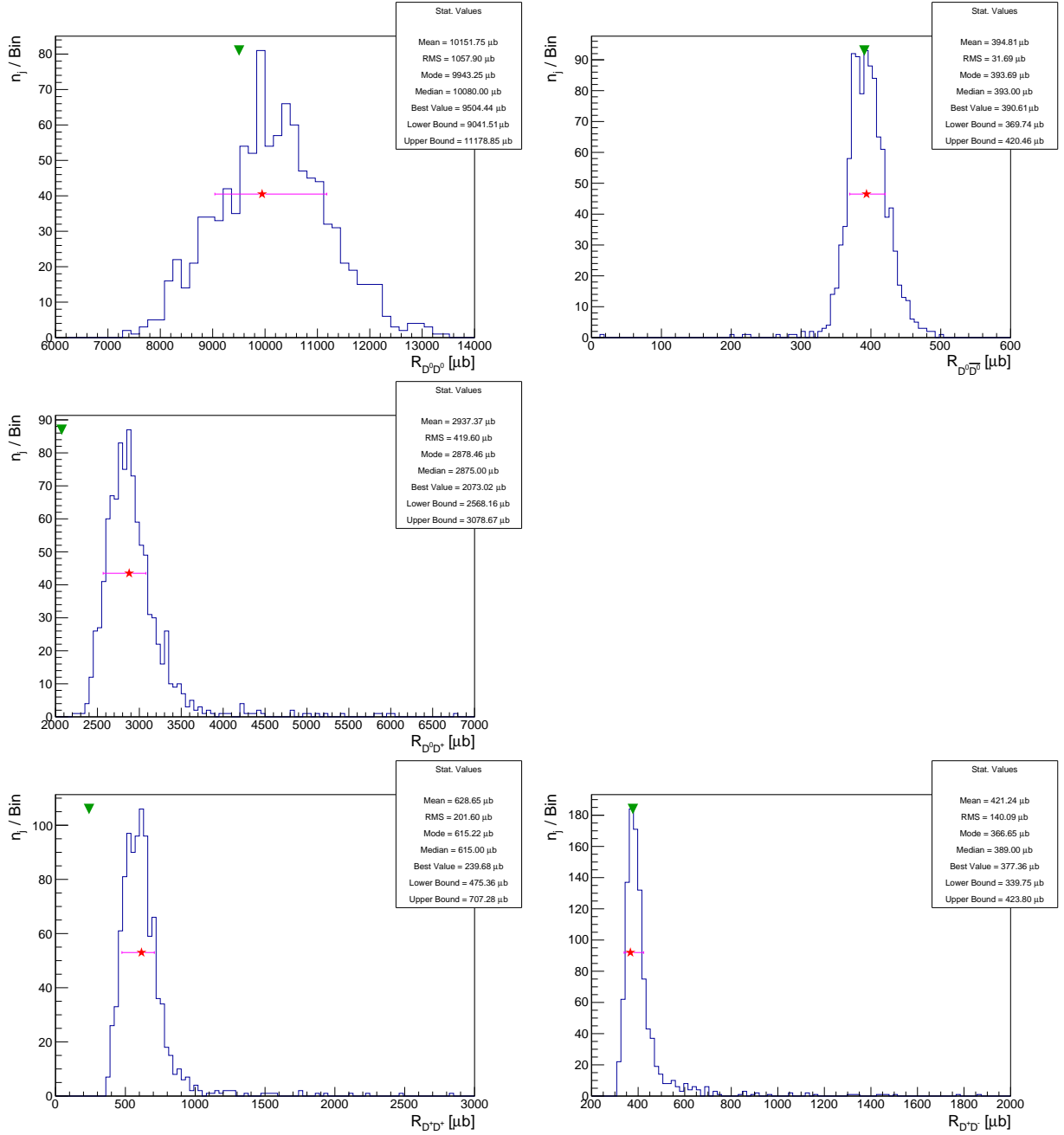
Figure 4.33: Cross section ratio (i.e. R_{CC}) distributions obtained from the toy experiments for the double open charm event candidates $D^0 D^0$ (top left), $D^0 D^+$ (center left), $D^+ D^+$ (bottom left) and for the open charm pair production event candidates $D^0 \bar{D}^0$ (top right) and $D^+ D^-$ (bottom right). No event candidate is observed for the $D^0 D^-$. The mode of a distributions is denoted as $Mode$ and drawn as a red star, while the cross section value calculated by the analysis is denoted as $BestValue$ and drawn as green triangle. The parameters $LowerBound$ and $UpperBound$ correspond to the lower and upper end points of the error bar, drawn in pink. The other statistics parameter calculated from the binned distributions are the mean, median and standard deviation, denoted as $Mean$, $Median$ and RMS.

Figure 4.34: Total efficiency distributions obtained from the toy experiments for the corresponding largest (1st column) and smallest (2nd column) event wise total efficiency for the single open charm event candidates D^0 (1st row) and D^+ (2nd row). The largest and smallest event wise total efficiencies are $\varepsilon_{\text{tot}; D^0, max} = 0.135$, $\varepsilon_{\text{tot}; D^+, max} = 0.141$, $\varepsilon_{\text{tot}; D^0, min} = 2.345 \cdot 10^{-4}$ and $\varepsilon_{\text{tot}; D^+, min} = 1.254 \cdot 10^{-4}$. Please note that the fluctuations are between 0 and 0.7 ‰ in the bottom right distribution.

5 Results

The production cross sections in pp collisions at $\sqrt{s} = 2.76$ TeV and $\mathcal{L} = 3.31$ pb^{-1} for the single open charm event candidates D^0, D$^+$, the double open charm event candidates D^{0}D^0, D^{0}D$^+$, D$^+$D$^+$ and the open charm pair production event candidates $D^0\bar{D}^0$, D^0D^- and D^+D^-, calculated according to equation 4.1, are presented in Tab. 5.1 and in Fig. 5.1. The cross section values are accompanied by their statistic and systematic uncertainties. Tab. 5.2 and Fig. 5.2 show the ratio R_{CC}, which is defined as:

$$R_{CC} := \alpha \, \frac{\sigma_C \, \sigma_C}{\sigma_{CC}}$$

$$\text{where} \qquad \alpha = \begin{cases} 1/4 & D^0D^0 \\ 1/2 & D^0D^+ \\ 1/4 & D^+D^+ \end{cases} , \qquad (5.1)$$

for the corresponding double open charm and open charm pair production event candidates.

Compared to the single open charm production cross sections at $\sqrt{s} = 7$ TeV in [8], the values obtained in this analysis are about a factor of 40 smaller. However, the selections in [8] are very different ($0 < p^T < 8$ GeV). The double open charm and pair production cross sections obtained in this analysis are similar to the values at $\sqrt{s} = 7$ TeV in [2] resp. [3] using slightly harsher cuts, e.g. $3 < p^T < 12$ GeV. As a variation of this analysis, the selection was tightened to ($p^T > 4$ GeV, $y > 2.25$). This leads to about half of the cross sections for single open charm and much less double open charm and open charm pair production cross sections (see Tab. C.1). The DPS model predicts an energy independent σ_{eff} over a vast energy range [14]. However, the obtained cross section ratio $R_{D^0D^0}$ is about a factor of 10 smaller compared to [2] and Tevatron [16]. Due to the reasons explained in chapter 4.9, the systematic uncertainties related to this analysis are not fully reliable. Therefore, no disagreement is claimed.

Candidate	σ_C or σ_{CC} [μb]	Stat.	Syst. Analysis	Syst. $\mathscr{L}$	Syst. B	Syst. Feed-Down.
D^0	49.82	± 0.36	$\pm^{3.71}_{2.31}$	± 1.10	± 0.51	± 0.85
D^+	16.69	± 0.18	$\pm^{1.33}_{1.28}$	± 0.37	± 0.42	± 0.22
$D^0 D^0$	0.26	± 0.16	$\pm^{0.029}_{0.019}$	$\pm 5.8 \cdot 10^{-3}$	$\pm 3.4 \cdot 10^{-3}$	$\pm 8.9 \cdot 10^{-3}$
$D^0 \bar{D}^0$	6.35	± 1.15	$\pm^{0.55}_{0.25}$	± 0.14	± 0.032	± 0.22
$D^0 D^+$	0.40	± 0.26	$\pm^{0.031}_{0.019}$	$8.9 \cdot 10^{-3}$	$7.1 \cdot 10^{-3}$	0.012
$D^0 D^-$	–					
$D^+ D^+$	1.16	± 1.15	$\pm^{0.12}_{0.074}$	± 0.026	± 0.059	0.030
$D^+ D^-$	0.74	± 0.32	$\pm^{0.057}_{0.048}$	± 0.016	± 0.016	± 0.016

Table 5.1: Production cross sections for the single open charm event candidates D^0 and D^+, the double open charm event candidates $D^0 D^0$, $D^0 D^+$ and $D^+ D^+$ and the open charm pair production event candidates $D^0 \bar{D}^0$ and $D^+ D^-$. No event candidate is observed for the $D^0 D^-$. The first uncertainty denotes the statistic uncertainty, the second one denotes the systematic uncertainty related to the analysis, followed by the systematic uncertainties related to the integrated luminosity, branching ratio and feed-down (see chapter 4.9).

Candidate	R_{CC} [mb]	Stat.	Syst. Analysis	Syst. $\mathscr{L}$
$D^0 D^0$	$4 \cdot (2.38$	± 1.50	$\pm^{0.31}_{0.23}$	$3.87 \cdot 10^{-6})$
$D^0 \bar{D}^0$	$4 \cdot (0.098$	± 0.024	$\pm^{6.69}_{5.99} \cdot 10^{-3}$	$1.0 \cdot 10^{-4})$
$D^0 D^+$	$2 \cdot (1.04$	± 0.67	$\pm^{0.20}_{0.16}$	$1.77 \cdot 10^{-5})$
$D^0 D^-$	$-$			
$D^+ D^+$	$4 \cdot (0.060$	± 0.060	$\pm^{0.023}_{0.035}$	$5.43 \cdot 10^{-5})$
$D^+ D^-$	$4 \cdot (0.094$	± 0.041	$\pm^{14.29}_{6.72} \cdot 10{-3}$	$3.33 \cdot 10^{-5})$

Table 5.2: Production cross section ratio $R_{CC} = \alpha \ \frac{\sigma_C \sigma_C}{\sigma_{CC}}$, where $C \in \{D^0, D^+\}$ for the double open charm event candidates $D^0 D^0$, $D^0 D^+$ and $D^+ D^+$ and the open charm pair production event candidates $D^0 \bar{D}^0$ and $D^+ D^-$. No event candidate is observed for the $D^0 D^-$. The first uncertainty denotes the statistic uncertainty, the second one denotes the systematic uncertainty related to the analysis (see chapter 4.9).
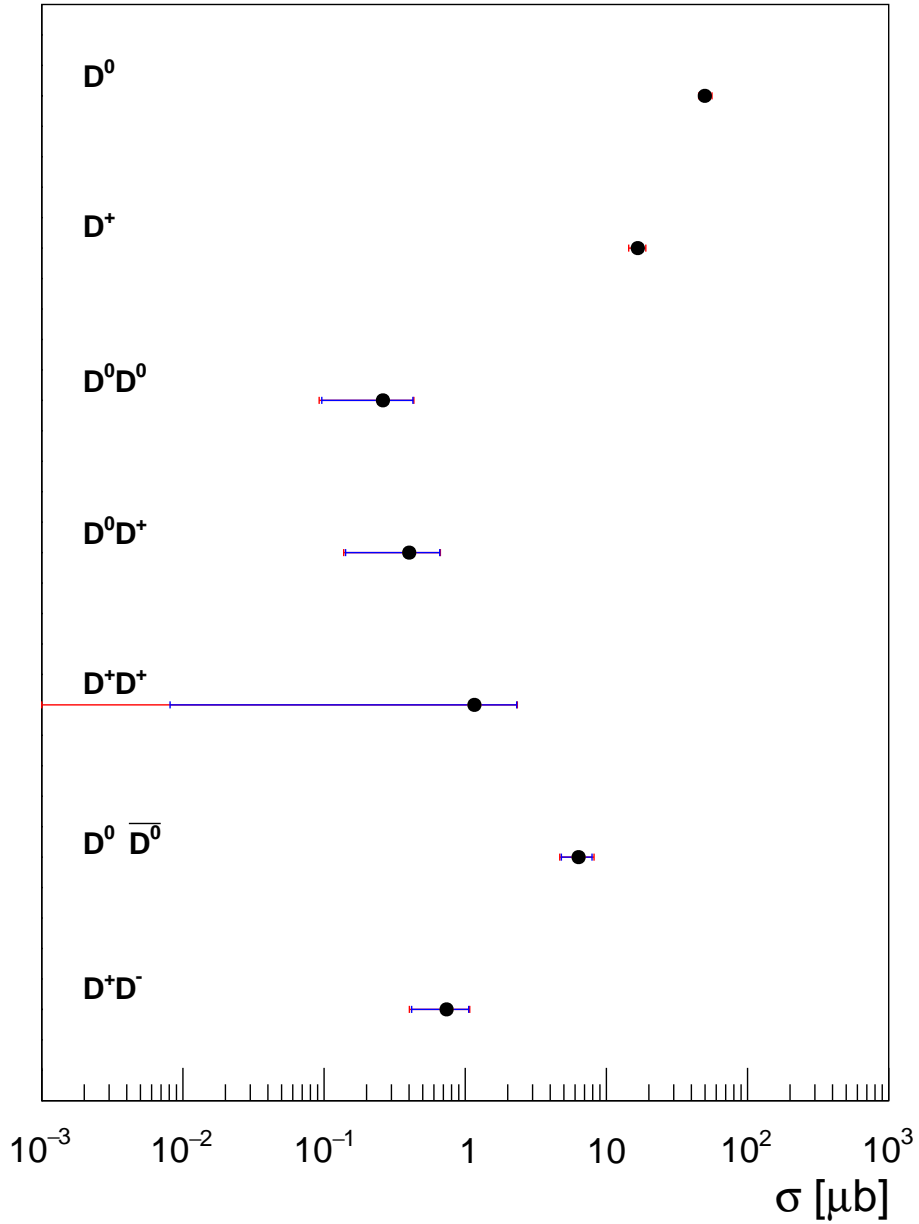
Figure 5.1: Production cross sections σ_C and σ_{CC}, where $C \in \{D^0, D^+\}$ (points with error bars). The blue errorbars denote the statistic uncertainties, the red errorbars the sum of the statistic and systematic uncertainties (see chapter 4.9). No event candidate is observed for the $D^0 D^-$.
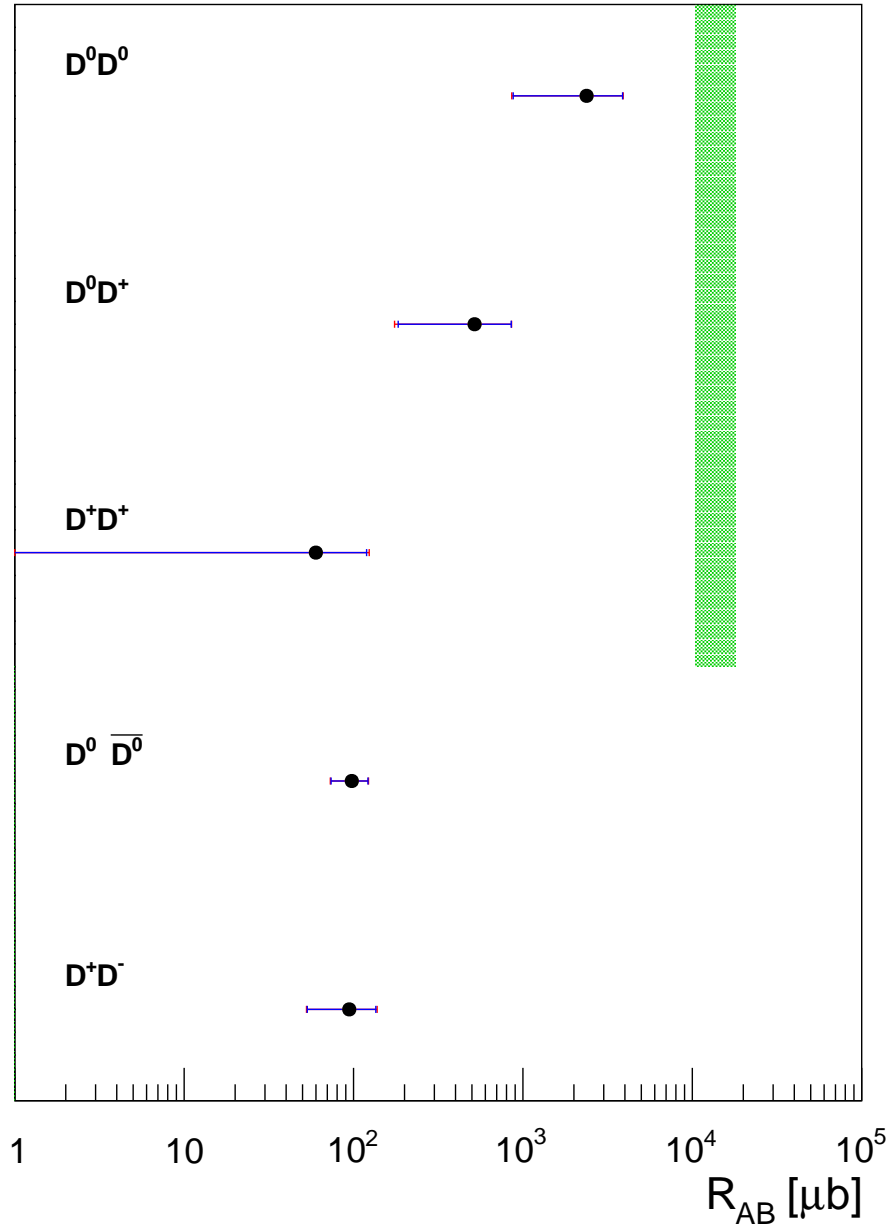
Figure 5.2: Production cross section ratios $R_{CC} := \alpha \, \frac{\sigma_C \, \sigma_C}{\sigma_{CC}}$, where $C \in \{D^0, D^+\}$ (points with error bars) in comparison with the measured effective cross section at Tevatron for multi-jet events (green dotted). The blue errorbars denote the statistic uncertainties, the red errorbars the sum of the statistic and systematic uncertainties. No event candidate is observed for the $D^0 D^-$.

6 Conclusion and Outlook

The production of single and double open charm mesons have been seen in pp collisions at $\sqrt{s} = 2.26$ TeV. The signals are clearly visible in the mass distributions for the modes D^0, D^+ and $D^0 D^0$ but less obvious for the double open charm modes involving D^+. A quantitative determination of the statistical significance was not performed. Nevertheless, this analysis reuses techniques from previous analyses, that produced significant observations [2], [28].

Based on this signal, a cross section measurement is attempted. For each class of reconstructed candidates a cross section could be calculated and fully corrected for reconstruction, tracking, particle identification, luminosity and branching ratio. However, a precise determination of the double open charm and pair production cross sections was not possible due to few candidates. The integrated luminosity needs to be increased to be able to do so. Moreover, the low and probably unprecisely determined charm trigger efficiency does not allow a precision measurement. In the LHCb collaboration, this is known to be a difficult problem.

Alternatively, a random trigger can be used especially for the D^0 and D^+ modes due to their large cross section. For the double open charm production, asymmetric selections may be feasible. Those would avoid using the charm trigger at low (p^T, y), still allowing the second charm meson to pass the selection. Also, data from 2012 taken at 8 TeV using the same trigger can be utilized. Combined with available random triggers, this might help to improve the precision. For this work, this was not possible due to time constraints.

A Invariant Mass Fit Parameters

The fit parameters of the unbinned maximum likelihood fit to the invariant mass distributions M_C, where $C \in \{D^0, D^+\}$ for the Gaussian, Bukin and Double Crystal Ball models are listed in Tab. A.1, A.2, A.3, respectively.

The fit parameters of the unbinned maximum likelihood fit to the invariant mass distributions M_{CC}, where $CC \in \{D^0 D^0 \cup D^0 \bar{D}^0, D^0 D^+ \cup D^0 D^-, D^+ D^+ \cup D^+ D^-\}$ for the Gaussian, Bukin and Double Crystal Ball models are listed in Tab. A.1, A.2, A.3, respectively.

Fit Parameter	D^0	D^+
μ [GeV]	$1.866 \pm 2.9 \cdot 10^{-5}$	$1.871 \pm 3.6 \cdot 10^{-5}$
σ [GeV]	$(8.054 \pm 0.024) \cdot 10^{-3}$	$(7.949 \pm 0.031) \cdot 10^{-3}$
N_S	91006.7 ± 313.7	56141.3 ± 247.2
τ	-13.969 ± 0.552	-13.022 ± 0.706
N_B	5433.9 ± 113.4	3567.0 ± 92.4

Table A.1: Fit parameters of the unbinned maximum likelihood fit to the invariant mass distributions for the single open charm event candidates D^0, D^+, M_{D^0}, M_{D^+}, using the Gaussian model.

Fit Parameter	D^0	D^+
μ [GeV]	$1.867 \pm 3.1 \cdot 10^{-5}$	$1.871 \pm 7.1 \cdot 10^{-5}$
σ [GeV]	$(7.369 \pm 0.028) \cdot 10^{-3}$	$(7.293 \pm 0.027) \cdot 10^{-3}$
ξ	$(-2.515 \pm 0.122) \cdot 10^{-3}$	$(-5.561 \pm 4.490) \cdot 10^{-3}$
ρ_l	-0.155 ± 0.012	-0.137 ± 0.001
ρ_r	-0.232 ± 0.010	-0.232 ± 0.003
N_S	92469.9 ± 308.5	57328.9 ± 242.4
τ	-14.919 ± 0.919	-14.706 ± 1.220
N_B	3915.4 ± 141.7	2201.7 ± 106.2

Table A.2: Fit parameters of the unbinned maximum likelihood fit to the invariant mass distributions for the single open charm event candidates D^0, D^+, M_{D^0}, M_{D^+}, using the Bukin model.

Fit Parameter	D^0	D^+
μ [GeV]	$1.866 \pm 3.3 \cdot 10^{-5}$	$1.871 \pm 4.1 \cdot 10^{-5}$
σ [GeV]	$(7.618 \pm 0.035) \cdot 10^{-3}$	$(7.262 \pm 0.048) \cdot 10^{-3}$
α_l	1.339 ± 0.047	0.946 ± 0.051
α_r	-1.259 ± 0.072	-1.321 ± 0.047
n_l	65.098 ± 42.820	98.559 ± 0.306
n_r	138.020 ± 0.217	146.362 ± 85.789
r	0.638 ± 0.060	0.407 ± 0.049
N_S	92638.6 ± 309.3	57588.3 ± 243.7
τ	-14.919 ± 0.919	-14.706 ± 1.220
N_B	3915.4 ± 141.7	2201.7 ± 106.2

Table A.3: Fit parameters of the unbinned maximum likelihood fit to the invariant mass distributions for the single open charm event candidates D^0, D^+, M_{D^0}, M_{D^+}, using the Double Crystal Ball model.

Fit Parameter	$D^0 D^0 \cup D^0 \bar{D}^0$	$D^0 D^+ \cup D^0 D^-$	$D^+ D^+ \cup D^+ D^-$
μ_{S_1} [GeV]	$1.866 \pm 2.8 \cdot 10^{-5}$	$1.866 \pm 2.8 \cdot 10^{-5}$	$1.871 \pm 3.6 \cdot 10^{-5}$
μ_{S_2} [GeV]	$1.866 \pm 2.8 \cdot 10^{-5}$	$1.871 \pm 3.6 \cdot 10^{-5}$	$1.871 \pm 3.6 \cdot 10^{-5}$
σ_{S_1} [GeV]	$(8.054 \pm 0.024) \cdot 10^{-3}$	$(8.054 \pm 0.024) \cdot 10^{-3}$	$(7.949 \pm 0.031) \cdot 10^{-3}$
σ_{S_2} [GeV]	$(8.054 \pm 0.024) \cdot 10^{-3}$	$(7.949 \pm 0.031) \cdot 10^{-3}$	$(7.949 \pm 0.031) \cdot 10^{-3}$
$N_{S_1 S_2}$	74.9 ± 9.3	8.5 ± 3.6	41.4 ± 7.3
$\tau_{B_1,c}$	4.766 ± 237	-7.674 ± 190	16.690 ± 24.01
$\tau_{B_2,c}$	4.766 ± 237	-57.696 ± 201	16.690 ± 24.01
τ_{B_1}	-12.824 ± 10.940	-5.770 ± 34.863	1.745 ± 14.0
τ_{B_2}	-12.824 ± 10.940	-44.244 ± 63.129	1.745 ± 14.0
$N_{B_1 B_2}$	$2.2 \cdot 10^{-6} \pm 1.1$	$6.3 \cdot 10^{-6} \pm 0.8$	1.4 ± 1.7
$N_{S_1 B_2}$	5.9 ± 3.3	1.2 ± 1.3	5.1 ± 3.3
$N_{S_2 B_1}$	6.3 ± 3.7	1.3 ± 2.3	3.1 ± 3.3

Table A.4: Fit parameters of the unbinned maximum likelihood fit to the invariant mass distributions for the double open charm event candidates (including open charm pair production) $D^0 D^0 \cup D^0 \bar{D}^0$, $D^0 D^+ \cup D^0 D^-$ and $D^+ D^+ \cup D^+ D^-$, $M_{D^0 D^0}$, $M_{D^0 D^+}$ and $M_{D^+ D^+}$, using the Gaussian model.

Fit Parameter	$D^0 D^0 \cup D^0 \bar{D}^0$	$D^0 D^+ \cup D^0 D^-$	$D^+ D^+ \cup D^+ D^-$
μ_{S_1} [GeV]	$1.867 \pm 3.1 \cdot 10^{-5}$	$1.867 \pm 3.1 \cdot 10^{-5}$	$1.871 \pm 7.1 \cdot 10^{-5}$
μ_{S_2} [GeV]	$1.867 \pm 3.1 \cdot 10^{-5}$	$1.871 \pm 7.1 \cdot 10^{-5}$	$1.871 \pm 7.1 \cdot 10^{-5}$
σ_{S_1} [GeV]	$(7.369 \pm 0.028) \cdot 10^{-3}$	$(7.369 \pm 0.028) \cdot 10^{-3}$	$(7.293 \pm 0.027) \cdot 10^{-3}$
σ_{S_2} [GeV]	$(7.369 \pm 0.028) \cdot 10^{-3}$	$(7.293 \pm 0.027) \cdot 10^{-3}$	$(7.293 \pm 0.027) \cdot 10^{-3}$
ξ_{S_1}	$(-2.515 \pm 0.122) \cdot 10^{-3}$	$(-2.515 \pm 0.122) \cdot 10^{-3}$	$(-5.561 \pm 4.490) \cdot 10^{-3}$
ξ_{S_2}	$(-2.515 \pm 0.122) \cdot 10^{-3}$	$(-5.561 \pm 4.490) \cdot 10^{-3}$	$(-5.561 \pm 4.490) \cdot 10^{-3}$
$\rho_{l; S_1}$	-0.155 ± 0.012	-0.155 ± 0.012	-0.137 ± 0.001
$\rho_{l; S_2}$	-0.155 ± 0.012	-0.137 ± 0.001	-0.137 ± 0.001
$\rho_{r; S_1}$	-0.232 ± 0.010	-0.232 ± 0.010	-0.232 ± 0.003
$\rho_{r; S_2}$	-0.232 ± 0.010	-0.232 ± 0.003	-0.232 ± 0.003
$N_{S_1 S_2}$	78.1 ± 7.4	9.4 ± 3.7	44.3 ± 7.8
$\tau_{B_1, c}$	-4.949 ± 245	-8.849 ± 173	1.227 ± 23.517
$\tau_{B_2, c}$	-4.949 ± 245	-16.848 ± 157	1.227 ± 23.517
τ_{B_1}	-8.437 ± 10.437	-4.961 ± 65.092	2.518 ± 20.798
τ_{B_2}	-8.437 ± 10.437	-4.422 ± 61.592	2.518 ± 20.798
$N_{B_1 B_2}$	$2.7 \cdot 10^{-6} \pm 183.0$	$1.3 \cdot 10^{-6} \pm 190.2$	1.4 ± 1.9
$N_{S_1 B_2}$	4.0 ± 2.5	1.2 ± 1.2	4.3 ± 3.1
$N_{S_2 B_1}$	4.9 ± 2.7	0.4 ± 3.4	0.9 ± 5.0

Table A.5: Fit parameters of the unbinned maximum likelihood fit to the invariant mass distributions for the double open charm event candidates (including open charm pair production) $D^0 D^0 \cup D^0 \bar{D}^0$, $D^0 D^+ \cup D^0 D^-$ and $D^+ D^+ \cup D^+ D^-$, $M_{D^0 D^0}$, $M_{D^0 D^+}$ and $M_{D^+ D^+}$, using the Bukin model.

Fit Parameter	D^0D^0 & $D^0\bar{D}^0$	D^0D^+ & D^0D^-	D^+D^+ & D^+D^-
μ_{S_1} [GeV]	$1.866 \pm 3.3 \cdot 10^{-5}$	$1.866 \pm 3.3 \cdot 10^{-5}$	$1.871 \pm 4.1 \cdot 10^{-5}$
μ_{S_2} [GeV]	$1.866 \pm 3.3 \cdot 10^{-5}$	$1.871 \pm 4.1 \cdot 10^{-5}$	$1.871 \pm 4.1 \cdot 10^{-5}$
σ_{S_1} [GeV]	$(7.618 \pm 0.035) \cdot 10^{-3}$	$(7.618 \pm 0.035) \cdot 10^{-3}$	$(7.262 \pm 0.048) \cdot 10^{-3}$
σ_{S_2} [GeV]	$(7.618 \pm 0.035) \cdot 10^{-3}$	$(7.262 \pm 0.048) \cdot 10^{-3}$	$(7.262 \pm 0.048) \cdot 10^{-3}$
$\alpha_{l;S_1}$	1.339 ± 0.047	1.339 ± 0.047	0.946 ± 0.051
$\alpha_{l;S_2}$	1.339 ± 0.047	0.946 ± 0.051	0.946 ± 0.051
$\alpha_{r;S_1}$	-1.259 ± 0.072	-1.259 ± 0.072	-1.321 ± 0.047
$\alpha_{l;S_2}$	-1.259 ± 0.072	-1.321 ± 0.047	-1.321 ± 0.047
$n_{l;S_1}$	65.098 ± 42.820	65.098 ± 42.820	98.559 ± 0.306
$n_{l;S_2}$	65.098 ± 42.820	98.559 ± 0.306	98.559 ± 0.306
$n_{r;S_1}$	138.020 ± 0.217	138.020 ± 0.217	146.362 ± 85.789
$n_{r;S_2}$	138.020 ± 0.217	146.362 ± 85.789	146.362 ± 85.789
r_{S_1}	0.638 ± 0.058	0.638 ± 0.058	0.407 ± 0.049
r_{S_2}	0.638 ± 0.058	0.407 ± 0.049	0.407 ± 0.049
$N_{S_1 S_2}$	78.7 ± 8.1	9.3 ± 3.9	44.5 ± 7.9
$\tau_{B_1,c}$	-5.739 ± 180	-8.841 ± 203	1.217 ± 23.211
$\tau_{B_2,c}$	-5.739 ± 180	-15.217 ± 228	1.217 ± 23.211
τ_{B_1}	-9.302 ± 12.2	-5.020 ± 50.084	3.709 ± 24.155
τ_{B_2}	-9.302 ± 12.2	-42.474 ± 65.470	3.709 ± 24.155
$N_{B_1 B_2}$	$1.0 \cdot 10^{-6} \pm 199.8$	$3.3 \cdot 10^{-6} \pm 1.3$	1.5 ± 2.0
$N_{S_1 B_2}$	3.8 ± 2.8	1.1 ± 1.3	4.0 ± 3.2
$N_{S_2 B_1}$	4.5 ± 3.0	0.6 ± 2.4	0.6 ± 8.8

Table A.6: Fit parameters of the unbinned maximum likelihood fit to the invariant mass distributions for the double open charm event candidates (including open charm pair production) $D^0D^0 \cup D^0\bar{D}^0$, $D^0D^+ \cup D^0D^-$ and $D^+D^+ \cup D^+D^-$, $M_{D^0D^0}$, $M_{D^0D^+}$ and $M_{D^+D^+}$, using the Double Crystal Ball model.

B GEC Efficiency Fit Parameters

The fit parameters of the unbinned maximum likelihood fit to the N_{SPD} distributions using the Double Gamma model G for the single open charm event candidates D^0 and D^+ and double open charm event candidates (including open charm pair produciton) $D^0 D^0 \cup D^0 \bar{D}^0$, $D^0 D^+ \cup D^0 D^-$ and $D^+ D^+ \cup D^+ D^-$ are presented in Tab. B.1 and B.2, respectively.

Fit Parameter	D^0	D^+
μ_1	-353.32 ± 3.14	-334.95 ± 4.03
γ_1	68.665 ± 0.51	67.07 ± 0.63
β_1	7.02 ± 0.48	6.93 ± 0.06
n_1	89970.0 ± 915.9	55868.0 ± 664.9
μ_2	59.93 ± 11.50	101.21 ± 13.19
γ_2	7.926 ± 0.54	5.69 ± 0.57
β_2	24.97 ± 0.89	27.64 ± 1.35
n_2	9179.3 ± 884.8	5431.6 ± 627.0

Table B.1: Fit parameters of the unbinned maximum likelihood fit to the N_{SPD} distributions using the Double Gamma model G for the single open charm event candidates D^0 and D^+.

Fit Parameter	$D^0 D^0 \cup D^0 \bar{D}^0$	$D^0 D^+ \cup D^0 D^-$	$D^+ D^+ \cup D^+ D^-$
μ	15.77 ± 62.40	$-1.63 \cdot 10^{-3} \pm 137$	-10.57 ± 192
γ	4.64 ± 4.15	1.10 ± 4.89	5.74 ± 12.10
β	29.34 ± 13.90	16.79 ± 7.62	27.07 ± 2.86
n	86.0 ± 9.3	10.0 ± 3.2	51.0 ± 7.1

Table B.2: Fit parameters of the unbinned maximum likelihood fit to the N_{SPD} distributions using the Single Gamma model g for the double open charm event candidates (including open charm pair production) $D^0 D^0 \cup D^0 \bar{D}^0$, $D^0 D^+ \cup D^0 D^-$ and $D^+ D^+ \cup D^+ D^-$.

The fit parameters of the unbinned maximum likelihood fit to the N_{SPD} distributions using the Single Gamma and Beta models for the single open charm event candidates D^0 and D^+ are presented in Tab. B.3 and B.4, respectively. For the Beta model a stretched Beta PDF with a special representation for the mean μ and mode ν is used:

$$B(x; a, b) \;=\; n \, \frac{x}{c} \, \left(\frac{x}{c} \right)^{-c\mu + 2\frac{\mu\nu}{c(\nu-\mu)} - 1} \; \left(1 - \frac{x}{c} \right)^{(-c\mu + 2\frac{\mu\nu}{c(\nu-\mu)} - 1)(\frac{c}{\mu} - 1) - 1} \qquad ,$$

x : observable, i.e. N_{SPD} for the single open charm event candidates $\qquad$ (B.1)

$\mu > 0, \nu > 0$: mean and mode of the Beta PDF

n, c : normalization factors $\quad$.

Fit Parameter	D^0	D^+
μ	-8.16 ± 2.81	-9.68 ± 3.93
γ	5.36 ± 0.17	5.70 ± 0.26
β	28.72 ± 0.46	27.20 ± 0.61
n	96095.6 ± 361.3	59613.6 ± 282.8

Table B.3: Fit parameters of the unbinned maximum likelihood fit to the N_{SPD} distributions using the Single Gamma model for the single open charm event candidates D^0 and D^+.

Fit Parameter	D^0	D^+
μ	146.58 ± 0.23	145.11 ± 0.31
ν	116.85 ± 0.29	118.29 ± 0.40
a	4.93 ± 0.722	4.14 ± 0.06
b	$(2.16 \pm 1.68) \cdot 10^7$	24.61 ± 1.76
n	95506 ± 318	59878 ± 258

Table B.4: Fit parameters of the unbinned maximum likelihood fit to the N_{SPD} distributions using the Beta model for the single open charm event candidates D^0 and D^+.

C Analysis for additionally applied $(p^T \, [\textbf{GeV}], y) > (4, 2.25)$

The results of the analysis corresponding to the additionally applied cuts on $p^T > 4$ GeV, $y > 2.25$ are presented in the following sections. These cuts are introduced in order to exclude event candidates lying below a certain efficiency threshold (see chapter 4.6). All given illustrations are to read in the same way as the corresponding ones in the original analysis.

C.1 Results

Candidate	R_{CC} [mb]	Stat.	Syst. Analysis	Syst. $\mathscr{L}$
$D^0 D^0$	$4 \cdot (1.48$	± 0.72	$\pm^{0.15}_{0.039}$	$1.27 \cdot 10^{-6})$
$D^0 \bar{D}^0$	$4 \cdot (0.25$	± 0.063	$\pm^{0.022}_{0.024}$	$7.49 \cdot 10^{-6})$
$D^0 D^+$	$2 \cdot (1.33$	± 1.05	$\pm^{0.15}_{0.029}$	$2.83 \cdot 10^{-6})$
$D^0 D^-$	$-$			
$D^+ D^+$	$4 \cdot (6.03$	± 6.03	$\pm^{0.82}_{0.30}$	$1.33 \cdot 10^{-7})$
$D^+ D^-$	$4 \cdot (0.20$	± 0.049	$\pm^{25.49}_{8.91} \cdot 10^{-3}$	$3.95 \cdot 10^{-6})$

Table C.2: Production cross section ratio R_{CC}, where $C \in \{D^0, D^+\}$ for the double open charm event candidates $D^0 D^0$, $D^0 D^+$ and $D^+ D^+$ and the open charm pair production event candidates $D^0 \bar{D}^0$ and $D^+ D^-$. No event candidate is observed for the $D^0 D^-$. The first uncertainty denotes the statistic uncertainty, the second the systematic uncertainty related to the analysis (see chapter 4.9).

Candidate	σ_C or σ_{CC} [μb]	Stat.	Syst. Analysis	Syst. $\mathscr{L}$	Syst. B	Syst. Feed-Down.
D^0	19.94	± 0.09	$\pm^{1.30}_{0.82}$	± 0.44	± 0.20	± 0.34
D^+	8.52	± 0.06	$\pm^{0.64}_{0.51}$	± 0.19	± 0.22	± 0.11
$D^0 D^0$	0.0671	± 0.0327	$\pm^{3.20}_{3.58} \cdot 10^{-3}$	$1.48 \cdot 10^{-3}$	$6.68 \cdot 10^{-4}$	$2.28 \cdot 10^{-3}$
$D^0 \bar{D}^0$	0.3961	± 0.0998	$\pm^{0.032}_{0.032}$	$8.75 \cdot 10^{-3}$	$2.03 \cdot 10^{-3}$	0.013
$D^0 D^+$	0.0640	± 0.0508	$\pm^{3.71}_{2.58} \cdot 10^{-3}$	$1.41 \cdot 10^{-3}$	$1.39 \cdot 10^{-3}$	$1.92 \cdot 10^{-3}$
$D^0 D^-$	—					
$D^+ D^+$	$3.0 \cdot 10^{-3}$	$\pm 3.0 \cdot 10^{-3}$	$\pm^{2.47}_{1.16} \cdot 10^{-4}$	$6.65 \cdot 10^{-5}$	$1.52 \cdot 10^{-4}$	$7.82 \cdot 10^{-5}$
$D^+ D^-$	0.0892	± 0.0216	$\pm^{4.72}_{4.96} \cdot 10^{-3}$	$1.97 \cdot 10^{-3}$	$1.09 \cdot 10^{-3}$	$2.32 \cdot 10^{-3}$

Table C.1: Production cross sections for the single open charm event candidates D^0 and D^+, the double open charm event candidates $D^0 D^0$, $D^0 D^+$ and $D^+ D^+$ and the open charm pair production event candidates $D^0 \bar{D}^0$ and $D^+ D^-$. No event candidate is observed for the $D^0 D^-$. The first uncertainty denotes the statistic uncertainty, the second the systematic uncertainty related to the analysis (see chapter 4.9), followed by the systematic uncertainties related to the integrated luminosity, branching ratio and feed-down.
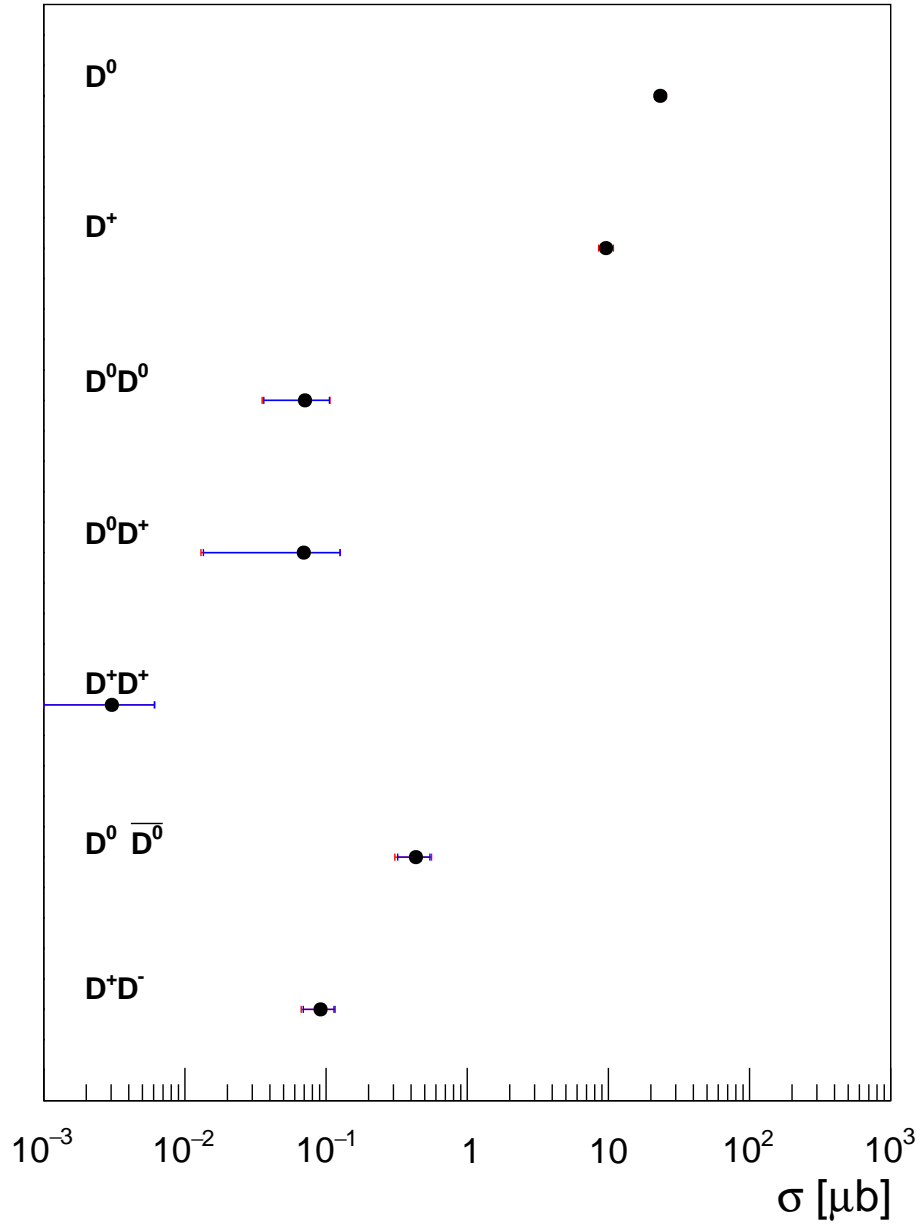
Figure C.1: Production cross sections σ_C and σ_{CC}, where $C \in \{D^0, D^+\}$ (points with error bars). The blue errorbars denote the statistic uncertainties, the red errorbars the sum the statistic and systematic uncertainties (see chapter 4.9). No event candidate is observed for the $D^0 D^-$.
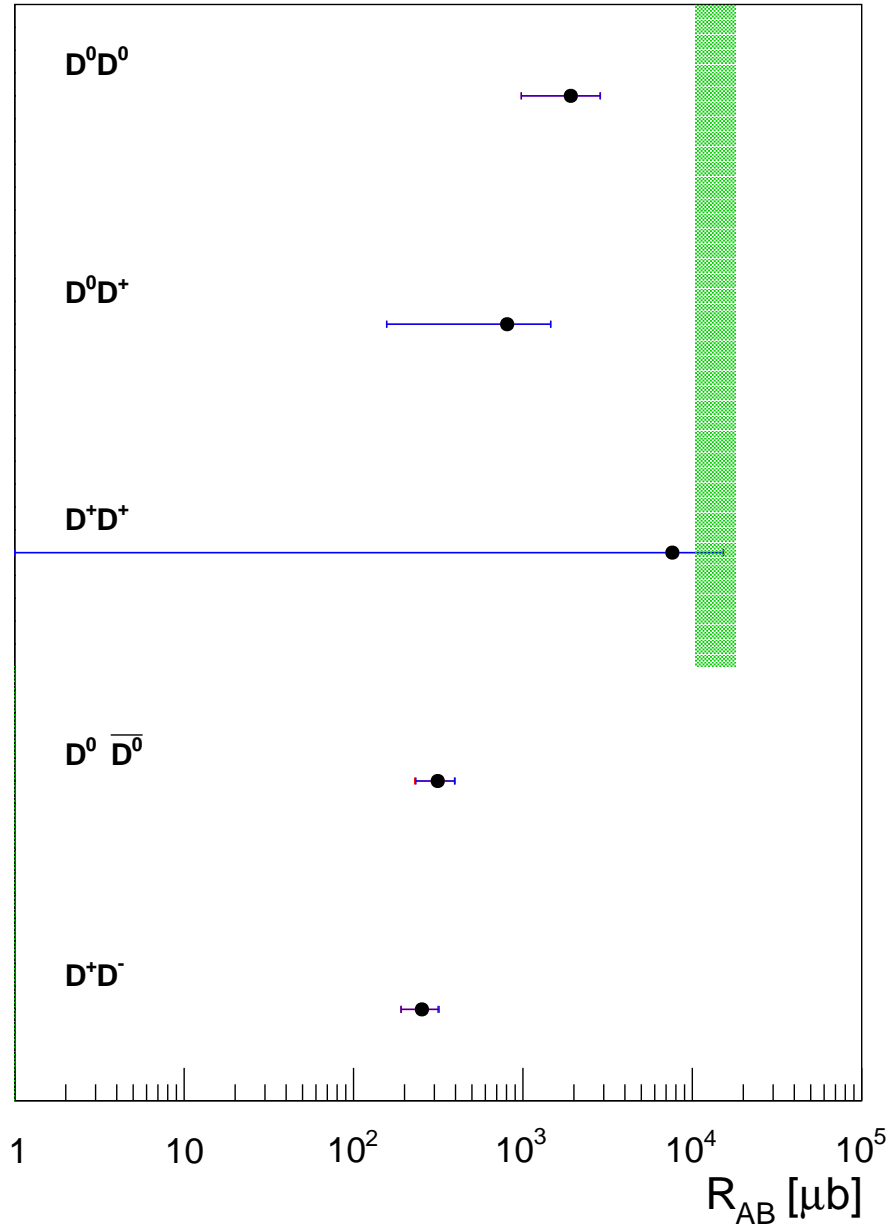
Figure C.2: Production cross section ratios $R_{CC} := \alpha \, \frac{\sigma_C \, \sigma_C}{\sigma_{CC}}$, where $C \in \{D^0, D^+\}$ (points with error bars) in comparison with the measured effective cross section at Tevatron for multi-jet events (green dotted). The blue errorbars denote the statistic uncertainties, the red errorbars the sum of the statistic and systematic uncertainties (see chapter 4.9). No event candidate is observed for the $D^0 D^-$

C.2 Systematic Uncertainties
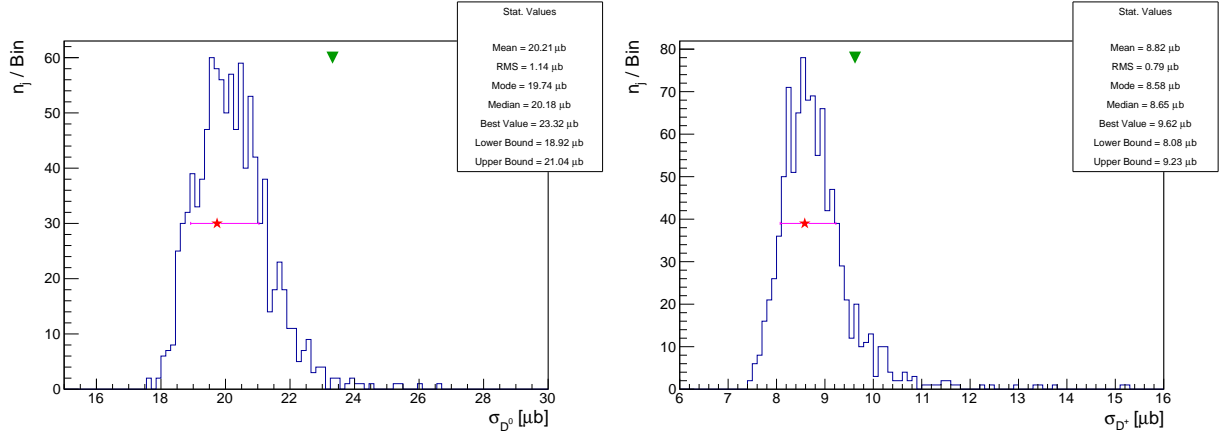
Figure C.3: Cross section distributions obtained from the toy experiments for the single open charm event candidates D^0 (left) and D^+ (right). The mode of a distributions is denoted as $Mode$ and drawn as a red star, while the cross section value calculated by the analysis is denoted as $BestValue$ and drawn as green triangle. The parameters $LowerBound$ and $UpperBound$ correspond to the lower and upper end points of the error bar, drawn in pink. The other statistics parameter calculated from the binned distributions are the mean, median and standard deviation, denoted as $Mean$, $Median$ and RMS.

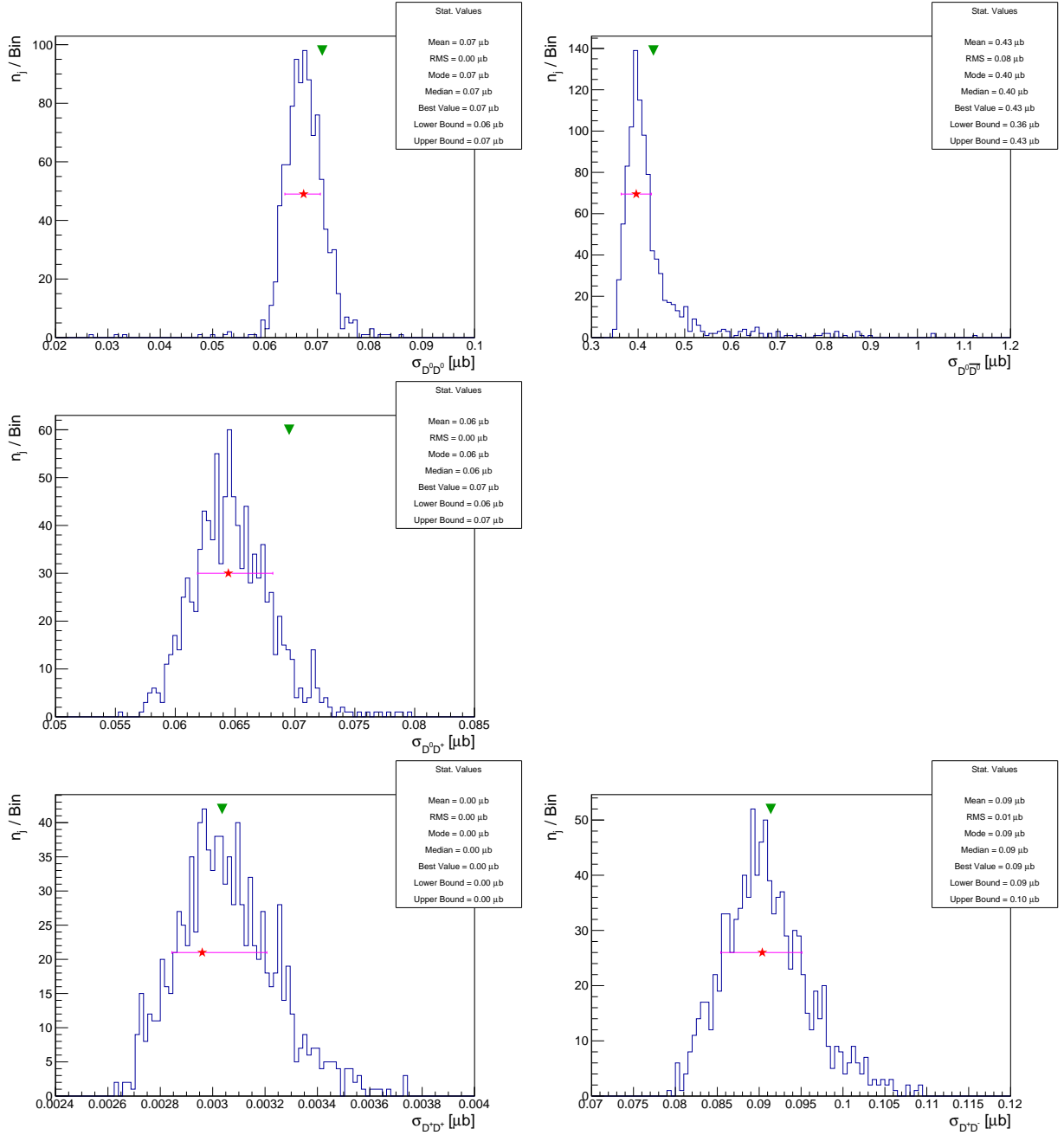Figure C.4: Cross section distributions obtained from the toy experiments for the double open charm event candidates D^0D^0 (top left), D^0D^+ (center left), D^+D^+ (bottom left) and for the open charm pair production event candidates $D^0\bar{D}^0$ (top right) and D^+D^- (bottom right). No event candidate is observed for the D^0D^-. The mode of a distributions is denoted as $Mode$ and drawn as a red star, while the cross section value calculated by the analysis is denoted as $BestValue$ and drawn as green triangle. The parameters $LowerBound$ and $UpperBound$ correspond to the lower and upper end points of the error bar, drawn in pink. The other statistics parameter calculated from the binned distributions are the mean, median and standard deviation, denoted as $Mean$, $Median$ and RMS.
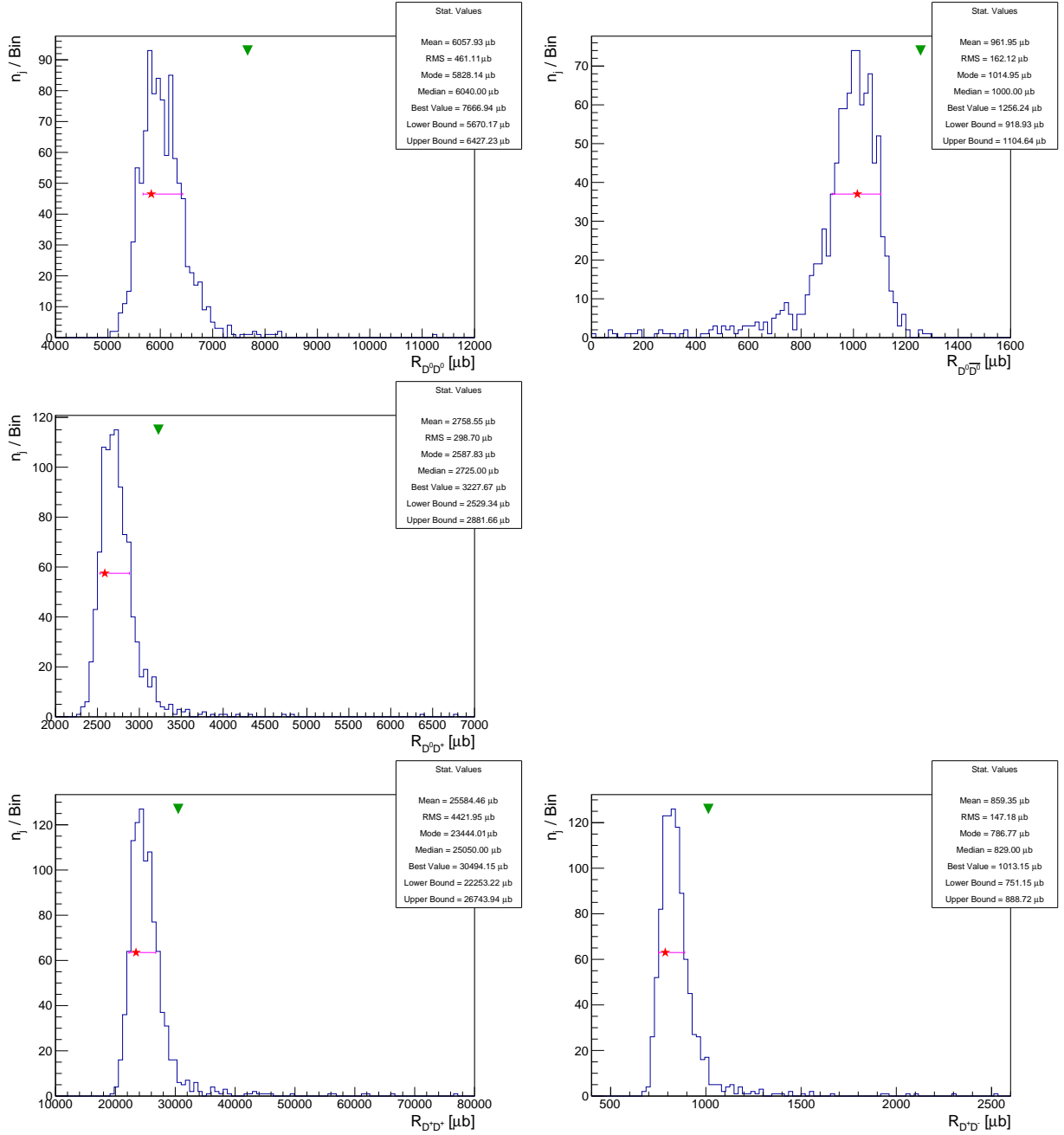
Figure C.5: Cross section ratio (i.e. R_{CC}) distributions obtained from the toy experiments for the double open charm event candidates $D^0 D^0$ (top left), $D^0 D^+$ (center left), $D^+ D^+$ (bottom left) and for the open charm pair production event candidates $D^0 \bar{D}^0$ (top right) and $D^+ D^-$ (bottom right). No event candidate is observed for the $D^0 D^-$. The mode of a distributions is denoted as $Mode$ and drawn as a red star, while the cross section value calculated by the analysis is denoted as $Best\,Value$ and drawn as green triangle. The parameters $Lower\,Bound$ and $Upper\,Bound$ correspond to the lower and upper end points of the error bar, drawn in pink. The other statistics parameter calculated from the binned distributions are the mean, median and standard deviation, denoted as $Mean$, $Median$ and RMS.

References

[1] R. Maciula and A. Szczurek, *Production of $c\bar{c}c\bar{c}$ in single and double parton scattering in collinear and kt-factorization approaches*, PoS EPS-HEP2015 (2015) 500.

[2] The LHCb Collaboration, R. Aaij et al., *Observation of double charm production involving open charm in pp collisions at $\sqrt{s} = 7$ TeV*, JHEP 06 (2012) 141 Addendum ibid. 03 (2014) 108, arXiv:1205.0975.

[3] A. Artamonov, V. Belyaev, V. Egorychev, D. Golubkov, J. He, A. Kozlinskiy, M. Needham, A. Novoselov and V. Romanovskiy, *Observation of J/ψ, open charm and double open charm production in pp collisions at $\sqrt{s} = 7$ TeV*, LHCB-ANA-2011-067.

[4] M. Peskin and D. Schröder, *An Introduction to Quantum Field Theory*, Advanced Book Program (ABP), Westview Press, Boulder, Colorado, October 1995.

[5] S. Weinberg, *The Quantum Theory of Fields*, Cambridge University Press, Cambridge, UK, 2005.

[6] J. Horejsi, *Fundamentals of Electroweak Theory*, The Karolinum Press, Charles University in Prague, Prague, Chech, 2002.

[7] Particle Data Group Collaboration, K. A. Olive et al., *Review of Particle Physics*, Chin. Phys. C, 38, 090001 (2014) and 2015 update.

[8] The LHCb Collaboration, R. Aaij et al., *Prompt charm production in pp collisions at $\sqrt{s} = 7$ TeV*, Nucl. Phys. B 871 (2013) 1-20, arXiv:1302.2864.

[9] J. Collins, D. Soper and G. Sterman, *Factorization of Hard Processes in QCD*, Adv. Ser. Direct. High Energy Phys. 5 (1989) 1-91, arXiv:hep-ph/0409313.

[10] J. R. Gault, C. -H. Kom, A. Kulesza and W. J. Stirling, *Same-sign W pair production as a probe of double-parton scattering at the LHC*, Eur. Phys. J. C 69 (2010) 53-65, arXiv:1003.3953 [hep-ph].

[11] H. D. Politzer, *Power Corrections at Short Distances*, Nucl. Phys. B 172 (1980) 349-382.

[12] N. Paver and D. Treleani, *Multi-Quark Scattering and Large p^T Jet Production in Hadronic Collisions*, Nuovo Cim. A 70 (1982) 215.

[13] M. Rinaldi, S. Scopetta and V. Vento, *Double parton correlations in constituent quark models*, Phys. Rev. D 87 (2013) 114021, arXiv:1302.6462 [hep-ph].

[14] M. H. Seymour and A. Siodmok, *Constraining MPI models using σ_{eff} and recent Tevatron and LHC underlying event data*, JHEP 1310 (2013) 113, arXiv:1307.5015 [hep-ph].

[15] M. H. Seymour and A. Siodmok, *Extracting $\sigma_{effective}$ from the LHCb double charm measurement*, MAN-HEP-2013-20, MC-NET-13-11, arXiv:1308.6749 [hep-ph].

[16] The CDF Collaboration, F. Abe et al., *Double parton scattering in $p\bar{p}$ collisions at $\sqrt{s} = 1.8$ TeV*, Phys. Rev. D 56 (1997) 3811-3832.

[17] The Axial Field Spectrometer Collaboration, T. Akesson et al., *Double Parton Scatterin in pp Collisions at $\sqrt{s} = 63$ GeV*, Z. Phys. C 34 (1987) 163.

[18] L. Kowarski, *An account of the origin and beginnings of CERN*, CERN-61-10 (see also: *The History of CERN*, http://timeline.web.cern.ch/timelines/The-history-of-CERN).

[19] L. Evans and P. Bryant, *LHC Machine*, JINST 3 (2008) S08001.

[20] L. Evans, *The Large Hadron Collider: A Marvel of Technology*, 1$^{\text{st}}$ edition, Fundamental Sciences, CERN and EPFL Press, Lausanne 2009.

[21] C. Lefevre, *LHC: the guide*, CERN-Brochure-2009-003-Eng, March 2009.

[22] The LHCb Collaboration, A. Alves Jr. et al., *The LHCb Detector at the LHC*, JINST 3 (2008) S08005.

[23] The LHCb Collaboration, R. Aaij et al., *LHCb detector performance*, Int. J. Mod. Phys. A 30 (2015) no. 07, 1530022, arXiv:1412.6352 [hep-ex].

[24] H. Goldstein, C. P. Poole Jr and J. L. Safko Sen., *Classical Mechanics*, 3$^{\text{rd}}$ edition, Addison-Wesley, San Francisco, June 25, 2001.

[25] U. Straumann, *Relativitätstheorie: Ergänzendes Skriptum zur Vorlesung Physik II*, Physik-Institut Universität Zürich, URL: http://www.physik.uzh.ch/~straumann/physik-a/srt.pdf, März 2013.

[26] J. W. Barlow, *Statistics: A Guide to the Use of Statistical Methods in the Physical Sciences*, 6$^{\text{th}}$ edition, John Wiley & Sons, New York, July 1999.

[27] W. Stahel, *Statistische Datenanalyse: Eine Einführung für Naturwissenschaftler*, 4. Auflage, Springer Verlag, November 2002.

[28] The LHCb Collaboration, R. Aaij et al., *Production of associated Υ and open charm hadrons in pp collisions at $\sqrt{s} = 7$ and 8 TeV via double parton scattering*, LHCB-PAPER-2015-046, arXiv:1510.05949 [hep-ex].

[29] I. Belyaev, V. Egorychev, M. Needham and V. Romanovsky, *Observation of the associative production of bottonimum and open charm mesons*, LHCB-ANA-2013-063.

[30] S. Kullback and R. A. Leibler, *On Information and Sufficiency*, The Annals of Mathematical Statistics Vol. 22, No. 1 (1951) 79-86.

[31] S. Kullback, *Information Theory and Statistics*, John Wiley and Sons, New York, USA, 1959.

[32] S. Kullback, *Letters to the editor: the Kullback-Leibler distance*, The American Statistican Vol. 41, No. 4 (1987) 338-341.

[33] W. Hulsbergen, *Decay chain fitting with a Kalman filter*, Nucl. Instrum. Meth. A 552 (2005) 566, arXiv:physics/0503191 [physics.comp-ph].

[34] The LHCb Collaboration, R. Aaij et al., *Observation of associated production of a Z boson with a D meson in the forward region*, JHEP 1404 (2014) 091, arXiv:1401.3235 [hep-ex].

[35] I. Belyaev, A. Bursche and K. Müller, *Observation of Z plus Charmed Hadron Production*, LHCB-ANA-2013-047.

[36] R. Brun and F. Rademakers, *ROOT: An object orientated data analysis framework*, Proceedings AIHENP'96 Workshop, Lausanne, Nucl. Inst. & Meth. in Phys. Res. A 389 (1997) 81-86 (see also http://root.cern.ch/).

[37] M. Pivk and F. Le Diberder, *sPlot: A statistical tool to unfold data distributions*, Nucl. Instrum. Meth. A 555 (2005) 356-369, arXiv:physics/0402083 [physics.data-an].

[38] The LHCb Collaboration, M. Clemencic et al., *The LHCb simulation application, Gauss: Design, evolution and experience*, J. Phys. Conf. Ser. 331 (2011) 032023.

[39] The LHCb Collaboration, I. Belyaev et al., *Handling the generation of primary events in Gauss, the LHCb simulation framework*, J. Phys. Conf. Ser. 331 032047 (see also Nulear Science Symposium Conference Record (NSS/MIC) IEEE (2010) 1155).

[40] The LHCb Collaboration, R. Aaij et al., *Measurement of the track reconstruction efficiency at LHCb*, JINST 10 (2015) no. 02, P02007, arXiv:1408.1251 [hep-ex].

[41] The LHCb Tracking Group, *General LHCb Tracking Wiki Page*, https://twiki.cern.ch/twiki/bin/view/LHCb/LHCbTracking.

[42] The LHCb RICH collaboration, M. Adinolfi et al., *Performance of the LHCb RICH detector at the LHC*, Eur. Phys. J. C 73 (2013) 2431, arXiv:1211.6759 [physics.ins-det].

[43] The LHCb RICH collaboration, A. Powell for the collaboration, *Reconstruction and PID performance of the LHCb RICH detectors*, Nucl. Inst. Meth. A 639 (2011) 260-263.

[44] The LHCb collaboration, A. Powell for the collaboration, *Particle identification at LHCb*, PoS (ICHEP2010) 020, LHCb-PROC-2011-008.

[45] S. Malde, *PID Calib Packages*, https://twiki.cern.ch/twiki/bin/view/LHCb/PIDCalibPackage

[46] The LHCb collaboration, R. Aaij et al., *Prompt K_s^0 production in pp collisions at $\sqrt{s} = 0.9$ TeV*, Phys. Lett. B 693 (2010) 69, arXiv:1008.3105 [hep-ex].

[47] The LHCb collaboration, R. Aaij et al., *Observation of J/ψ pair production in pp collisions at $\sqrt{s} = 7$ TeV*, Phys. Lett. B 707 (2012) 52-59, arXiv:1109.0963.

[48] E. López Azamar et al., *Measurement of trigger efficiencies and biases*, CERN- LHCb-2008-073.

[49] R. Aaij et al., *The LHCb Trigger and its Performance in 2011*, JINST 8 (2013) P04022, arXiv:1211.3055 [hep-ex].

[50] R. Puig, *The LHCb trigger in 2011 and 2012*, LHCb-PUB-2014-046.

[51] M. Vesterinen, *LHCb trigger twiki pages*, https://twiki.cern.ch/twiki/bin/view/LHCb/LHCbTrigger.

[52] C. J. Clopper and E. S. Pearson, *The Use of Confidence or Fiducial Limits Illustrated in the Case of the Binomial*, Biometrika Vol. 26, No. 4 (1934), pp. 404-413.

[53] The LHCb Collaboration, R. Aaij et al., *Absolute luminosity measurements with the LHCb detector at the LHC*, JINST 7 (2012) P01010, arXiv:1110.2866 [hep-ex].

[54] M. Ferro-Luzzi, *Proposal for an absolute luminosity determination in colliding beam experiments using vertex detection of beam-gas interactions*, Nucl. Instrum .Meth. A 553 (2005) 388-399.

[55] The LHCb Collaboration, R. Aaij et al., *Precision luminosity measurements at LHCb*, JINST 9 (2014) no. 12, P12005, arXiv:1410.0149 [hep-ex].